DISSERTATION

FAST AND ACCURATE DOUBLE-HIGHER-ORDER METHOD OF MOMENTS ACCELERATED BY DIAKOPTIC DOMAIN DECOMPOSITION AND MEMORY EFFICIENT PARALLELIZATION FOR HIGH PERFORMANCE COMPUTING SYSTEMS

Submitted by

Ana Manić

Department of Electrical and Computer Engineering

In partial fulfillment of the requirements

For the Degree of Doctor of Philosophy

Colorado State University

Fort Collins, Colorado

Fall 2015

Doctoral Committee:

Advisor: Branislav Notaros

Steven Reising
Iuliana Oprea
Sourajeet Roy
Milan Ilić

ABSTRACT

FAST AND ACCURATE DOUBLE-HIGHER-ORDER METHOD OF MOMENTS ACCELERATED BY DIAKOPTIC DOMAIN DECOMPOSITION AND MEMORY EFFICIENT PARALLELIZATION FOR HIGH PERFORMANCE COMPUTING SYSTEMS

The principal objective of this dissertation is to develop and test a robust method based on the method of moments (MoM) surface integral equation (SIE) formulation for electromagnetic analysis of dielectric and magnetic scatterers and antennas in the frequency domain using double higher order (DHO) mesh discretization. It is well known that by using higher order basis functions for current/field modeling in computational electromagnetics (CEM), significant reductions in the number of unknowns, as well as faster system matrix computation/solution, can be achieved when compared to the traditional low order modeling. Tightly coupled with using higher order basis functions is higher order geometry modeling and together they lay foundation to double higher order (DHO) modeling. Double (geometrical and current) higher order modeling enables using large curved patches, which can greatly reduce the number of unknowns for a given problem and enhance the accuracy and efficiency of the computation. Element orders in the model can also be low both in terms of basis function order or geometrical order, so the low-order modeling approach is actually included in the DHO modeling. So, a whole range of element sizes and shapes, geometrical orders, and current approximation orders can be used at the same time in a single simulation model of a complex structure using the high order (more precisely, low-to-high order) CEM technique.

The two major issues arising in the application of the MoM-SIE numerical methods when solving large and computationally expensive electromagnetic problems are: 1) fast and accurate calculation of the system matrix entrances arising in the MoM-SIE formulation and 2) overall computational and memory storage complexity of the method. The goal of this dissertation is to propose and validate a solution for both of the major method's bottlenecks.

The accurate and fast computation of the system matrix includes advanced methods for numerical computation of singular and near-singular integrals defined on the surface mesh elements. When the method is aimed at analysis of both metallic and dielectric/magnetic structures, the singularity of the integral kernel increases, and requires special treatment of highly singular integrals. Finally, this problem is even more pronounced when higher order basis functions are used for the approximation of electric and magnetic equivalent surface currents defined on curved patches. This dissertation presents a novel method for numerical computation of near-singular (potential) and near-hypersingular (field) integrals defined on Lagrange-type generalized curved parametric quadrilateral surface elements of arbitrary geometrical orders with polynomial basis functions of arbitrary current-approximation orders. The integrals are evaluated using a method based on the singularity extraction, which consists of analytical integration of a principal singular part of the integrand over a (generally not rectangular) parallelogram whose surface is close to the surface of the generalized quadrilateral near the singular point and numerical integration of the rest. The majority of the existing extraction techniques have been developed for planar triangular patches involving low-order basis functions. Few of those have been extended to curved patches but without really taking into account the curvature of the surface. The presented integration technique considers the curvature of the patch by extracting

multiple terms in the evaluation of the principal singular part. Further, the theory behind the extraction technique has been extended to consider integrals with higher order basis functions.

Overall computational complexity and memory requirements of the traditional MoM-SIE method are of the $O(N^3)$ and $O(N^2)$, respectively, where N is the number of unknowns. Even though DHO modelling can reduce number of unknowns by the order of 20, the order of computational complexity remains the same. As the part of this dissertation, a novel fast scalable DHO parallel algorithm on the DHO MoM-SIE in conjunction with a direct solver for dense linear systems with hierarchically semiseparable structures (HSS) is proposed. We are developing asymptotically fast higher order direct algorithms for MoM-SIE solutions which, in a nutshell, are an algebraic generalization to fast multipole methods. In addition to being fast, they offer a promise of being memory- and communication-efficient and amenable to extreme-scale parallel computing. The main advantage of the HSS algorithm is in the linear-complexity ULV-type factorizations (compared to the conventional LU decomposition that has cubic complexity). Our work uses the recently developed new, state-of-the-art, algorithms for solving dense and sparse linear systems of equations based on the HSS method. In addition, rank revealing QR (RRQR) decomposition for the matrix (memory) compression. Its adaptive nature comes from the ability to use the stopping criteria, i.e., relative tolerance value/minimal rank, which allows for the method to store only the low-rank approximation of the original matrix that satisfies predefined accuracy. The standard and most accurate technique for constructing the HSS representation of a dense matrix implies explicit calculation of all matrix elements, and then compression of appropriate blocks using the RRQR decomposition, with an $O(rN^2)$ asymptotic cost. Once the HSS construction is done, the other steps are cheaper, with $O(r^2N)$ time complexity for ULV factorization and $O(rN)$ for solution, respectively, where N was previously

defined and r is the maximum numerical rank. In order to enhance the HSS compression and parallelization i.e. scalability of the method, an algorithm for geometrical preprocessing of the geometrical mesh based on the cobblestone distance sorting technique is utilized. Hence, the MoM unknowns having spatial locality, also exhibit the data locality in the matrix system of equations. To sum up, method is validated and great performance is achieved. Even more, the simulation results show great scalability of the method on more than 1000 processes.

Besides developing a fast, parallel and robust method based on the MoM-SIE, in order to extend applicability of the method to the analysis that involves inhomogeneous anisotropic dielectric and magnetic materials, new symmetric hybridization of the finite element method (FEM) and the MoM was developed. The FEM is one of the general numerical tools for solving closed-region (e.g., waveguide/cavity) problems in electromagnetics. It has been especially effectively used in three-dimensional (3-D) frequency-domain modeling and analysis of electromagnetic structures that contain geometrical and material complexities. In addition, as the part of the work included in this dissertation the DHO FEM method was implemented primarily to support analysis of both inhomogeneous and anisotropic materials.

Further, numerical computation is accelerated by applying Diakoptic Domain Decomposition approach to divide the original problem of interest into smaller subsystems, analyze subsystems independently, and then connect them back together through the surface equivalence theorem.

Finally, all numerical methods described above are validated on a variety of numerical examples and tested across several high performance supercomputing platforms.

ACKNOWLEDGMENTS

To begin I would like to thank my advisor Dr. Branislav Notaroš for his guidance, help and motivation, which has made me a better researcher and this dissertation possible. I would also like to thank my colleagues Sanja Manić, Elene Chobanyan and Nada Šekeljić for a supportive and collaborative environment, which allowed my research to be more productive and enjoyable. Most importantly, I would like to thank my husband Marko Denić for his unconditional love and support.

DEDICATION

To

Radosav Janicijević, Rajka Janicijević, Danica Manić and Aleksandar Manić,

for giving me the most beautiful childhood memories.

TABLE OF CONTENTS

ABSTRACT ii

ACKNOWLEDGMENTS vi

CHAPTERS

1. LARGE ANISOTROPIC INHOMOGENEOUS HIGHER ORDER HIERARCHICAL GENERALIZED HEXAHEDRAL FINITE ELEMENTS FOR 3-D ELECTROMAGNETIC MODELING OF SCATTERING AND WAVEGUIDE STRUCTURES 1
   - 1.1. Introduction 1
   - 1.2. Theory and Implementation 3
   - 1.3. Numerical Results and Discussion 7
   - 1.4. Conclusion 11
2. HIGHER ORDER FEM-MOM-DIAKOPTIC METHOD FOR ANALYSIS OF INHOMOGENEOUS ANISOTROPIC DIELECTRIC AND MAGNETIC SCATTERERS 14
   - 2.1. Introduction 14
   - 2.2. FEM-MoM-Diakoptic Method for Inhomogeneous Anisotropic Scatterers 16
   - 2.2.1. Theory of FEM-MoM-Diakoptics for Scattering Analysis 16
   - 2.2.2. Double-Higher-Order Magnetic-Field FEM Diakoptic Implementation 21
   - 2.3. Numerical Results 26
   - 2.3.1. 2-D Array of Dielectrically Coated PEC Spherical Scatterers 27
   - 2.3.2. Dielectric Scatterer Modeled by Multiple Touching FEM Domains 29
   - 2.3.3. 3-D Array of Cubical Dielectric Scatterers 31
   - 2.3.4. 2-D Array of PEC Spheres with Cloaking Dielectric/Magnetic Metamaterial Covers 33
   - 2.4. Conclusions 36
3. EFFICIENT SCALABLE PARALLEL HIGHER ORDER DIRECT MOM-SIE METHOD WITH HIERARCHICALLY SEMISEARABLE STRUCTURES FOR 3D SCATTERING 37
   - 3.1. Introduction 37
   - 3.2. DHO MoM-SIE Modeling of Metallic Scatterers 41
   - 3.2.1. Surface Integral Equation Formulation 41
   - 3.2.2. Double Higher Order Modeling 42
   - 3.2.3. Geometrical Preprocessing Based on Cobblestone Distance Sorting Technique 43
   - 3.3. HSS Theory 45
   - 3.3.1. HSS Structures 45
   - 3.3.2. HSS Compression 47

3.3.3. ULV HSS Factorization and Solution 49
3.4. Parallelization Strategy 50
3.5. Numerical results and Discussion 53
3.5.1. Example 1: Spherical Scatterer 53
3.5.2. Example 2: NASA Almond 57
3.6. Conclusions 59
4. DUFFY METHOD FOR EVALUATION OF SINGULAR POTENTIAL INTEGRALS OVER CURVED QUADRILATERALS WITH HIGHER ORDER BASIS FUNCTIONS IN SIE ANALYSIS OF ANTENNAS AND SCATTERERS 61
4.1. Introduction 61
4.2. Theory 64
4.2.1. Duffy Method for Singularity Cancellation 65
4.2.2. Four Integration Methods used for Comparison 67
4.3. Numerical Results and Discussion 68
4.3.1. Integral with Constant Basis Functions over a Square Plate 69
4.3.2. Integral with High-Order Basis Functions and Geometry 72
4.3.3. Example of 2-D/2-D Integral 74
4.4. Conclusions 75
5. NUMERICAL COMPUTATION OF NEAR-SINGULAR AND NEAR-HYPERSINGULAR INTEGRALS IN HIGHER ORDER METHOD OF MOMENTS USING CURVED QUADRILATERAL PATCHES 77
5.1. Introduction 77
5.2. Double higher order singularity extraction 79
5.2.1. Near-Singular and Near-Hyper-Singular Integrals 79
5.2.2. Analytical integrals over parallelogram 82
5.3. Numerical Results 85
5.3.1. Near-Singular and Near-Hypersingular Integrals over Curvilinear Spherical patch 86
5.4. Near-Singular and Near-Hypersingular Integrals calculated using optimized expansion of power series 87
5.5. Conclusions 89
4 REFERENCES 91
5 PUBLICATIONS OF THE CANDIDATE 101

1. LARGE ANISOTROPIC INHOMOGENEOUS HIGHER ORDER HIERARCHICAL GENERALIZED HEXAHEDRAL FINITE ELEMENTS FOR 3-D ELECTROMAGNETIC MODELING OF SCATTERING AND WAVEGUIDE STRUCTURES[1]

1.1. Introduction

The finite element method (FEM) is one of the most powerful and versatile general numerical tools for solving both open-region (e.g., antenna/scattering) and closed-region (e.g., waveguide/cavity) problems in electromagnetics [1–4]. It has been especially effectively used in three-dimensional (3-D) frequency-domain modeling and analysis of electromagnetic structures that contain geometrical and material complexities. In terms of the particulars of the numerical discretization, on the other hand, traditional FEM tools are low-order (also referred to as small-domain or subdomain) techniques – the electromagnetic structure is modeled by volume geometrical elements that are electrically very small and with planar sides, and the fields within the elements are approximated by low-order basis functions, which results in very large requirements in computational resources. An alternative which can greatly reduce the number of unknowns for a given problem and enhance the accuracy and efficiency of the FEM analysis is the higher order (also known as the large-domain or entire-domain) computational approach, which utilizes higher order basis functions defined in large curved geometrical elements [5]. However, although higher order FEM modeling has, since relatively recently, been constantly

[1] Reprinted, with permission, from "A. B. Manic, S. B. Manic, M. M. Ilic, and B. M. Notaros, "Large Anisotropic Inhomogeneous Higher Order Hierarchical Generalized Hexahedral Finite Elements for 3-D Electromagnetic Modeling of Scattering and Waveguide Structures," Microwave and Optical Technology Letters, vol. 54, No. 7, July 2012, pp. 1644-1649. " with copyright © 2012 of Wiley Periodicals, Inc.

gaining popularity among FEM developers and practitioners and is definitely becoming a mainstream activity in FEM research and practice, there seems to be a lack of investigations and reported results on the actual higher order and large-domain modeling of material complexities and a full exploitation of modeling flexibility and efficiency of large curved finite elements with *p*-refined high-order field approximations when applied in the presence of arbitrary material anisotropy and inhomogeneity.

This paper presents a novel higher order large-domain FEM technique for efficient and accurate 3-D analysis in the frequency domain of open- and closed-region electromagnetic structures involving general anisotropic inhomogeneous materials, as an extension and generalization of works in [6–9]. The technique implements Lagrange-type generalized curved parametric hexahedral finite elements of arbitrary geometrical-mapping orders, filled with anisotropic inhomogeneous materials with continuous spatial variations of complex relative permittivity and permeability tensors described by Lagrange interpolation polynomials of arbitrary material-representation orders, and curl-conforming hierarchical polynomial vector basis functions of arbitrary field-expansion orders for the approximation of the electric field vector within the elements. The technique is applied to the analysis of open-region scattering structures, with a truncation of the FEM domain by a hybridization with a higher order method of moments (MoM) within the surface integral equation (SIE) approach [10, 8], and to the analysis of closed-region microwave waveguide structures, with a simple single-mode boundary condition introduced across the waveguide ports and a large buffer finite element at each port to ensure relaxation of higher modes [7]. To the best of our knowledge, this is the first demonstration of large (extending a couple of wavelengths in each dimension) anisotropic inhomogeneous curved finite elements with *p*-refined field distributions of high (e.g., seventh)

approximation orders in high-frequency electromagnetics. Our current and future related work includes applications of these new elements in analysis and design of anisotropic inhomogeneous dielectric and magnetic material structures aimed for (i) electromagnetic cloaking [13], (ii) perfectly matched layers (PMLs) [2], and (iii) waveguide components.

1.2. Theory and Implementation

Consider an electromagnetic structure that contains some anisotropic continuously inhomogeneous material regions. In our analysis method, the computational domain is first tessellated using higher order geometrical elements, and the electric field intensity vector within the *e*-th element is approximated by the following sum:

$$\mathbf{E}^e = \sum_{l=1}^{N^e} \gamma_l^e \, \mathbf{f}_l^e \,, \tag{1.1}$$

where $\mathbf{f}_l^e$ are higher order vector basis functions with a total of N^e unknown field-distribution coefficients γ_l in the element. Elements are adopted in the form of Lagrange-type generalized curved parametric hexahedra of arbitrary geometrical orders K_u^e, K_v^e, and K_w^e ($K_u^e, K_v^e, K_w^e \geq 1$), analytically described as [6]

$$\mathbf{r}^e(u,v,w) = \sum_{i=0}^{K_u^e} \sum_{j=0}^{K_v^e} \sum_{k=0}^{K_w^e} \mathbf{r}_{ijk}^e L_i^{K_u^e}(u) L_j^{K_v^e}(v) L_k^{K_w^e}(w) \,, \qquad -1 \leq u,v,w \leq 1, \tag{1.2}$$

where $\mathbf{r}_{ijk}^e = \mathbf{r}(u_i, v_j, w_k)$ are position vectors of interpolation nodes and $L_i^{K_u^e}$ represent Lagrange interpolation polynomials,

$$L_i^{K_u^e}(u) = \prod_{\substack{h=0 \\ h \neq i}}^{K_u^e} \frac{u - u_h}{u_i - u_h} \,, \tag{1.3}$$

and similarly for $L_j^{K_v^e}(v)$ and $L_k^{K_w^e}(w)$. Equations (1.2) and (1.3) define a mapping from a cubical parent domain to the generalized hexahedron, as illustrated in Fig. 1.1.

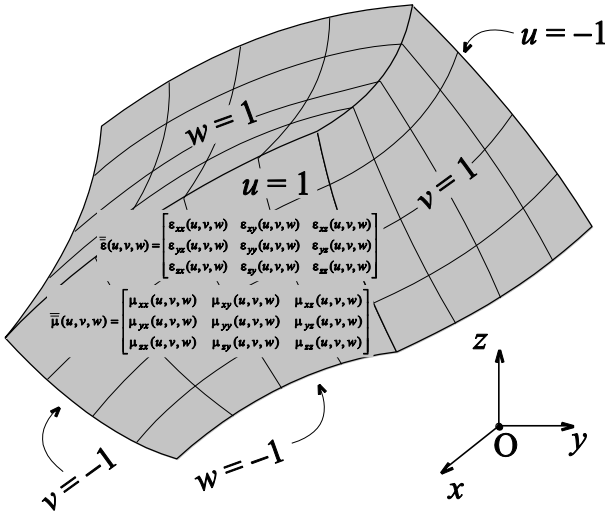

Figure 1.1. Generalized curved parametric hexahedron defined by (1.2), with continuous spatial variations of complex relative permittivity and permeability tensors of the material given by (1.4); cubical parent domain is also shown.

The same polynomials in (1.3) are used to describe the continuous spatial variations of both the complex relative permittivity and permeability tensors, $\bar{\bar{\varepsilon}}_{\mathrm{r}}$ and $\bar{\bar{\mu}}_{\mathrm{r}}$, of an anisotropic inhomogeneous material filling the generalized hexahedral element in Fig. 1.1 (*e*-th element in the model) as follows:

$$\bar{\bar{\varepsilon}}_{\mathrm{r}}^{e}(u,v,w)=\begin{bmatrix}\varepsilon_{\mathrm{r},xx}^{e}(u,v,w) & \varepsilon_{\mathrm{r},xy}^{e}(u,v,w) & \varepsilon_{\mathrm{r},xz}^{e}(u,v,w)\\ \varepsilon_{\mathrm{r},yx}^{e}(u,v,w) & \varepsilon_{\mathrm{r},yy}^{e}(u,v,w) & \varepsilon_{\mathrm{r},yz}^{e}(u,v,w)\\ \varepsilon_{\mathrm{r},zx}^{e}(u,v,w) & \varepsilon_{\mathrm{r},zy}^{e}(u,v,w) & \varepsilon_{\mathrm{r},zz}^{e}(u,v,w)\end{bmatrix}=\sum_{m=0}^{M_u^e}\sum_{n=0}^{M_v^e}\sum_{p=0}^{M_w^e}\bar{\bar{\varepsilon}}_{\mathrm{r},mnp}^{e}L_m^{M_u^e}(u)L_n^{M_v^e}(v)L_p^{M_w^e}(w),\ -1\le u,v,w\le 1 \quad (1.4)$$

where $\bar{\bar{\varepsilon}}_{\mathrm{r},mnp}^{e}=\bar{\bar{\varepsilon}}_{\mathrm{r}}^{e}(u_m,v_n,w_p)$ are the relative permittivity values at the points defined by position vectors of spatial interpolation nodes, $\mathbf{r}_{mnp}^{e}$, and similarly for $\bar{\bar{\mu}}_{\mathrm{r}}^{e}(u,v,w)$, with M_u^e, M_v^e, and M_w^e ($M_u^e, M_v^e, M_w^e \ge 1$) standing for arbitrary material-representation polynomial orders within the element.

Basis functions are curl-conforming hierarchical polynomials of arbitrary field-approximation orders N_u^e, N_v^e, and N_w^e ($N_u^e, N_v^e, N_w^e \geq 1$) in the e-th element, in Fig. 1.1, which, for the reciprocal u-component of the field vector, are given by [6]

$$\mathbf{f}_{uqst}^e = u^q P_s(v) P_t(w) \frac{\mathbf{a}_v^e \times \mathbf{a}_w^e}{\mathfrak{I}^e}, \quad P_s(v) = \begin{cases} 1-v, & n=0 \\ v+1, & n=1 \\ v^s - 1, & s \geq 2, \text{even} \\ v^s - v, & s \geq 3, \text{odd} \end{cases}, \quad \mathfrak{I}^e = (\mathbf{a}_u^e \times \mathbf{a}_v^e) \cdot \mathbf{a}_w^e, \quad \mathbf{a}_u^e = \frac{\partial \mathbf{r}^e}{\partial u},$$

$$\mathbf{a}_v^e = \frac{\partial \mathbf{r}^e}{\partial v}, \ \mathbf{a}_w^e = \frac{\partial \mathbf{r}^e}{\partial w}, \ -1 \leq u,v,w \leq 1, \ q = 0,1,\ldots,N_u^e - 1, \ s = 0,1,\ldots,N_v^e, \ t = 0,1,\ldots,N_w^e, \tag{1.5}$$

where $\mathfrak{I}^e$ is the Jacobian of the covariant transformation, and $\mathbf{a}_u^e$, $\mathbf{a}_v^e$, and $\mathbf{a}_w^e$ are the unitary vectors along the parametric coordinates of the element. Higher order hierarchical basis functions with improved orthogonality and conditioning properties constructed from Legendre and other standard orthogonal polynomials [11, 12] may also be implemented.

Geometrical-mapping orders (K_u^e, K_v^e, K_w^e) in (1.2), material-representation orders (M_u^e, M_v^e, M_w^e) in (1.4), and field-expansion orders (N_u^e, N_v^e, N_w^e) in (1.5) are entirely independent from each other, and the three sets of parameters of a higher order model can be combined independently for the best overall performance of the method. Furthermore, because the basis functions in (1.5) are hierarchical (each lower-order set of functions is a subset of all higher-order sets), all of the parameters can be adopted anisotropically in different directions within an element, and nonuniformly from element to element in a model.

To solve for the field coefficients γ_l, we substitute the field expansion (1.1) in the curl-curl electric-field vector wave equation [6], which for the *e*-th element reads

$$\nabla \times \left[\bar{\bar{\mu}}_{\mathrm{r}}^{e\,-1}(u,v,w) \nabla \times \mathbf{E}^e(u,v,w) \right] - k_0^2 \bar{\bar{\varepsilon}}_{\mathrm{r}}^e(u,v,w) \mathbf{E}^e(u,v,w) = 0, \tag{1.6}$$

with $k_0 = \omega\sqrt{\varepsilon_0\mu_0}$ being for the free-space wave number. A standard Galerkin weak-form discretization of (1.6) yields

$$\int_{V^e} \left[\nabla \times \mathbf{f}_t^e(u,v,w)\right] \cdot \left[\overline{\overline{\mu}}_r^{e-1}(u,v,w)\nabla \times \mathbf{E}^e(u,v,w)\right] \mathrm{d}V - k_0^2 \int_{V^e} \mathbf{f}_t^e(u,v,w) \cdot \left[\overline{\overline{\varepsilon}}_r^e(u,v,w)\mathbf{E}^e(u,v,w)\right] \mathrm{d}V = \mathrm{j}k_0\eta_0 \oint_{S^e} \mathbf{f}_t^e(u,v,w) \cdot \left[\mathbf{n} \times \mathbf{H}^e(u,v,w)\right] \mathrm{d}S \quad ,(1.7)$$

where V^e is the volume of the *e*-th element, bounded by the surface S^e, n is the outward unit normal on S^e, $\mathbf{f}_t$ are testing functions [the same as basis functions in (1.1) and (1.5)], and η_0 is the free-space intrinsic impedance. Due to the continuity of the tangential component of the magnetic field intensity vector, $\mathbf{n} \times \mathbf{H}^e$, in (1.7) across the interface between any two finite elements in the FEM model, the right-hand side term in (1.7) contains the surface integral over the overall boundary surface, *S*, of the entire FEM domain, and not over the internal boundary surfaces between the individual hexahedra in the model.

For open-region scattering structures, the FEM domain is truncated at the surface *S* by means of unknown equivalent surface electric and magnetic currents, of densities $\mathbf{J}_S$ and $\mathbf{M}_S$, respectively, defined on MoM curved quadrilateral patches representing external (on *S*) faces of the FEM hexahedra, and expanded using a divergence-conforming 2-D version of basis functions in (1.5) [10]. The electric field in the FEM domain, $\mathbf{E}_{\mathrm{FEM}}$, given by (1.1) in individual finite elements, is coupled to the scattered electric and magnetic fields due to $\mathbf{J}_S$ and $\mathbf{M}_S$, $\mathbf{E}_{\mathrm{MoM}}$ and $\mathbf{H}_{\mathrm{MoM}}$, and the incident fields, $\mathbf{E}_{\mathrm{inc}}$ and $\mathbf{H}_{\mathrm{inc}}$, through boundary conditions for the tangential field components on *S* as follows:

$$\mathbf{n} \times \mathbf{E}_{\mathrm{FEM}} = \mathbf{n} \times \mathbf{E}_{\mathrm{MoM}}(\mathbf{J}_S, \mathbf{M}_S) + \mathbf{n} \times \mathbf{E}_{\mathrm{inc}}, \quad \mathbf{n} \times \mathbf{H}_{\mathrm{FEM}} = \mathbf{J}_S = \mathbf{n} \times \mathbf{H}_{\mathrm{MoM}}(\mathbf{J}_S, \mathbf{M}_S) + \mathbf{n} \times \mathbf{H}_{\mathrm{inc}}, \quad (1.8)$$

thus providing the computational interface between the FEM and MoM regions, with $\mathbf{E}_{\mathrm{FEM}}$, $\mathbf{J}_{\mathrm{S}}$ and $\mathbf{M}_{\mathrm{S}}$ as unknowns, and giving rise to a hybrid higher order FEM-MoM solution [8].

For closed-region microwave waveguide structures, the right-hand side term in (1.7) reduces to the surface integral across the artificially introduced planar surfaces (waveguide ports). If, moreover, the waveguide operates in the single-mode regime (which is a standard assumption for practical microwave applications) and the ports are moved away from all discontinuities (by placing a single large finite element with a high field-approximation order in the longitudinal direction as a buffer zone), the boundary condition at the ports is expressed as [1, 7]

$$\mathbf{n}\times(\nabla\times\mathbf{E}_{\mathrm{FEM}})+\mathrm{j}k_{z10}\mathbf{n}\times(\mathbf{n}\times\mathbf{E}_{\mathrm{FEM}})=\begin{cases}-2\mathrm{j}k_{z10}\mathbf{E}_{\mathrm{inc}},\ \mathbf{E}_{\mathrm{inc}}=\mathbf{E}_0\exp(-\mathrm{j}k_{z10}z) & \text{(excitation port)}\\ 0 & \text{(receiving ports)}\end{cases}, \quad (1.9)$$

where, for a rectangular waveguide, $k_{z10}=\sqrt{k_0^2-(\pi/a)^2}$ is the wave number of the dominant mode (a is the larger dimension of the waveguide cross section).

1.3. Numerical Results and Discussion

As the first example of the application of the novel higher order large-domain general FEM technique, aimed at demonstrating the accuracy and efficiency of the technique when curved large anisotropic finite elements with p-refined field distributions are used, consider an anisotropic dielectric (nonmagnetic and lossless) spherical scatterer, of radius $a=1\,\mathrm{m}$ and relative permittivity given by the tensor

$$\bar{\bar{\varepsilon}}_{\mathrm{r}}=\begin{bmatrix}4&0&0\\0&4&0\\0&0&1\end{bmatrix}, \quad (1.10)$$

illuminated by an incident time-harmonic plane wave of frequency $f = 150\,\text{MHz}$. Shown in the inset of Fig. 1.2 is the higher order FEM-MoM model of the scatterer, which consists of a single curved hexahedral FEM element and six MoM curved quadrilaterals, all of geometrical-mapping

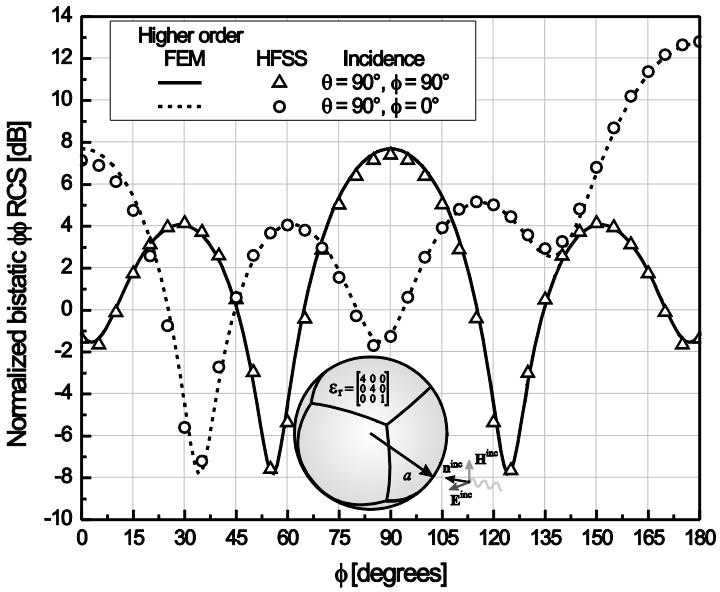

Figure 1.2. Bistatic RCS in the x-y plane of an anisotropic dielectric spherical scatterer with the relative permittivity tensor given by (1.10), normalized to λ_0^2, λ_0 being the free-space wavelength, for the plane wave incidence from the direction defined by $\theta = 90^o$ and $\varphi = 90^o$ or $\varphi = 0^o$; higher order FEM-MoM model of the scatterer, with a single finite element, is shown in the figure inset.

orders $K = 2$. The orders of the polynomial expansion are $N_{\text{FEM}} = 7$ and $N_{\text{MOM}} = 6$ for the fields in the FEM domain and for the surface currents in the MoM domain, respectively. In Fig. 1.2, the bistatic radar cross section (RCS) of the scatterer computed using the higher order FEM-MoM is compared with the results obtained by HFSS, and an excellent agreement of the two sets of results is observed. The described FEM-MoM model results in 1344 FEM and 864 MoM unknowns, while he HFSS simulation, which converges to 0.1 delta energy after 6 adaptive

passes, employs 412,592 first-order tetrahedral finite elements (the number of unknowns is of the same order of magnitude).

As an example of an accurate and efficient higher order large-domain FEM-MoM scattering analysis of continuously inhomogeneous anisotropic structures, we next consider a dielectric cubical scatterer, of side length $a = 1\,\mathrm{m}$, with relative permittivity described by the tensor

$$\bar{\bar{\varepsilon}}_{\mathrm{r}}(u) = \begin{bmatrix} 9-8u^2 & 0 & 0 \\ 0 & 1 & 0 \\ 0 & 0 & 1 \end{bmatrix}, \qquad -1 \le u \le 1, \tag{1.11}$$

as shown in Fig. 1.3(a). The scatterer is excited by an incident ϕ-polarized plane wave from different directions in the x-y plane ($\theta = 90^{\mathrm{o}}$) at a frequency of $f = 300\,\mathrm{MHz}$. The FEM-MoM model, in Fig. 1.3(a), consists of a single FEM element of the geometrical order K = 1, with the permittivity ε_{rxx} represented as a Lagrange polynomial function of material-representation order M = 2, and six MoM quadrilaterals. The orders of the FEM and MoM field/current polynomial expansions are the same as in the first example. The reference HFSS solutions for validation and comparison are obtained using piecewise homogeneous anisotropic layered approximations of the dielectric profile, with the original structure subdivided into several equally thick anisotropic layers with individual permittivities calculated as the average of the corresponding permittivity functions for the layer, as depicted in Fig. 1.3(b) for the model with seven layers. From the results for the monostatic RCS of the scatterer shown in Fig. 1.4, we see that models with three and five layers provide an inadequate approximation of the continuous permittivity profile of the cube, yielding rather inaccurate RCS values, and that seven (and more) layers are necessary to obtain a satisfactory approximation of the profile resulting in a quite accurate RCS

characterization and a very good agreement of the higher order continuously inhomogeneous anisotropic FEM model and the approximate layered HFSS model.

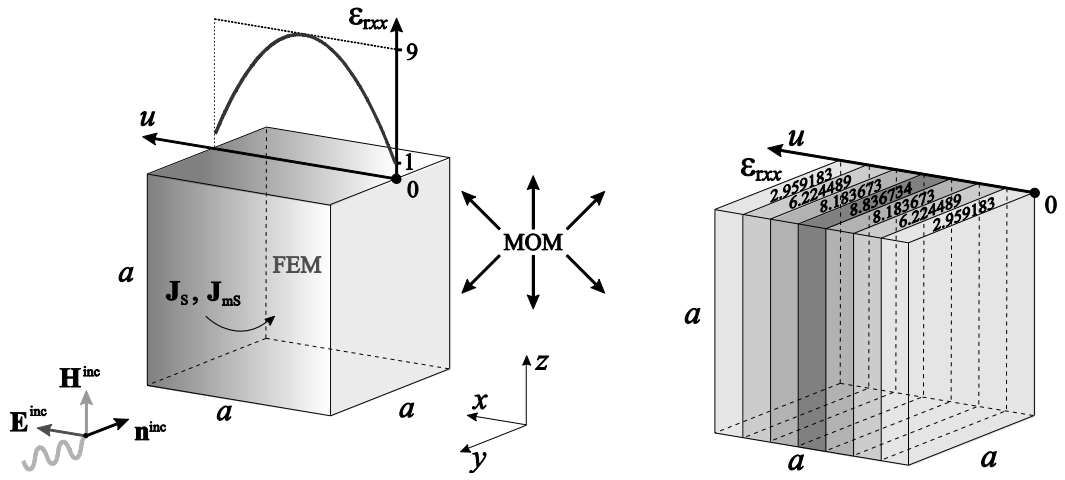

(a) (b)

Figure 1.3. Analysis of a continuously inhomogeneous anisotropic dielectric cubical scatterer with the relative permittivity tensor given by (1.11): (a) exact higher order FEM-MoM model with a single finite element and (b) approximate piecewise homogeneous anisotropic model, with averaged permittivities of layers, for HFSS simulation.

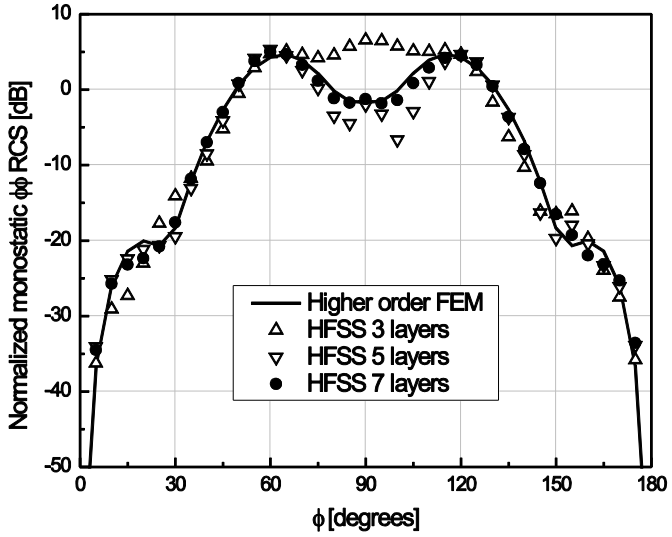

Figure 1.4. Normalized monostatic RCS (RCS/λ_0^2) in the *x*-*y* plane of the scatterer in Fig. 1.3.

Finally, to demonstrate an accurate and efficient higher order large-domain FEM analysis of waveguide structures with anisotropic continuously inhomogeneous materials, that also include curvature, the last example is an H-plane waveguide T-junction with a "partial-height" cylindrical dielectric post, shown in Fig. 1.5(a), with the relative permittivity tensor defined as

$$\bar{\bar{\varepsilon}}_{\mathrm{r}}(v)=\begin{bmatrix}1 & 0 & 0\\ 0 & 1+7\dfrac{(v+1)^2}{4} & 0\\ 0 & 0 & 1\end{bmatrix},\qquad -1\le v\le 1, \tag{1.12}$$

and the $\varepsilon_{\mathrm{r}yy}$ component being represented as the second-order (M = 2) Lagrange polynomial. For the reference HFSS simulation, the post is modeled using six layers as depicted in Fig. 1.5(b). A higher order FEM model of the junction and discontinuity consists of three trilinear (K = 1) and six triquadratic (K = 2) hexahedral finite elements, as portrayed in Fig. 1.5(a), with polynomial field-expansion orders (N_u^e, N_v^e, and N_w^e) in the FEM simulation ranging from 2 to 7 in different elements and different directions. In Fig. 1.6, we observe an excellent agreement of higher order continuous isotropic FEM and layered anisotropic HFSS results for the S-parameters of the structure.

1.4. Conclusion

This paper has presented a novel higher order large-domain FEM technique for 3-D analysis of open- and closed-region electromagnetic structures involving general anisotropic inhomogeneous materials. The technique features Lagrange generalized curved parametric hexahedral finite elements with anisotropic continuously inhomogeneous materials in conjunction with curl-conforming hierarchical polynomial vector basis functions for field

expansions. The examples have demonstrated efficient and accurate simulations of anisotropic continuously inhomogeneous scattering and waveguide structures. In the analysis of scatterers,

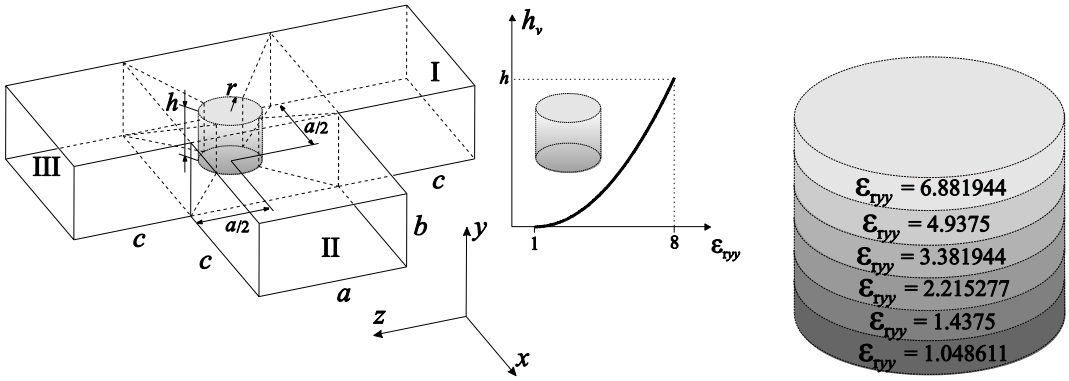

(a) (b)

Figure 1.5. *H*-plane WR-75 waveguide T-junction with a "partial-height" continuously inhomogeneous anisotropic cylindrical dielectric post whose relative permittivity tensor is given by (1.12): (a) structure geometry ($r = 5\,\text{mm}$, $h = 6\,\text{mm}$, $a = 19.05\,\text{mm}$, $b = 9.525\,\text{mm}$, and $c = 30\,\text{mm}$) and higher order large-domain FEM mesh and (b) approximate 6-layer model of the post used in HFSS simulations.

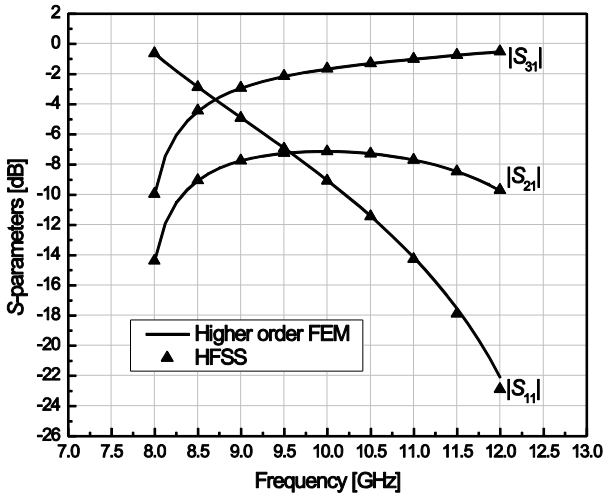

Figure. 1.6. Magnitudes of *S*-parameters of the waveguide structure in Fig. 1.5.

the FEM domain is truncated by a hybridization with a higher order MoM-SIE technique. For multiport waveguide discontinuities, a simple single-mode boundary condition is introduced across the waveguide ports. This appears to be the first demonstration of large (up to a couple of wavelengths across) anisotropic inhomogeneous curved finite elements with p-refined high-order (e.g., seventh-order) field distributions for electromagnetic modeling. Our current and future work includes applications of the new elements in electromagnetic cloaking, PMLs, and waveguide component designs.

2. HIGHER ORDER FEM-MOM-DIAKOPTIC METHOD FOR ANALYSIS OF INHOMOGENEOUS ANISOTROPIC DIELECTRIC AND MAGNETIC SCATTERERS[2]

2.1. Introduction

The finite element method (FEM) is, by its inherent features, especially suitable for modeling and analysis of structures that contain inhomogeneous, complex electromagnetic materials and geometrical irregularities. The FEM is well established as a method of choice for such applications, with the analysis of open-region scattering structures being performed truncating the FEM domain by a hybridization with the method of moments (MoM) or by some sort of a boundary condition. On the other hand, one possible general strategy aimed at extending the practical applicability of the FEM over its inherent numerical limit and considerably enhancing its efficiency in real-world simulations is the diakoptic approach [14]–[20], according to which, the solution of a large and complex electromagnetic system is found as a linear combination of solutions of diakoptic subsystems, using explicit linear relations between coefficients in expansions of equivalent electric and magnetic surface currents on boundary surfaces of subsystems.

The diakoptic analysis of electromagnetic systems is formally similar to the diakoptic approach in circuit theory [21]. However, our diakoptic analysis is based on the surface equivalence principle and operates with coefficients in expansions of surface electric and magnetic currents and volume electromagnetic fields. The diakoptic analysis also belongs to the

[2] This is an Accepted Manuscript of an article published by Taylor & Francis in Electromagnetics on 14 Apr. 2014, available online: http://wwww.tandfonline.com/10.1080/02726343.2014.877755.

class of domain decomposition methods [22]–[25]. However, diakoptics takes explicitly into account linear relations between coefficients of the equivalent surface current expansions, with each electromagnetic subsystem being represented by linear relations written in the form of matrices. In addition, the diakoptic approach uses a direct solution of the diakoptic linear system of equations.

This paper presents a new FEM-MoM-diakoptic method for analysis of inhomogeneous anisotropic dielectric and magnetic scatterers in the frequency domain, as a continuation of the previous work in [14]–[20]. The method splits the original electromagnetic system into a number of closed-region subsystems containing material complexities, which are analyzed by a FEM technique (FEM diakoptic subsystems), and an open-region subsystem enclosing the FEM subsystems, analyzed by a MoM technique (MoM diakoptic subsystem). Each of the subsystems is analyzed completely independently applying FEM or MoM solvers to obtain linear relations between coefficients in the expansions of equivalent electric and magnetic surface currents on the boundary surface of each subsystem (diakoptic surfaces). In the final system of equations, the only unknowns are the expansion coefficients on diakoptic surfaces.

The method implements Lagrange-type generalized curved parametric hexahedral finite elements of arbitrary geometrical-mapping orders, filled with inhomogeneous anisotropic materials with continuous spatial variations of complex relative permittivity and permeability tensors described by Lagrange interpolation polynomials of arbitrary material-representation orders. Curl-conforming hierarchical polynomial vector basis functions of arbitrary field-expansion orders are used for the approximation of the electric field vector within the finite elements, while divergence-conforming higher order vector bases on generalized curved parametric quadrilaterals are implemented for diakoptic surfaces. Furthermore, the connection

between the diakoptic electric sources and the magnetic field in the FEM subsystems is enforced using dual sets of higher order basis functions satisfying explicitly the natural relation between curl-conforming and divergence-conforming quantities, when closing the FEM domain by a boundary surface with fictitious equivalent surface currents. Finally, this diakoptic method inherently allows touching of the subsystems, i.e., the subsystems can share a common diakoptic boundary – without requirements for introduction of additional basis functions. Note that, theoretically, the diakoptic surfaces can be anywhere: away from the scatterers, at the boundary of a scatterer, or even crossing the volume of a scatterer.

The rest of this paper is organized as follows. Section 2.2 presents the theory of the FEM-MoM-diakoptic method for analysis of inhomogeneous anisotropic dielectric and magnetic scatterers, starting with the surface equivalence principle, and deriving linear relations between diakoptic coefficients and representing electromagnetic subsystems by diakoptic matrices. It also presents the implementation of the method based on a magnetic-field FEM diakoptic formulation and double-higher-order numerical discretization. In Section 2.3, the proposed diakoptic method is validated in several characteristic scattering examples.

2.2. FEM-MoM-Diakoptic Method for Inhomogeneous Anisotropic Scatterers

2.2.1. Theory of FEM-MoM-Diakoptics for Scattering Analysis

The diakoptic method is based on the surface equivalence principle [26], [27]. For instance, consider an arbitrary closed surface *S*, as shown in Fig. 2.1a, which divides the original electromagnetic system into two regions, with sources of electromagnetic fields (e.g., lumped generators or incident fields in the system) assumed to exist in both regions. Employing the surface equivalence principle, equivalent sources are placed at each side of the boundary *S* (in

each of the regions) and are chosen so that the electric and magnetic fields, generated by the sources, inside each individual region remain the same as in the original system, while the fields in the other region are annulled, as illustrated in Figs. 2.1b and 2.1c. For the inner region (reg 1), the densities of equivalent electric and magnetic surface currents are given by $\mathbf{J}_{\mathrm{e}}^{\mathrm{reg}\,1} = \mathbf{n} \times \mathbf{H}_{1S}$ and $\mathbf{M}_{\mathrm{e}}^{\mathrm{reg}\,1} = -\mathbf{n} \times \mathbf{E}_{1S}$, where n denotes the inward looking unit normal on *S*, and $\mathbf{E}_{1S}$ and $\mathbf{H}_{1S}$ stand for the electric and magnetic field vectors, respectively, on the inner side of *S* in the original system in Fig. 2.1a. The equivalent sources for the outer region (reg 2) are obtained in an analogous fashion. Applying the tangential continuity conditions for the fields in the original system, we obtain the following relations between equivalent sources for the two regions:

$$\mathbf{J}_{\mathrm{e}}^{\mathrm{reg}\,1} = -\mathbf{J}_{\mathrm{e}}^{\mathrm{reg}\,2} \quad \text{and} \quad \mathbf{M}_{\mathrm{e}}^{\mathrm{reg}\,1} = -\mathbf{M}_{\mathrm{e}}^{\mathrm{reg}\,2}, \tag{2.1}$$

which will later be used explicitly to connect unknown variables in the diakoptic method.

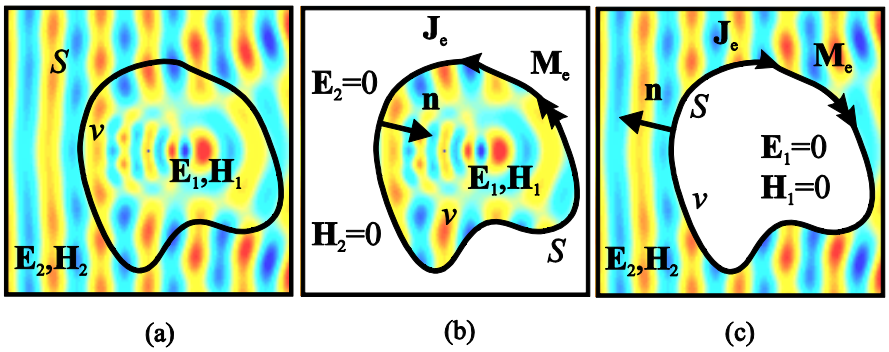

Figure 2.1. Illustration of the surface equivalence principle, as the theoretical foundation of the FEM-MoM-diakoptic method: (a) original electromagnetic system, (b) equivalent problem for the interior region, and (c) equivalent problem for the exterior region.

Next, we use an example depicted in Fig. 2.2 to describe the implementation of the diakoptic analysis combining FEM and MoM solvers. The diakoptic approach starts with subdividing the original electromagnetic system into a number of arbitrary non-overlapping subsystems, as shown in Fig. 2.2a, where the so-called diakoptic boundary is the surface enclosing different

subsystems and, in general, containing a number of disconnected closed surfaces. In the present method, a FEM technique is used for the analysis of each of the closed-region subsystems (N_{FEM} FEM subsystems), as indicated in Fig. 2.2b, while the open-region subsystem, that in Fig. 2.2c, is analyzed invoking a MoM technique (MoM subsystem). Secondly, the diakoptic boundary is used as an interface between the FEM and MoM domains (subsystems) employing the surface equivalence principle (Fig. 2.1) and allowing each of the subsystems to be independently analyzed and then connected back together through relations in (2.1). Consequently, when implementing the diakoptic approach using FEM and MoM solvers, the unknowns, in general, are: (i) distributions of electric and magnetic fields of intensities $\mathbf{E}$ and $\mathbf{H}$ in the FEM regions and (ii) distributions of equivalent surface electric and magnetic currents of densities $\mathbf{J}_{\text{e}}$ and $\mathbf{M}_{\text{e}}$ at the diakoptic boundary.

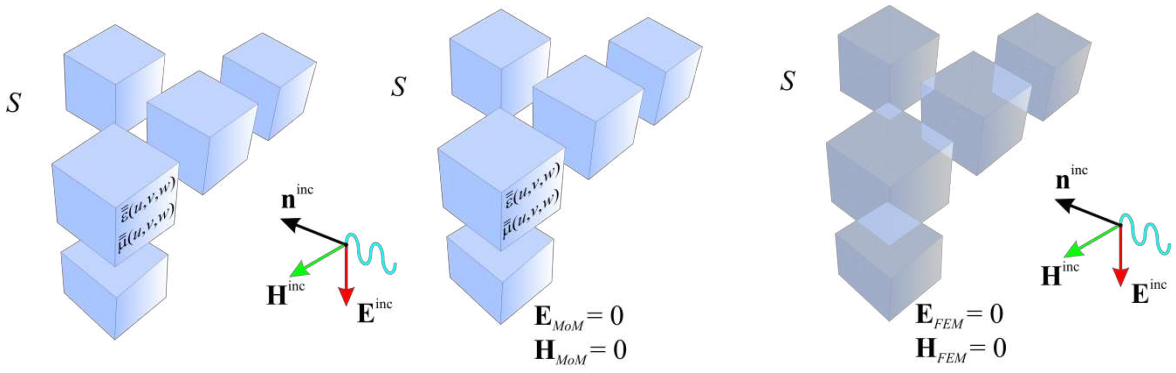

Figure 2.2. Application of the FEM-MoM-diakoptic technique for scattering analysis: (a) original electromagnetic system split into $N_{\text{FEM}}+1$ parts (subsystems), (b) N_{FEM} closed-region subsystems containing material complexities, analyzed by a FEM technique (FEM diakoptic subsystems), and (c) an open-region subsystem, analyzed by a MoM technique (MoM diakoptic subsystem).

Let the total number of unknown coefficients for the approximation of $\mathbf{E}$ and $\mathbf{H}$, placed in column-matrices $[\mathbf{e}]$ and $[\mathbf{h}]$, respectively, for all FEM subsystems be $N_{\text{tot}}^{\text{FEM}} = N_{\text{tot}}^{e} + N_{\text{tot}}^{h}$,

where $N_{\text{tot}}^{e} = \sum_{i=1}^{N_{\text{FEM}}} N_i^{e}$ and $N_{\text{tot}}^{h} = \sum_{i=1}^{N_{\text{FEM}}} N_i^{h}$ are the total numbers of coefficients in [**e**] and [**h**], and N_i^{e} and N_i^{h} are the respective numbers of coefficients for the *i*-th FEM subsystem. In addition, there are $2D$ unknowns for the approximation of $\mathbf{J}_{\text{e}}$ and $\mathbf{M}_{\text{e}}$ at the diakoptic boundary (the union of N_{FEM} disconnected boundary surfaces in Fig. 2.2b), namely, D coefficients for $\mathbf{J}_{\text{e}}$, in the column-matrix $[\mathbf{j}_{\text{e}}]$, and the same number of coefficients for $\mathbf{M}_{\text{e}}$, in $[\mathbf{m}_{\text{e}}]$, where $D = \sum_{i=1}^{N_{\text{FEM}}} D_i$, with D_i being the number of diakoptic coefficients associated with the *i*-th FEM subsystem ($i = 1,2,\ldots,N_{\text{FEM}}$). It is essential that the column-matrices $[\mathbf{j}_{\text{e}}]$ and $[\mathbf{m}_{\text{e}}]$ are of the same dimensions.

Based on the linearity of the electromagnetic system in Fig. 2.2a, the objective of the diakoptic analysis of each of the subsystems in Figs. 2.2b and 2.2c is to define linear relations between electric and magnetic diakoptic sources belonging to the diakoptic boundary of the subsystem, in the following form:

$$[\mathbf{j}_{ek}] = [\mathbf{Y}_k][\mathbf{m}_{ek}] + [\mathbf{j}_{ek}]_0, \quad k = 1,2, \tag{2.2}$$

where $k = 1$ denotes the inner side (FEM side) of the union of all disconnected diakoptic subdomains and $k = 2$ denotes the outer side (MoM side) of the same union, and where $[\mathbf{Y}_k]$ is the $D \times D$ diakoptic matrix of the subsystem and $[\mathbf{j}_{ek}]_0$ is the $D \times 1$ column-matrix containing coefficients of $\mathbf{J}_{\text{e}}$ that represent the excitation in the subsystem. In order to numerically calculate the matrix $[\mathbf{Y}_k]$, we assume that all the excitations in the subsystem are turned off and the subsystem is excited with one, the j-th, unit-valued coefficient in $[\mathbf{m}_{ek}]$, while all other coefficients in $[\mathbf{m}_{ek}]$ are equal to zero. By using the FEM solver, we calculate coefficients of $\mathbf{E}$,

$\mathbf{H}$, and $\mathbf{J}_{\mathrm{e}}$ in the FEM subsystems, with the obtained coefficients of $\mathbf{J}_{\mathrm{e}}$ representing, numerically, the j-th column of the matrix $[\mathbf{Y}_k]$. While MoM matrices are dense, FEM matrices are sparse, and are stored and computed as such.

In the same analysis, we obtain the linear relations between coefficients in $[\mathbf{m}_{\mathrm{e}1}]$ and those in $[\mathbf{e}]$ and $[\mathbf{h}]$. These relations can be written as

$$\begin{bmatrix}\mathbf{e}\\ \mathbf{h}\end{bmatrix} = [\mathbf{C}][\mathbf{m}_{\mathrm{e}1}] + \begin{bmatrix}\mathbf{e}\\ \mathbf{h}\end{bmatrix}_0, \tag{2.3}$$

with $[\mathbf{C}]$ being of dimensions $N_{\mathrm{tot}}^{\mathrm{FEM}} \times D$. The matrix $[\mathbf{C}]$ is evaluated during the calculation of matrices $[\mathbf{Y}_k]$ in the same way, column by column, exciting the respective subsystem by a single coefficient in $[\mathbf{m}_{\mathrm{e}1}]$ at the time, with the computed coefficients of $\mathbf{E}$ and $\mathbf{H}$ thus filling the respective column of the matrix $[\mathbf{C}]$, and stored to be used for subsequent calculation of the final solution.

The excitations $[\mathbf{j}_{\mathrm{e}k}]_0$ and $\begin{bmatrix}\mathbf{e}\\ \mathbf{h}\end{bmatrix}_0$ in (2.2) and (2.3) are found as the responses of a given subsystem stipulating that all coefficients in $[\mathbf{m}_{\mathrm{e}k}]$ are set to zero, while the original excitation is turned on. By the standard FEM and MoM analysis, we calculate the coefficients of $\mathbf{J}_{\mathrm{e}}$, $\mathbf{E}$, and $\mathbf{H}$, which constitute, in the numerical sense, the respective column-matrices $[\mathbf{j}_{\mathrm{e}k}]_0$ and $\begin{bmatrix}\mathbf{e}\\ \mathbf{h}\end{bmatrix}_0$. Relations in (2.2) and (2.3) will be discussed in the following sections with specifics given for both FEM and MoM solvers.

In order to obtain the solution of the original electromagnetic problem, in Fig. 2.2a, using matrices that represent different subsystems in (2.2) and (2.3), we relate the diakoptic

coefficients of $\mathbf{J}_e$ and $\mathbf{M}_e$ on the diakoptic boundary between FEM and MoM subsystems as follows:

$$-[\mathbf{j}_{e1}]=[\mathbf{j}_{e2}]=[\mathbf{j}_e],\quad -[\mathbf{m}_{e1}]=[\mathbf{m}_{e2}]=[\mathbf{m}_e], \tag{2.4}$$

where we utilized the facts that the equivalent sources in (2.1) have opposite signs and that the directions of vectors **n** in Figs. 2.1b and 2.1c are opposite. Note that the mutual relations connecting the diakoptic coefficients obtained for the interior side of the diakoptic surface for any subsystem must also be satisfied on the surface outside that subsystem. This property is further used when combining (2.2) and (2.4) to arrive to the following diakoptic matrix system of equations:

$$([\mathbf{Y}_1]-[\mathbf{Y}_2])[\mathbf{m}_e] = -[\mathbf{j}_{e1}]_0+[\mathbf{j}_{e2}]_0, \tag{2.5}$$

whose solution is $[\mathbf{m}_e]$. This system of equations is solved with a direct solver (i.e., the system is LU factorized, using partial pivoting with row interchanges, and then forward and backward substitutions are performed), since it is dense in the general case. The diakoptic coefficients in $[\mathbf{j}_{ek}]$, $k=1,2$, are then computed from $[\mathbf{m}_e]$ using (2.2), and the coefficients in $[\mathbf{e}]$ and $[\mathbf{h}]$, for subsystems in Figs. 2.2b and 2.2c, are obtained from (2.3). Once we have these latter coefficients, we can calculate the electromagnetic field at any point in space, as well as any other quantity of interest for the original electromagnetic structure, in Fig. 2.2a.

2.2.2. Double-Higher-Order Magnetic-Field FEM Diakoptic Implementation

The diakoptic method described in the previous sections is now applied in conjunction with double-higher-order FEM and MoM solvers based on higher order geometrical modeling and higher order field/current modeling. In specific, the building block for volumetric modeling in FEM subsystems (Fig. 2.2b) is a Lagrange-type interpolation generalized hexahedron of arbitrary

geometrical orders K_u, K_v, and K_w (K_u, K_v, $K_w \geq 1$), shown in Fig. 2.3a and analytically described as [6]

$$\mathbf{r}(u,v,w) = \sum_{i=0}^{K_u} \sum_{j=0}^{K_v} \sum_{k=0}^{K_w} \mathbf{r}_{ijk} L_i^{K_u}(u) L_j^{K_v}(v) L_k^{K_w}(w), \quad L_i^{K_u}(u) = \prod_{\substack{l=0 \\ l \neq i}}^{K_u} \frac{u - u_l}{u_l - u_i}, \quad -1 \leq u,v,w \leq 1, \quad (2.6)$$

where $\mathbf{r}_{ijk} = \mathbf{r}(u_i, v_j, w_k)$ are position vectors of interpolation nodes and $L_i^{K_u}(u)$ represent Lagrange interpolation polynomials in the u coordinate, with u_i being defined as $u_i = (2i - K_u)/K_u$, $i = 0,1,...,K_u$, and similarly for $L_j^{K_v}(v)$ and $L_k^{K_w}(w)$.

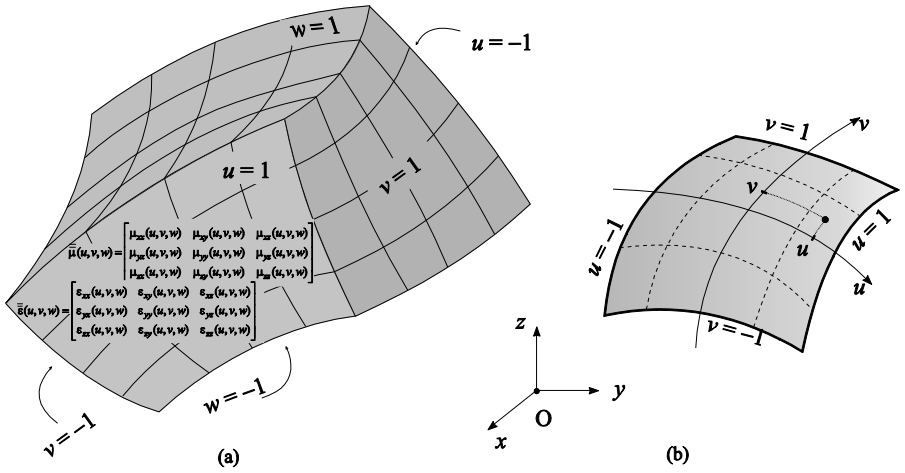

Figure 2.3. Lagrange-type curved parametric elements for higher order FEM-MoM-diakoptic analysis (Fig. 2.2) of inhomogeneous anisotropic dielectric and magnetic scatterers: (a) generalized FEM hexahedron, defined by (2.6), and (b) generalized MoM quadrilateral patch.

The same polynomials in (2.6) are used to describe the continuous spatial variations of both the complex permittivity and permeability tensors, $\bar{\bar{\varepsilon}}(u,v,w)$ and $\bar{\bar{\mu}}(u,v,w)$, of an inhomogeneous anisotropic material filling the generalized hexahedral element in Fig. 2.3a, as proposed in [28]. In specific, the *xx*-component of $\bar{\bar{\varepsilon}}$ is incorporated in the FEM model as

$$\varepsilon_{xx}(u,v,w) = \sum_{m=0}^{M_u} \sum_{n=0}^{M_v} \sum_{p=0}^{M_w} \varepsilon_{xx}^{mnp} L_m^{M_u}(u) L_n^{M_v}(v) L_p^{M_w}(w), \tag{2.7}$$

where M_u, M_v, and M_w ($M_u, M_v, M_w \geq 1$) are arbitrary material-representation polynomial orders (independent from K_u, K_v, and K_w), $\varepsilon_{xx}^{mnp} = \varepsilon_{xx}(\mathbf{r}_{mnp})$ are the respective permittivity values at interpolation nodes $\mathbf{r}_{mnp}$ corresponding to orders M_u, M_v, and M_w, and similarly for all remaining components of $\bar{\bar{\varepsilon}}$ and for all components of $\bar{\bar{\mu}}$.

The diakoptic surface enclosing each of the FEM domains is modeled using Lagrange-type generalized curved parametric quadrilaterals, in Fig. 2.3b [10], which are surface two-dimensional (2-D) versions of the hexahedron in Fig. 2.3a, and are conformal with the sides of hexahedra belonging to the diakoptic surface [8].

In this work, we utilize the *H*-field FEM formulation (except in the last example, where the E-field FEM formulation is used) and expand the magnetic field by means of curl-conforming hierarchical polynomial vector basis functions of arbitrary field-expansion orders N_u, N_v, and N_w ($N_u, N_v, N_w \geq 1$) introduced in [6]. Furthermore, in the field expansion, basis functions that possess tangential components at the boundary (marked by "boundary") are distinguished from those that do not ("interior"), as described in [2]:

$$\mathbf{H} = \sum_{i=1}^{N_{\text{tot}}^h} \mathbf{h}_i \mathbf{f}_i = \sum_{i=1}^{N_{\text{INTERIOR}}} \mathbf{h}_{\text{I}i} \mathbf{f}_{\text{I}i} + \sum_{i=1}^{N_{\text{BOUNDARY}}} \mathbf{h}_{\text{B}i} \mathbf{f}_{\text{B}i}. \tag{2.8}$$

Boundary volume basis functions are further used to generate divergence-conforming surface basis functions as $\mathbf{n} \times \mathbf{f}_{\text{B}i}\big|_S$, for expanding the diakoptic surface currents in the following form [19]:

$$\mathbf{J}_{\mathrm{e}} = \mathbf{n} \times \mathbf{H}\Big|_S = \sum_{i=1}^{N_{\mathrm{BOUNDARY}}} \mathbf{j}_{\mathrm{e}i} (\mathbf{n} \times \mathbf{f}_{\mathrm{B}i})\Big|_S , \tag{2.9}$$

$$\mathbf{M}_{\mathrm{e}} = -\mathbf{n} \times \mathbf{E}\Big|_S = \sum_{i=1}^{N_{\mathrm{BOUNDARY}}} \mathbf{m}_{\mathrm{e}i} (\mathbf{n} \times \mathbf{f}_{\mathrm{B}i})\Big|_S , \tag{2.10}$$

where $\mathbf{n}$ is adopted to be the outward looking unit normal to the enclosed diakoptic surface *S*.

In order to numerically establish the matrix relationships in (2.2), the FEM solver discretizes a Galerkin-type weak form of the curl-curl magnetic-field vector wave equation,

$$\int_V (\nabla \times \mathbf{f}_i) \cdot \left(\bar{\bar{\varepsilon}}_{\mathrm{r}}^{\ -1} \nabla \times \mathbf{H} \right) \mathrm{d}V - k_0^2 \int_V \mathbf{f}_i \cdot \left(\bar{\bar{\mu}}_{\mathrm{r}} \mathbf{H} \right) \mathrm{d}V = \mathrm{j}k_0 \oint_S \mathbf{f}_i \cdot (\mathbf{n} \times \mathbf{E}) \mathrm{d}S , \tag{2.11}$$

with $k_0 = \omega\sqrt{\varepsilon_0 \mu_0}$ being the free-space wave number (ω is the angular frequency of the time-harmonic excitation in the system). This discretization leads to a matrix equation with the unknowns coefficients being only those describing boundary variables,

$$[F_{\mathrm{BB}} - F_{\mathrm{BI}} (F_{\mathrm{II}}^{\ -1} F_{\mathrm{IB}})] [\mathbf{h}_{\mathrm{B}}] = -\mathrm{j}k_0 \left[\langle \mathbf{f}_{\mathrm{B}}, \mathbf{n} \times \mathbf{f}_{\mathrm{B}} \rangle \right] [\mathbf{m}_{\mathrm{e}}], \tag{2.12}$$

and in which the connection in (2.10) is employed on the right-hand side of the equation such that magnetic diakoptic sources can numerically be considered as excitation of the system. In (2.12), F_{BB}, F_{BI}, F_{IB}, and F_{II} are the submatrices of a well-known FEM matrix [6], with F_{IB}, for instance, standing for the submatrix corresponding to testing functions belonging to a set of the interior FEM functions and basis functions being the boundary functions, and the operator $\langle \mathbf{a}, \mathbf{b} \rangle$ is a standard surface integral of a dot product of vector variables $\mathbf{a}$ and $\mathbf{b}$. Note that while the matrix $\left[\langle \mathbf{f}_{\mathrm{B}}, \mathbf{n} \times \mathbf{f}_{\mathrm{B}} \rangle \right]$ in (2.12) is ill-conditioned, this does not deteriorate the overall accuracy of the method, as shown in examples presented in this paper (and evaluated in other cases that are not shown).

Next, boundary coefficients in the expansion of the magnetic field are equated to the appropriate electric-current coefficients, using (2.9), so that a diakoptic linear relation in (2.2)

can be established by inverting the system matrix in (2.12). Denoting the local diakoptic matrix of the i-th FEM subsystem in Fig. 2.2b by $[\mathbf{Y}_1^i]$, and the corresponding source column-matrices by $[\mathbf{m}_\mathrm{e}^i]$ and $[\mathbf{j}_\mathrm{e}^i]$, we have

$$[\mathbf{Y}_1^i][\mathbf{m}_\mathrm{e}^i]=[\mathbf{j}_\mathrm{e}^i],\quad [\mathbf{Y}_1^i]=-\mathrm{j}k_0[F_{\mathrm{BB}}-F_{\mathrm{BI}}(F_{\mathrm{II}}{}^{-1}F_{\mathrm{IB}})]^{-1}\left[\langle \mathbf{f}_\mathrm{B},\mathbf{n}\times\mathbf{f}_\mathrm{B}\rangle\right],\quad i=1,2,\ldots,N_{\mathrm{FEM}}, \qquad (2.13)$$

and the global diakoptic matrix $[\mathbf{Y}_1]$ given in (2.5) is then assembled using the local matrices as follows:

$$[\mathbf{Y}_1]=\begin{array}{c} \\ D_1\updownarrow \\ D_2\updownarrow \\ \vdots \\ D_{N_{\mathrm{FEM}}}\updownarrow \end{array}\begin{array}{c} \begin{array}{cccc} D_1 & D_2 & \cdots & D_{N_{\mathrm{FEM}}} \end{array} \\ \begin{array}{cccc} \leftrightarrow & \leftrightarrow & & \leftrightarrow \end{array} \\ \begin{bmatrix} \mathbf{Y}_1^1 & & & \\ & \mathbf{Y}_1^2 & & \\ & & \ddots & \\ & & & \mathbf{Y}_1^{N_{\mathrm{FEM}}} \end{bmatrix} \end{array}. \qquad (2.14)$$

Once the diakoptic excitations $[\mathbf{m}_\mathrm{e}]$ are found from (2.5), the magnetic field inside each of the FEM domains can be calculated based on (2.3), using $[\mathbf{C}]$, which in turn, can easily be obtained from (2.11) in terms of appropriate local matrices in the same fashion as in (2.14).

In cases where the original electromagnetic system, in Fig. 2.2a, is subdivided into a number of touching FEM subsystems, the adjacent subsystems touch each other through parts of the diakoptic surface, which is meshed in a way that a generalized quadrilateral patch belonging to one side of the common area has its match on the opposite side, i.e., the meshes on opposite sides of the diakoptic surface are conformal. Even though spatial positions of touching quadrilaterals are the same, independent subsystems are pre-processed separately. In this setup, the touching quadrilaterals need to have opposite orientations, that is, the directions of normal vectors n should be opposite to one another, which is ensured by a simple adjustment of the two local parametric coordinate systems for the two coinciding patches. Next, touching subsystems are

assumed to be immersed in the air-filled open-region subsystem, and hence an infinitesimally thin layer of air is considered to exist between the touching quadrilaterals. Consequently, touching FEM domains influence each other through a MoM domain, where a numerical solver is applied to a structure consisting of touching and other surfaces. The only issue with applying the MoM solver relates to the calculation of singular and hyper-singular Galerkin impedance matrix elements [10], due to the mutual contributions of surface currents belonging to two touching surfaces. Since touching surfaces (faces of the adjacent diakoptic domains), although belonging to two distinct diakoptic domains, actually share a unique surface in space, the corresponding Galerkin impedances are computed by applying a self-integration procedure, with testing and basis functions belonging to the two distinct surfaces coinciding in space. Namely, the singularity extraction method for calculation of singular and hyper-singular MoM operators [10], [29], [5] is utilized. Note also that in the case of touching domains, matrix is not diagonal-dominant, and it influences the final matrix obtained by the diakoptic method. Note, finally, that any other FEM and/or MoM numerical discretization is possible within the framework of the diakoptics, including low-order elements and bases.

2.3. Numerical Results

A special parallel version of the FEM-MoM-diakoptic solver based on the message passing interface (MPI) basic linear algebra communication subprograms (BLACS) is developed, and run on a CrayXT6m platform. The Cray supercomputer used for simulations contains 52 compute nodes, with a total of 104 AMD Magny Cours 64-bit 1.9-GHz processors (two per node), where each processor has 12 cores. A 32-GB RAM memory is available on each node, while the interconnection between the nodes is SeaStar2+ with 2D torus topology.

2.3.1. 2-D Array of Dielectrically Coated PEC Spherical Scatterers

As the first example of the application and validation of the new diakoptic method, consider a 2-D array of 4×4 dielectrically coated spherical perfect-electric-conductor (PEC) scatterers, depicted in Fig. 2.4. For each scatterer, the PEC sphere radius is r = 100 mm and the thickness and relative permittivity of the coating are d = 35 mm and $\varepsilon_r = 4$, respectively, while the center-to-center distances between adjacent scatterers are s = 400 mm. The original system is divided into 17 diakoptic subsystems, with 16 FEM subsystems modeling individual spherical scatterers and one open-region MoM subsystem. The geometrical model of each spherical scatterer is comprised of six FEM curvilinear hexahedra of the second geometrical orders ($K_u = K_v = K_w = 2$) modeling the dielectric coating, with PEC boundary conditions on the inner surfaces and six curvilinear quadrilateral patches on the outer surfaces, coinciding with the adopted diakoptic boundary. The adopted field approximation orders in all FEM hexahedra are $N_w = 2$ in the radial direction and $N_u = N_v = 4$ in other two (transversal) directions, and these latter orders are used for current expansions on the MoM patches (on the diakoptic boundaries) as well. This results in a total of D = 3,072 diakoptic unknowns.

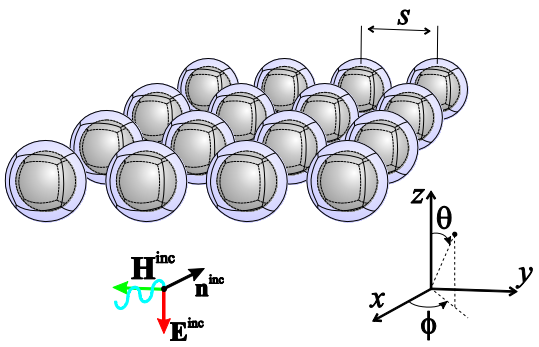

Figure 2.4. 2-D array of dielectrically coated spherical PEC scatterers.

Fig. 2.5 presents the normalized bistatic radar cross section (RCS), σ_{3D}/λ_0^2 (λ_0 henceforth being the free-space wavelength), of the array at a frequency $f = 0.5\,\mathrm{GHz}$ as a function of the scattered angle in two characteristic plane cuts. The excitation wave is incident from the direction defined by $\theta_{inc} = 90°$ and $\varphi_{inc} = 0$, where θ and φ are angular coordinates in the spherical coordinate system shown in Fig. 2.4. The same (θ, φ) notation will be used in all examples in this section. We observe an excellent agreement of diakoptic results with the solution obtained by WIPL-D (pure-MoM commercial software), which serves as a reference. The total number of unknowns used for modeling in WIPL-D is 9,216. The approximately three times reduction in the number of the diakoptic unknowns, when compared with the commercial higher order MoM software, comes from the implemented geometrically higher order modeling and the diakoptic compression. Note also that the analysis of this problem using a low-order variant of the proposed diakoptic method, with first-order (rooftop) basis functions on patches that are not larger than $\lambda/10$ in each dimension (with λ being the wavelength in the dielectric medium), would require D = 19,200 diakoptic unknowns, and about 244 times longer time to solve the matrix system of equations and about 39 times larger RAM memory for the simulation than the presented higher order diakoptic solution.

In addition, shown in Fig. 2.5 are the RCS results for the same geometry and frequency but with the dielectric coating being made from a continuously inhomogeneous dielectric material whose relative permittivity undergoes a linear radial variation from $\varepsilon_r = 4$ at the PEC boundary to $\varepsilon_r = 10$ at the outer surface of the scatterer. The higher order geometrical and numerical model is the same as in the previous case but with $M = 1$ in (2.7) for the local radial direction to model the dielectric inhomogeneity. The solution using the continuously inhomogeneous FEM-MoM-diakoptic model is compared with a WIPL-D solution for a three-layer piecewise

homogeneous approximate model of the dielectric coating (with equivalent permittivities calculated as the mean value of the inhomogeneous profile for each of the equally thick layers), which takes 51,712 unknowns, and a good agreement of the two sets of results is observed.

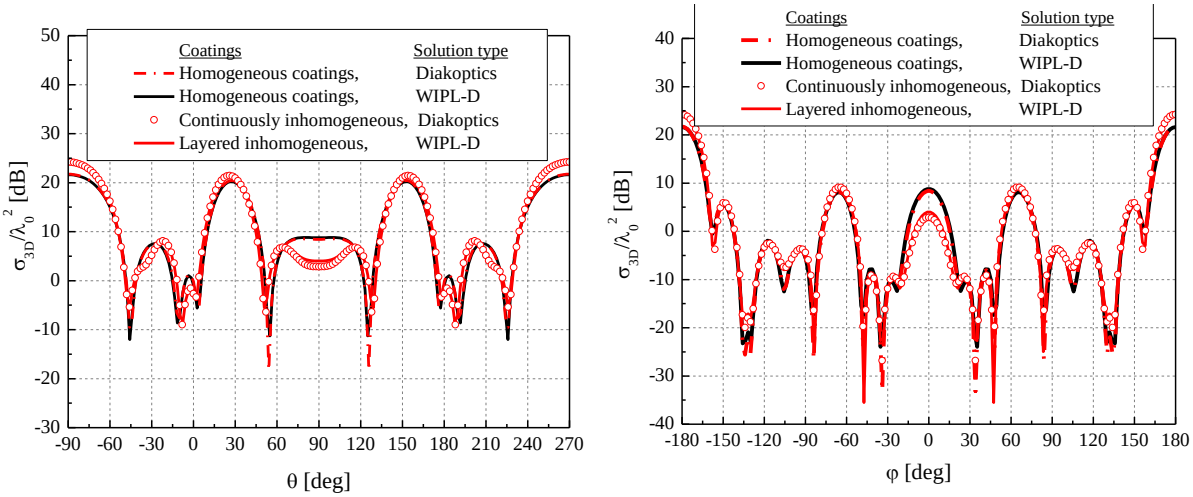

(a) (b)

Figure 2.5. Normalized bistatic radar cross section of the array of scatterers in Fig. 2.4, for homogeneous and continuously inhomogeneous dielectric coatings, respectively, computed by the FEM-MoM-diakoptic method and by the pure-MoM commercial software WIPL-D: (a) $\varphi = 0$ cut and (b) $\theta = 90°$ cut.

The total computation time for the FEM-MoM-diakoptic analysis of scatterers with both the homogeneous and continuously inhomogeneous dielectrics (in Fig. 2.5) is 2 min 27 sec and the RAM memory used for the storage of the diakoptic matrices is 288 MB, running the parallel code on a 2×2-process grid, all processes are on a single compute node

2.3.2. Dielectric Scatterer Modeled by Multiple Touching FEM Domains

As the next example, we consider a dielectric (ε_r = 2.25) brick-shaped scatterer, shown in Fig. 2.6, illuminated by a uniform plane wave incident from the direction defined by $\theta_{inc} = 90°$ and

$\varphi_{\text{inc}} = 0$, with electric and magnetic field vectors given by $\mathbf{E}^{\text{inc}} = -1\mathbf{i}_z$ V/m and $\mathbf{H}^{\text{inc}} = -\eta_0^{-1}\mathbf{i}_y$ A/m at the global coordinate origin, where $\eta_0 = \sqrt{\mu_0 / \varepsilon_0}$ stands for the free-space intrinsic impedance. The operating frequency is f = 250 MHz. We model the brick by four adjacent cubical FEM elements, each with edge length a = 1 m and each being enclosed by the diakoptic surface with air as the outer medium. All elements in the model are of the first geometrical order (K_u = K_v = K_w = 1), whereas the orders of the field expansions (in all FEM elements in all directions) and current expansions (on all square MoM patches surrounding each of the FEM subdomains) are all the same and equal to 5. The total number of unknowns in the final system of equations is D = 1,200, while the total number of unknown coefficients used for magnetic field expansion is $N_{\text{tot}}^{h} = 2{,}160$.

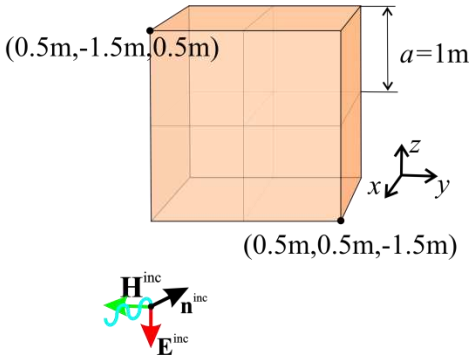

Figure 2.6. Brick-shaped dielectric scatterer modeled by four touching cubical FEM diakoptic subsystems.

Shown in Fig. 2.7a is the computed real part of H_y in the FEM domains, in the vertical plane defined by x = 0, placed in the middle of the scatterer. For comparison, the same solution obtained by WIPL-D is shown in Fig. 2.7b as a reference. We can conclude from the figure that the agreement of the diakoptic results with the reference results is very good. Running the code in a single process, the FEM-MoM-diakoptic solution takes 56 sec of simulation time and uses 43.9 MB of RAM memory to store the diakoptic matrices.

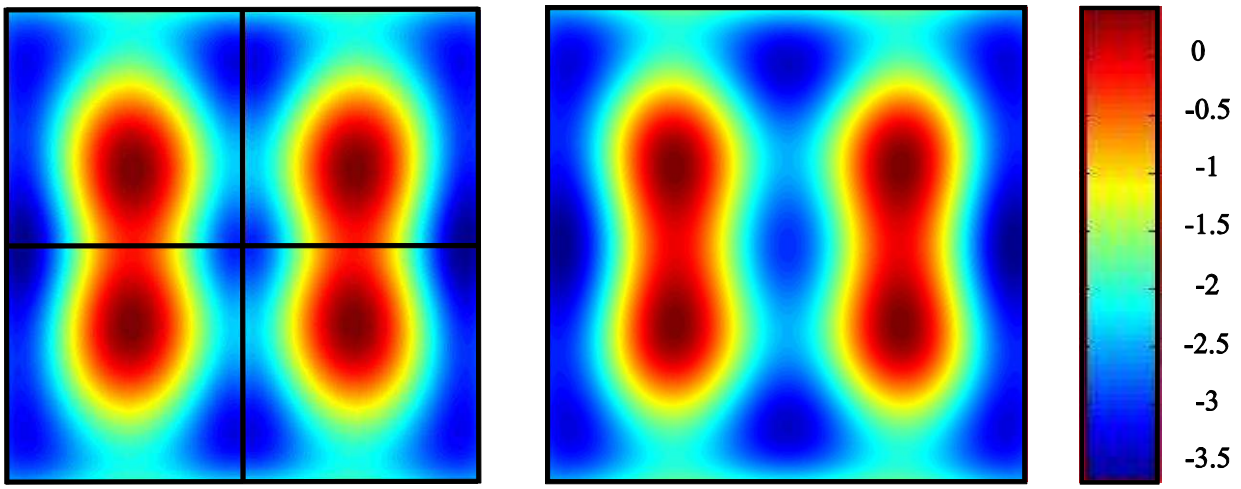

Figure 2.7. Real part of the internal magnetic field component H_y in the vertical plane ($x = 0$) in the middle of the scatterer in Fig. 2.6 obtained by (a) the FEM-MoM-diakoptic method and (b) the WIPL-D; The color-bar units are mA/m.

2.3.3. 3-D Array of Cubical Dielectric Scatterers

Next, consider a three-dimensional (3-D) array of cubical dielectric scatterers shown in Fig. 2.8. The cube edges and side-to-side distances between neighboring cubes amount to $a = s = 1\lambda_0$, and the relative permittivity of the dielectric is $\varepsilon_r = 2.25$. The structure is modeled by 513 diakoptic subsystems (512 FEM domains and one open-region MoM domain). The volume and surface elements in the model are of the first geometrical orders, $K_u = K_v = K_w = 1$, while the field and current expansion orders are all the same and equal to 3. The size of the system of diakoptic equations is $D = 55{,}296$.

Fig. 2.9 displays two characteristic normalized bistatic RCS plane cuts for uniform plane wave excitation of the system shown in Fig. 2.8, with the results obtained by the diakoptic method being compared with the reference WIPL-D solution. We observe from the figure an excellent agreement of the two sets of results. The total number of unknowns used for modeling

in WIPL-D is 24,576. Similarly to the first example, when comparing the diakoptic approach to the pure MoM solution (by commercial software), the reduction in the number of unknowns in the final system of equations is by 3.55 times.

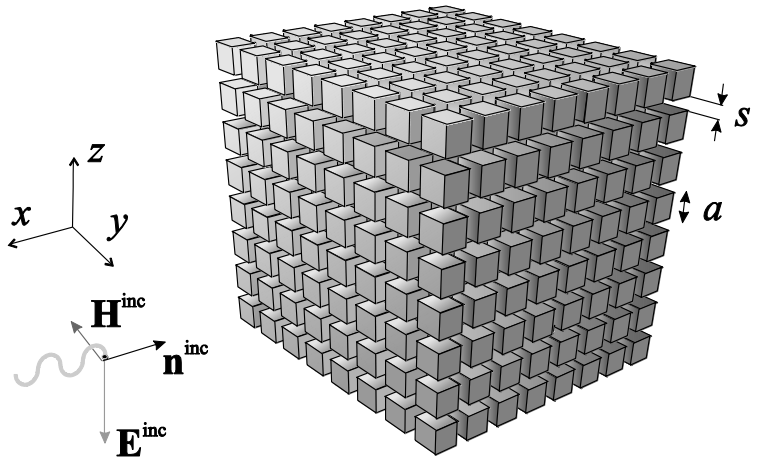

Figure 2.8. 3-D array of cubical dielectric scatterers.

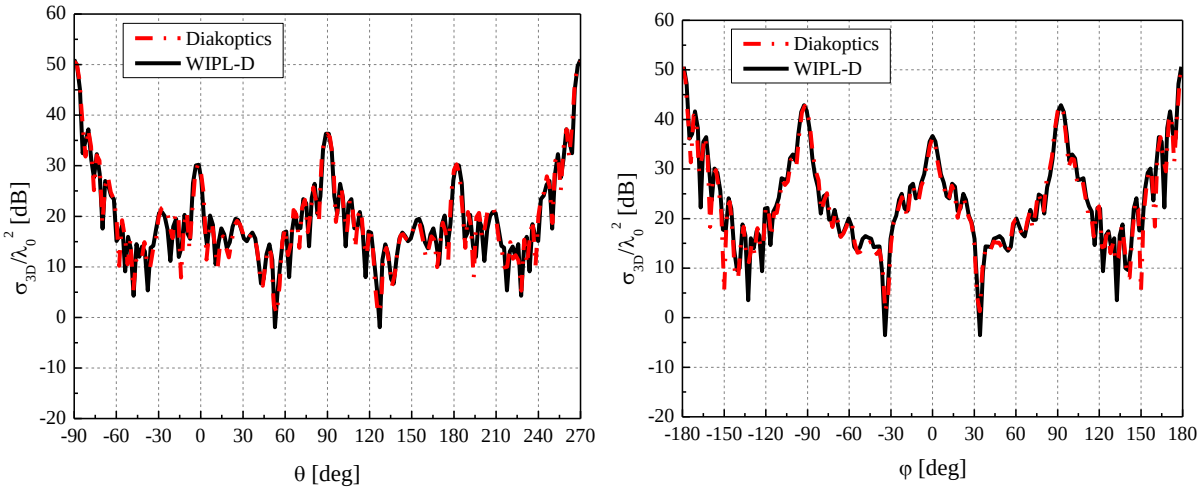

Figure 2.9. Normalized bistatic RCS of the array of scatterers in Fig. 2.8 obtained by the FEM-MoM-diakoptic method and by WIPL-D: (a) $\varphi = 0$ cut and (b) $\theta = 90°$ cut.

The total number of unknowns used for modeling in WIPL-D if no symmetries were exploited is 110,592. Similarly to the first example, when comparing the diakoptic approach to the pure

MoM higher order solution (WIPL-D), the reduction in the number of unknowns in the final system of equations is by two times. However, note that the higher order FEM-MoM-diakoptic method would allow modeling of inhomogeneous and/or anisotropic scatterers in the array in Fig. 2.8 at essentially the same computational cost. Running the FEM-MoM-diakoptic parallel code on a 16×16-process grid, on 16 compute nodes (16 processes per node), the simulation time is 30 min 12 sec and the RAM memory consumption for the storage of the diakoptic matrices is 91.1 GB. Note also that, when compared to the higher order diakoptic solution, the low-order diakoptic model specified in Section 2.3.i would require 7.11 times more diakoptic unknowns, about 358 times longer direct-solver solution time, and about 50 times larger RAM memory.

2.3.4. 2-D Array of PEC Spheres with Cloaking Dielectric/Magnetic Metamaterial Covers

The final example is a 2-D array of cloaked spherical PEC scatterers, depicted in Fig. 2.10. The radii of the PEC spheres are R_1 = 1 m, thicknesses of the cloaks are d = 0.1 m (outer radii of the cloaks are $R_2 = R_1 + d$), and distances between the scatterer centres are L = 5 m. Each transformation-based metamaterial spherical cloak relies on the theory derived in [13], whereas its detailed analysis by the higher order FEM-MoM can be found in [30]. The scatterer geometry and incident plane wave direction are shown in Fig. 2.10. In the FEM-MoM-diakoptic analysis, each of the cloaked regions is modeled by six curvilinear hexahedra of fourth geometrical orders, K_u = K_v = K_w = 4, enclosed by six quadrilaterals conformal to the outer cloak surface. The adopted field approximation orders are $N_u = N_v = N_w = 5$ for all FEM hexahedra, while the current approximation orders are $N_u = N_v = 4$ for all MoM patches. The total number of diakoptic unknowns amounts to D = 768. Continuous spatial variations of the medium tensors $\bar{\bar{\varepsilon}}$ and $\bar{\bar{\mu}}$ in the cloaked regions, obtained from the linear cloak transformation in the spherical (

r,θ,φ) coordinate system are given by [30]

$$\bar{\bar{\varepsilon}} = \bar{\bar{\mu}} = \begin{bmatrix} \dfrac{R_2(R_1 - r)^2}{(R_2 - R_1)r^2} & 0 & 0 \\ 0 & \dfrac{R_2}{R_2 - R_1} & 0 \\ 0 & 0 & \dfrac{R_2}{R_2 - R_1} \end{bmatrix}, \tag{2.15}$$

where R_1 and R_2 are the inner and outer radii, respectively, of the spherical cloak. The Cartesian equivalents of $\bar{\bar{\varepsilon}}$ and $\bar{\bar{\mu}}$ are implemented using (2.7) with $M_u = M_v = M_w = 6$.

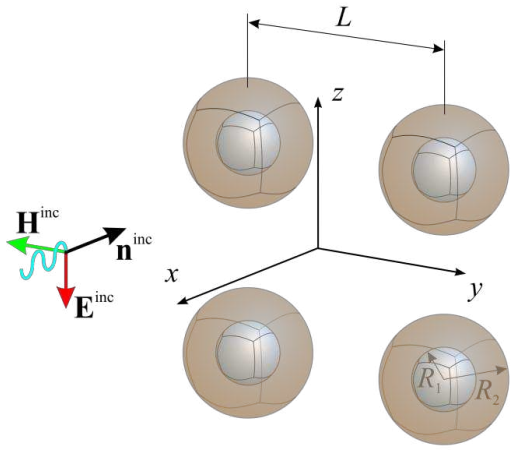

Figure 2.10. 2-D array of PEC spheres with cloaking metamaterial covers whose permittivity and permeability tensors are given in (2.15).

Shown in Fig. 2.11 is the normalized backscattering RCS of the array of cloaked spheres at f = 55 MHz obtained by the FEM-MoM-diakoptic method, in the $\varphi = 0$ plane. For the purpose of validation of the numerical solution, the computed RCS of the array of uncloaked PEC spheres, with the continuously inhomogeneous anisotropic FEM elements constituting the cloaking layer being replaced by homogeneous air-filled elements having all field and current expansions and other parameters in the FEM-MoM-diakoptic analysis the same as in the cloak model, is also shown in Fig. 2.11, where it is compared with the WIPL-D solution, and an

excellent agreement of the two sets of results is observed. In addition, while having in mind that the cloak is theoretically ideal (RCS theoretically vanishes), a WIPL-D solution for a homogeneous air-filled sphere is shown as a reference, giving a clear insight into what a typical numerical solution for the given geometry and an ideal invisibility material (scattering from free-space) would be. We observe from the figure, a very significant reduction in the numerically obtained scattering cross section of the array of cloaked spheres with respect to the array of PEC spheres; namely, the RCS is so low that it is on par with the best numerical approximation of the zero backscatter from an empty spherical region of the same size as the original scatterer, as verified by WIPL-D. The total number of FEM unknowns is $N_{\text{tot}}^{e} = 2{,}260$, (computation time: 24 min 5 sec, RAM memory: 18 MB, single process), while the total numbers of unknowns in WIPL-D simulations are 3,456 for the array of air-filled spheres and 1,728 for the array of PEC spheres.

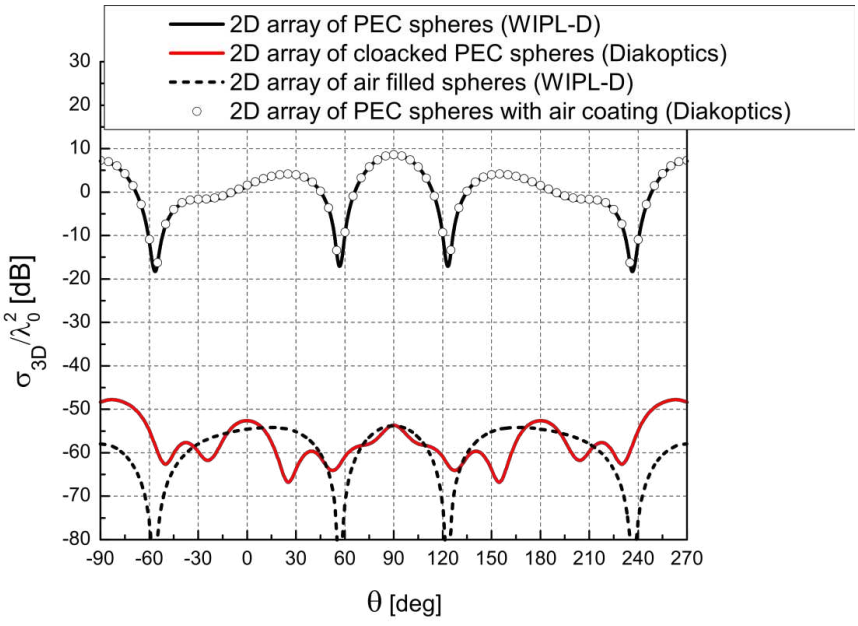

Figure 2.11. Normalized bistatic RCS in the $\varphi = 0$ plane of (i) the cloaked array in Fig. 2.10 computed using the FEM-MoM-diakoptics, (ii) the array of PEC spheres obtained by WIPL-D, (iii) the array of uncloaked spheres with the cloaks replaced by homogeneous air layers calculated by the FEM-MoM-diakoptics, and (iv) the array of homogeneous air-filled spheres obtained using WIPL-D.

2.4. Conclusions

This paper has presented a new FEM-MoM-diakoptic method for analysis of inhomogeneous anisotropic dielectric and magnetic scatterers in the frequency domain. The method splits the original electromagnetic system into a number of closed-region FEM diakoptic subsystems containing material complexities and an open-region MoM diakoptic subsystem. Each of the subsystems is analyzed completely independently applying FEM or MoM solvers, and the solution to the original problem is obtained from linear relations between coefficients in expansions of equivalent electric and magnetic surface currents on diakoptic boundary surfaces. The method implements large curved hexahedral finite elements, filled with inhomogeneous anisotropic materials. Diakoptic electric sources and the magnetic field in FEM subsystems are connected using dual sets of hierarchical polynomial vector basis functions explicitly satisfying the natural relation between curl-conforming and divergence-conforming quantities. A technique enabling touching of the subsystems, i.e., that the subsystems share a common diakoptic boundary, has been introduced in the diakoptic method.

The proposed higher order FEM-MoM-diakoptic method and its versatility, accuracy, and efficiency have been validated and demonstrated in several characteristic examples of finite arrays of dielectric, dielectric/magnetic, and dielectrically coated PEC scatterers. Numerical results include analysis of scatterers with straight edges and pronounced curvature, a scatterer modeled by multiple touching FEM diakoptic domains, and a transformation-based metamaterial cloaking structure, with the continuously inhomogeneous anisotropic cloaking region modeled using large curved finite elements that allow continuous spatial variations of complex permittivity and permeability tensors and high-order FEM field approximations.

3. EFFICIENT SCALABLE PARALLEL HIGHER ORDER DIRECT MOM-SIE METHOD WITH HIERARCHICALLY SEMISEARABLE STRUCTURES FOR 3D SCATTERING[3]

3.1. Introduction

Recent trends in computational electromagnetics (CEM), in applications that involve calculating, storing, and solving large and dense matrices, include applying fast, parallel (direct or iterative) solvers for the system of equations in conjunction with compressed storage of large matrices and their parts. Two general approaches emerge among fast methods attempting to reduce numerical and storage complexity: (i) the fast multipole method (FMM) [31] and (ii) *H*-matrices [32]–[34]. The idea behind both of them is to approximate the integral kernel by a degenerate kernel using so-called functional skeletons. In the case of multipole methods, these functions have to be known explicitly for each kernel, which means that the method and its behavior depend heavily on the physics behind the exact problem to be solved. On the other hand, in the case of algebraic methods, such as *H*-matrices, matrix blocks are approximated by low-rank matrices.

H-matrix algorithms were first introduced by Hackbusch [32]–[34], with their H^2-matrix version being introduced in [35], and have been used efficiently with fast LU based direct solvers or as preconditioners to fast iterative solvers. The *H*-matrix methods are kernel independent so they are suitable for application to any type of integral equation (IE) based formulation. In the

[3] Material included in this chapter is submitted to *IEEE Transactions on Antennas and Propagation:* © 2015 IEEE, A. B. Manić, François-Henry Rouet, Xiaoye Sherry Li, and Branislav M. Notaroš, "Efficient Scalable Parallel Higher Order Direct MoM-SIE Method with Hierarchically Semiseparable Structures for 3D Scattering, " submitted to *IEEE Transactions on Antennas and Propagation.*

CEM community, several applications of *H*-type direct solvers to tackle surface integral equation (SIE) problems are presented in [36]–[40].

Matrix compression solvers rely heavily on a type of the low-rank matrix approximation method such as singular value decomposition (SVD) [38], [41], rank-revealing QR (RRQR) decomposition [42], [43] or adaptive cross approximation (ACA), where ACA can be considered as rank-revealing LU (RRLU). ACA is well known and established method for fast matrix computation in CEM, introduced first to solve the low-frequency (quasistatic) IE problems [44], and then combined with different matrix compression methods to solve system of equations arising in high-frequency SIE methods [45]–[48].

In addition, semiseparable matrices, the ones that can easily be compressed and accurately approximated by their low-rank counterpart, and its application to Green's function integral kernel are discussed in [49]. In order to combine beneficial features of semiseparable matrices and *H*-matrix representation, the hierarchically semiseparable matrices are most recently introduced [50]. Solution of the two-dimensional (2D) SIE method of moments (MoM) using hierarchically semiseparable compression is discussed in [51], where the authors comment on the possible extension of their work to the 3D case.

On the other hand, it is well known that by using higher order basis functions for current/field modeling in CEM, significant reductions in the number of unknowns, as well as faster system matrix computation/solution, can be achieved [10] when compared to the traditional low order modeling [52]. Tightly coupled with using higher order basis functions is higher order geometry modeling [10], [26] and together they lay foundation to double higher order (DHO) modeling. The DHO approach has been effectively used in both direct and iterative MoM-SIE solvers [53]–[57].

Besides developing fast algorithms to solve MoM-SIE equations, the CEM researchers have intensely investigated parallelization of the fast algorithms coupled with direct solvers in order to speed up the simulations of electrically large electromagnetic structures. DHO MoM-SIE system matrix filling followed by the computationally expensive LU decomposition on a full matrix was implemented into parallel out-of-core hybrid GPU/CPU algorithm [56], while the performance of a similar method using higher order basis functions was investigated on more than 4,000 CPU cores on a distributed memory system [57]. Similarly, a parallel *H*-LU direct solver using hybrid MPI-OpenMP that builds on the ability to combine both shared and distributed memory programming was used to analyze 3D scattering problems with nearly 4 million unknowns [58]. Further, a parallel hierarchical ACA algorithm demonstrating an acceleration factor larger than 200 was presented in [59].

This paper proposes a novel fast scalable higher order parallel algorithm for large and complex scattering, radiation, and propagation problems in CEM based on the DHO MoM-SIE modeling in the frequency domain [10], [26], [12], [60] in conjunction with a direct solver for dense linear systems with hierarchically semiseparable structures (HSS) [61]. We are developing asymptotically fast higher order direct algorithms for MoM-SIE solutions which, in a nutshell, are an algebraic generalization to fast multipole methods. In addition to being fast, they offer a promise of being memory- and communication-efficient and amenable to extreme-scale parallel computing. The main advantage of the HSS algorithm is in the linear-complexity ULV-type factorizations (whereas the conventional LU decomposition has cubic complexity). Our work uses the recently developed new, state-of-the-art, algorithms for solving dense and sparse linear systems of equations based on the HSS method [61]. The new HSS algorithms have been demonstrated to have a dramatic advantage in terms of time and space complexity (e.g., ~70

times less memory for seismic imaging examples with matrix size $2.5 \cdot 10^5 \times 2.5 \cdot 10^5$) than the LU factorization algorithm, and to be extremely scalable. In addition, this paper employs a RRQR decomposition for the matrix (memory) compression. Its adaptive nature comes from the ability to use the stopping criteria, i.e., relative tolerance value/minimal rank, which allows for the method to store only the low-rank approximation of the original matrix that satisfies predefined accuracy. In order to enhance the HSS compression and parallelization, a method for geometrical preprocessing of the scatterers based on the cobblestone distance sorting technique [45] is utilized. Hence, the MoM unknowns having spatial locality (belonging to the same mesh group) also exhibit the data locality in the matrix system of equations. The basic theory and preliminary results of the DHO HSS-MoM-SIE analysis are presented in a summary form in [62].

HSS compression is implemented in a multilevel fashion as described in [61] and, essentially, its multilevel compression can be considered comparable to the one used in the MLACA algorithm [47]. Furthermore, so-called multilevel "butterfly" algorithms [63]–[64], as well as the fast solver presented in [65], have a similar basis to the multilevel compression coupled with low-rank matrix representation.

This paper is organized as follows. Section 3.2 gives an overview of the MoM-SIE methodology and the associated discretization using DHO modeling. In addition, geometrical preprocessing used to group surface quadrilaterals into mesh groups that achieves spatial-data locality in the system matrix is described. In Section 3.3, the HSS compression and the ULV factorization followed by the solution of the compressed matrix is discussed. The parallelization and communication between the processes in matrix filling and HSS compression/factorization is outlined in Section 3.4. Section 3.5 provides numerical results and discussion, followed by the conclusions in Section 3.6.

3.2. DHO MoM-SIE Modeling of Metallic Scatterers

One of the most general and best established approaches to solving scattering CEM problems is the one based on the method of moments in the surface integral equation formulation and the frequency domain (FD) [26]. Inherently, the MoM results in dense linear systems, so the HSS compression and solver are applied to allow for fast and memory efficient execution.

3.2.1. Surface Integral Equation Formulation

The MoM-SIE methodology is applicable to the analysis of metallic and dielectric structures, where both electric and magnetic surface currents are introduced over boundary surfaces between homogeneous parts of the structure, and surface integral equations based on boundary conditions for both electric and magnetic field intensity vectors are solved with current densities as unknowns. This paper focuses on metallic structures only. However, extending this work to include problems involving dielectrics is straightforward based on [10].

If the structure made of a perfect electric conductor (PEC) is excited by a time-harmonic electromagnetic field of electric field intensity $\mathrm{E}^{\mathrm{inc}}$ at the angular frequency ω, then the scattered field $\mathbf{E}^{\mathrm{scat}}$ can be expressed in terms of the surface electric currents of density $\mathbf{J}_{\mathrm{s}}$ using the boundary condition for the tangential fields at the surface *S* of the structure as follows:

$$\left(\mathbf{E}^{\mathrm{scat}}\left(\mathbf{J}_{\mathrm{s}}\right)+\mathbf{E}^{\mathrm{inc}}\right)_{\mathrm{tang}}=0\,,\ \mathbf{E}^{\mathrm{scat}}\left(\mathbf{J}_{\mathrm{s}}\right)=-\mathrm{j}\omega\mathbf{A}-\nabla\Phi \tag{3.1}$$

$$\mathbf{A}=\mu\int_{S}\mathbf{J}_{\mathrm{s}}\,g dS,\ \Phi=\frac{\mathrm{j}}{\omega\varepsilon}\int_{S}\nabla_{s}\cdot\mathbf{J}_{\mathrm{s}}\,g dS \tag{3.2}$$

where $\mathbf{A}$ and Φ are magnetic vector and electric scalar potential, respectively, $g=\mathrm{e}^{-\mathrm{j}\omega\sqrt{\varepsilon\mu}R}\big/4\pi R$, is the Green's function for the unbounded homogeneous medium with

parameters ε and μ, and R is the distance of the field point from the source point. Hence, (3.1) and (3.2) constitute an electric field integral equation (EFIE) for $\mathbf{J}_s$ as unknown quantity, which is discretized using the MoM.

3.2.2. Double Higher Order Modeling

Double higher order modeling consists of meshing the geometry of the electromagnetic structure using DHO surface elements, which means that both geometry as well as the unknown variable (surface current) are discretized using higher order functions. In specific, surface of the structure is modeled using generalized curved quadrilaterals of arbitrary geometrical orders K_u and K_v, shown in Fig. 3.1(a), and the current density $\mathbf{J}_s$ over quadrilaterals is approximated by means of hierarchical vector basis functions of arbitrarily high current-expansion orders N_u and N_v [10],

$$\mathbf{r}(u,v)=\sum_{k=0}^{K_u}\sum_{l=0}^{K_v}\mathbf{r}_{kl}L_k^{K_u}(u)L_l^{K_v}(v),\ -1\le u,v\le 1, \tag{3.3}$$

$$\mathbf{J}_s=\sum_{i=0}^{N_u}\sum_{j=0}^{N_v-1}\alpha_{ij}^{(u)}P_{ij}^{(u)}(u,v)\frac{\mathbf{a}_u}{\mathfrak{J}}+\sum_{i=0}^{N_u-1}\sum_{j=0}^{N_v}\alpha_{ij}^{(v)}P_{ij}^{(v)}(u,v)\frac{\mathbf{a}_v}{\mathfrak{J}} \tag{3.4}$$

arranged in a maximally orthogonalized fashion [66], [67] as illustrated in Fig. 3.1(b). Here, L represent Lagrange interpolation polynomials, r_{kl} are position vectors of interpolation nodes, P are divergence-conforming polynomial bases, $\mathfrak{J} = |\mathrm{a}_u \times \mathrm{a}_v|$ is the Jacobian of the covariant transformation, and $\mathrm{a}_u = \partial \mathrm{r}/\partial u$ and $\mathrm{a}_v = \partial \mathrm{r}/\partial v$ are unitary vectors along the parametric coordinates. The unknown current-distribution coefficients $\{\alpha\}$ in (3.4) are determined by solving the SIE in (3.1), employing Galerkin method. Double (geometrical and current) higher order modeling enables the use of large curved patches, which can greatly reduce the number of

unknowns for a given problem and enhance the accuracy and efficiency of the computation. Element orders in the model, however, can also be low, so the low-order modeling approach is actually included in the higher order modeling. Moreover, because our basis functions are hierarchical, a whole range of element sizes and shapes, geometrical orders, and current approximation orders can be used at the same time in a single simulation model of a complex structure using the high order (more precisely, low-to-high order) CEM technique.

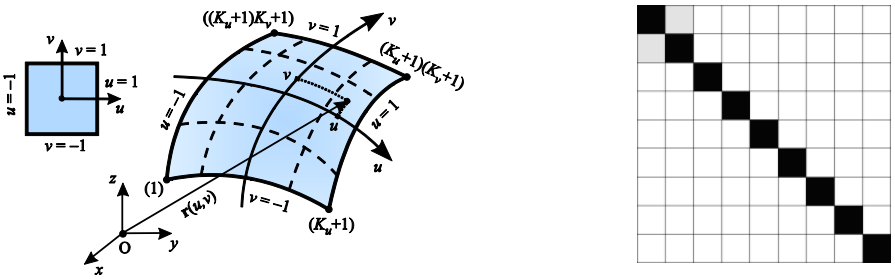

(a) (b)

Figure 3.1. a) Generalized curved parametric quadrilateral patch for DHO MoM-SIE modeling [10]. (b) Sketch of the orthogonality factor for maximally orthogonalized hierarchical basis functions of the eight order [66].

3.2.3. Geometrical Preprocessing Based on Cobblestone Distance Sorting Technique

The geometrical grouping of the quadrilaterals in the object mesh based on their spatial locality, as shown in Fig. 3.2, is done by applying the distance sorting technique [45] as outlined by the steps described in Fig. 3.3. The grouping technique ensures data locality in the dense system matrix, which is greatly beneficial for achieving the properties needed for the HSS compression. Specifically, the cobblestone distance sorting technique divides the mesh into N^g mesh groups. Each matrix sub-block determined by the coordinates (i,j) stores the interactions between MoM unknowns belonging to the i^{th} and j^{th} mesh groups. The mesh size of each mesh

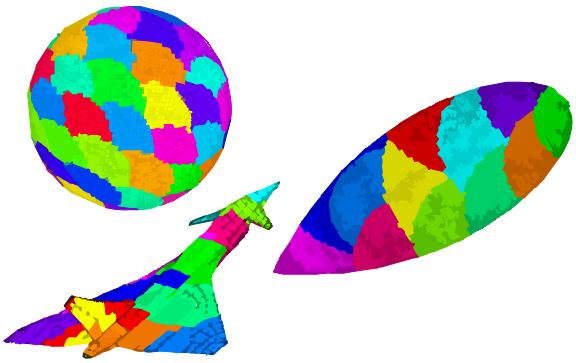

Figure 3.2 Illustration of geometrical preprocessing of objects based on the cobblestone distance sorting technique [45].

group (i.e., the number of unknowns) is predetermined by the number of processes, geometry, and other simulation specifics and is given as an input to the geometrical preprocessor. The outcome of the preprocessor is that MoM unknowns belonging to the same mesh group, besides its spatial locality, exhibit the data locality in the matrix system of equations: self-interaction blocks are on the diagonal, while near interactions tend to be closer to the diagonal and far interactions further away from the diagonal of the system matrix. It is well known that the numerical rank of the matrix block describing the interactions between two groups decreases with the increase of the distance between the groups [45], [68]. This matrix property plays a significant role in the HSS matrix compression.

Distance Sorting Technique:

for $k = 1 : N^g$

1. List all remaining (ungrouped) unknowns corresponding to basis functions on the quadrilateral mesh;
2. Create a box enclosing ungrouped mesh;
3. Find all projections of the remaining unknowns onto the vector defined by the diagonal of the box;
4. Define the group's "zero" point as the first unknown along the vector;
5. Sort all remaining unknowns based on the distance from the "zero" point;
6. Group the first N_k unknowns, where N_k is the predetermined number of unknowns in the k^{th} subgroup.

End

Figure. 3.3. The algorithm behind the cobblestone distance sorting technique [45], illustrated in Fig. 3.2.

3.3. HSS Theory

This section contains an overview of the HSS structures, their compression, factorization and solution, defined and explained in more detail in [61].

3.3.1. HSS Structures

HSS representations rely on a cluster tree T that defines a hierarchical clustering (or partitioning) of the index set [1; N], where N is the number of rows and columns of the matrix. A cluster tree is such that every node i is associated with an interval t_i . For each node $i \in T$ there is an index subset $t_i \subset [1;N]$, such that $t_{c1} \cap t_{c2} = 0$, $t_{c1} \cup t_{c2} = t_i$. At the root, $t_{2k-1} = I = [1:N]$. Consequently, $A_{|t_i \times t_j}$ is the submatrix of A with t_i and t_j being its row and column index subsets, respectively.

The HSS matrix form is defined (exists) on a corresponding cluster tree T (a.k.a. HSS tree. For simplicity we only consider binary trees). An L-level postordered T consists of $2k-1$ numbered nodes ($k = 2^{L-1}$), where the root (the only L^{th} level node) is labeled by $2k-1$, while k nodes are leaves (first level nodes). Further, each nonleaf node $i \in T$ has exactly two children nodes that satisfy relation $c1 < c2 < i$, with $c1$ and $c2$ being its left and right child, respectively. An example of the four-level HSS tree is given in Fig. 3.4.

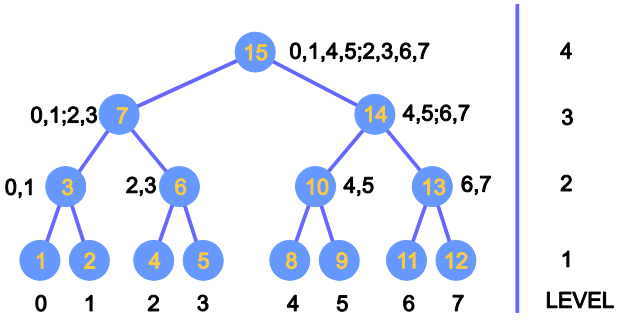

Figure. 3.4. Four-level postordered binary tree used in the HSS representation.

The maximum rank r (or numerical rank r for a given tolerance τ) of all HSS blocks is called the HSS rank of matrix A. Matrix A has a low-rank property and can be efficiently compressed and solved using the HSS algorithm if r is small comparing to the matrix size.

Compressed HSS representation is defined by using the so-called HSS generators D_i, U_i, R_i, B_i, W_i, and V_i, belonging to each node i of the tree, such that $D_{2k-1} = A$, while nonleaf node generators are constructed by using its children's generators as follows:

$$D_i = A_{|t_i \times t_i} = \begin{bmatrix} D_{c1} & U_{c1}B_{c1}V_{c2}^H \\ U_{c2}B_{c2}V_{c1}^H & D_{c2} \end{bmatrix}, \tag{3.5}$$

$$U_i = \begin{bmatrix} U_{c1}R_{c1} \\ U_{c2}R_{c2} \end{bmatrix}, \; V_i = \begin{bmatrix} V_{c1}W_{c1} \\ V_{c2}W_{c2} \end{bmatrix}, \tag{3.6}$$

where the superscript "H" denotes Hermitian transpose. Fig. 3.5 depicts a block example of the 8×8 HSS representation of a matrix defined on the corresponding HSS tree, given in the Fig. 3.4. Leaf level D matrices are calculated and stored as fully dense, while other matrices are calculated and saved in the compressed form obtained by the rank-revealing QR (RRQR) decomposition.

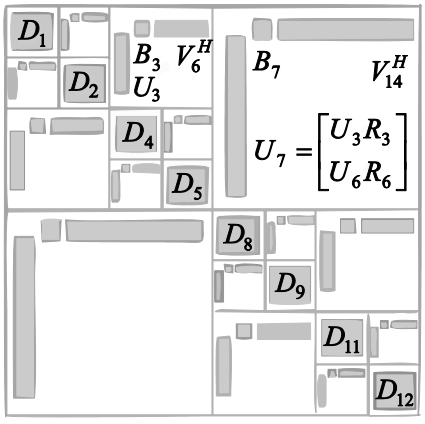

Figure 3.5. Illustration of a corresponding HSS form.

3.3.2. HSS Compression

HSS compression is done in two stages: row and column compression steps, where the latter one is applied to an already row-compressed matrix. RRQR decomposition is applied for compression of all the matrices [43]. The steps in the algorithm behind the RRQR decomposition are given in Fig. 3.6.

Rank-revealing QR decomposition:

Compression of a $M \times N$ matrix $A \approx QT$ with rank r and tolerance τ is given by following steps:

for $i = 1 : \min(M, N)$;

1. Find the column $f_j = A(:, j)$ with the maximum norm
2. Interchange f_i and f_j;
3. Set $t_{ii} = \|f_i\|_2$, if $t_{ii} / t_{11} \leq \tau$ then $r = i$, exit;
4. Calculate the i^{th} column of Q: $q_i = f_i / t_{ii}$;
5. Calculate the i^{th} row of T: $t_i^H = q_i^H [\, f_{i+1}, f_{i+2}, \ldots, f_N \,]$;
6. Update the rest of the matrix $[\, f_{i+1}, f_{i+2}, \ldots, f_N \,] = [\, f_{i+1}, f_{i+2}, \ldots, f_N \,] - q_i t_i^H$.

End

Figure 3.6. Rank-revealing QR algorithm.

Row compression step is applied in an upward sweep along the HSS tree, where at each leaf level node i, a local block row of the system matrix $A_{|t_i \times I}$ is calculated as explained in Section 3.2. Afterwards, initial RRQR decomposition is done and column block U_i HSS generators are defined at leaf level nodes. In the next step along the HSS tree, a local matrix is defined using children's matrices and compressed as given in (3.7) and (3.8) and outlined in the row compression algorithm in Fig. 3.7. The algorithm is applied in a recursive fashion along the HSS tree, and the row compression stage is accomplished once the root node is reached.

In a similar fashion, column compression is applied in an upward sweep as given in the column compression algorithm in Fig. 3.8. A block column matrix $A_{\tilde{t}_i \times t_i}$ that was already

compressed at the row compression stage is associated with each node *i* and column compressed as given in (3.10) and (3.11). Construction of the matrix *A* HSS form and all its generators is obtained after the column compression stage. Note that the compression of the right-hand side is done in the same fashion as the compression of the system matrix.

Row compression algorithm:

1. At the leaf level, row compression of the local matrix is calculated on each node *i*: $A_{|t_i \times (I \setminus t_i)} \approx U_i A_{|\hat{t}_i \times (I \setminus t_i)}$;

2. At each non-leaf level, matrices of interest are defined by children's matrices and compressed ((3.7) and (3.8)). Children's local matrices *R* are stored, while the matrix block forwarded to the parent node is $A_{|\hat{t}_i \times (I \setminus t_i)}$,

$$A_{|t_{c1} \times t_{c2}} \approx U_{c1} A_{|\hat{t}_{c1} \times t_{c2}},\ A_{|t_{c2} \times t_{c1}} \approx U_{c2} A_{|\hat{t}_{c2} \times t_{c1}}, \tag{3.7}$$

$$F_i = \begin{pmatrix} A_{|\hat{t}_{c1} \times (I \setminus t_i)} \\ A_{|\hat{t}_{c2} \times (I \setminus t_i)} \end{pmatrix} \approx \begin{pmatrix} R_{c1} \\ R_{c2} \end{pmatrix} A_{|\hat{t}_i \times (I \setminus t_i)}. \tag{3.8}$$

Figure 3.7. Row compression algorithm.

Column compression algorithm:

1. At the leaf level, let us define $\bar{t}_i$ on each node *i* as:

$$\bar{t}_i = \bigcup_{l=1}^{L-1} \hat{t}_{sib(ances(i,l))}, \tag{3.9}$$

where *sib*(*i*) stands for a sibling node while *ances*(*i*,*l*) is the ancestor of the node *i* at the level *l*. The column compression of the local matrix is calculated:

$$A_{|\bar{t}_i \times t_i} \approx A_{|\bar{t}_i \times \tilde{t}_i} V_i^H; \tag{3.10}$$

2. At each non-leaf level matrices of interest are defined by children's matrices and compressed further,

$$G_i = \begin{pmatrix} A_{|\bar{t}_i \times \tilde{t}_{c1}} & A_{|\bar{t}_i \times \tilde{t}_{c2}} \end{pmatrix} = A_{|\bar{t}_i \times \tilde{t}_i} \begin{pmatrix} W_{c1} \\ W_{c2} \end{pmatrix}^H, \tag{3.11}$$

$$B_{c1} = A_{|\hat{t}_{c1} \times \tilde{t}_{c2}},\ B_{c2} = A_{|\hat{t}_{c2} \times \tilde{t}_{c1}}. \tag{3.12}$$

Figure 3.8. Column compression algorithm.

3.3.3. ULV HSS Factorization and Solution

The *ULV* factorization is applied to the HSS compressed form of the matrix *A* in (3.5) in order to find orthogonal (*U*,*V*) and triangular (*L*) matrices. The factorization is done by multiplying the local matrix given in (3.5) at the node *i* by specially constructed *Q* and *P* matrices,

$$\begin{bmatrix} Q_{c1}^H & 0 \\ 0 & Q_{c2}^H \end{bmatrix} \begin{bmatrix} D_{c1} & U_{c1}B_{c1}V_{c2}^H \\ U_{c2}B_{c2}V_{c1}^H & D_{c2} \end{bmatrix} \begin{bmatrix} P_{c1}^H & 0 \\ 0 & P_{c2}^H \end{bmatrix} \tag{3.13}$$

Q matrices are formed by the *QL* factorization of column blocks *U* matrices in order to introduce zero off-diagonal row blocks:

$$U_{c1} = Q_{c1}\begin{bmatrix} 0 \\ \tilde{U}_{c1} \end{bmatrix}, U_{c2} = Q_{c2}\begin{bmatrix} 0 \\ \tilde{U}_{c2} \end{bmatrix}, \tag{3.14}$$

where $\tilde{U}_{ck}, k = 1,2$ are lower triangular matricies of size r_{ck}, r_{ck} being the rank of the U_{ck} matrix. *Q* matrices are used further to define $\hat{D}_{ck} = Q_{ck}^H D_{ck}, k = 1,2$, which are conveniently partitioned as:

$$\hat{D}_{ck} = \begin{bmatrix} \hat{D}_{ck;1,1} & \hat{D}_{ck;1,2} \\ \hat{D}_{ck;2,1} & \hat{D}_{ck:2,2} \end{bmatrix}, k = 1,2., \tag{3.15}$$

so that $\hat{D}_{ck;2,2}$ is a square matrix of size equal to r_{ck}. Finally, *P* matrices are defined by the following *LQ* factorization:

$$\begin{pmatrix} \hat{D}_{ck;1,1} & \hat{D}_{ck;1,2} \end{pmatrix} = \begin{pmatrix} \tilde{D}_{ck;1,1} & 0 \end{pmatrix} P_{ck}. \tag{3.16}$$

Applying (3.14)-(3.16) and using orthogonality properties of involved *P* and *Q* matrices, (3.13) may be expressed in a new form:

$$\begin{bmatrix} \begin{bmatrix} \tilde{D}_{c1;1,1} & 0 \\ \tilde{D}_{c1;2,1} & \tilde{D}_{c1;2,2} \end{bmatrix} & \begin{bmatrix} 0 \\ \tilde{U}_{c1} B_{c1} \begin{bmatrix} \tilde{V}_{c2;1}^H & \tilde{V}_{c2;2}^H \end{bmatrix} \end{bmatrix} \\ \begin{bmatrix} 0 \\ \tilde{U}_{c2} B_{c2} \begin{bmatrix} \tilde{V}_{c1;1}^H & \tilde{V}_{c1;2}^H \end{bmatrix} \end{bmatrix} & \begin{bmatrix} \tilde{D}_{c2;1,1} & 0 \\ \tilde{D}_{c2;2,1} & \tilde{D}_{c2;2,2} \end{bmatrix} \end{bmatrix}. \tag{3.17}$$

Note that all non-zero off-diagonal blocks in (3.17) are of small dimensions relative to the full matrix dimension. At this stage, it is easy to redefine parent generators using only a small part of children's generators,

$$D_i = \begin{bmatrix} \tilde{D}_{c1;2,2} & \tilde{U}_{c1} B_{c1} \tilde{V}_{c2;2}^H \\ \tilde{U}_{c2} B_{c2} \tilde{V}_{c1;2}^H & \tilde{D}_{c2;2,2} \end{bmatrix}, U_i = \begin{bmatrix} \tilde{U}_{c1} R_{c1} \\ \tilde{U}_{c2} R_{c2} \end{bmatrix}, V_i = \begin{bmatrix} \tilde{V}_{c1;2} W_{c1} \\ \tilde{V}_{c2;2} W_{c2} \end{bmatrix}. \tag{3.18}$$

Note also that, for example, a square matrix D_i is still saved in the compressed fashion as before but its new dimension is only $r_{c1} + r_{c2}$, while after the HSS compression stage it was $sizeof(t_{c1} \cup t_{c2})$.

Algorithm described in (3.13)-(3.18) is then performed in an upward sweep. When the root node is reached, an LU factorization with partial pivoting is performed on a square dense matrix of a dimension far smaller than the starting matrix. Once (3.18) is solved on the parent node, it is straightforward to use (3.17) and calculate children's solutions. Solving the matrix is done in a downward sweep and the final solution is obtained when the leaf level is reached.

3.4. Parallelization Strategy

The parallelization strategy of the HSS-MoM-SIE method is adopted from [61] for HSS compression and solution and from [69] for MoM-SIE matrix filling. Communication method between the processes is adopted to be the same as the communication layer of state-of-the-art dense linear algebra library ScaLAPACK [70]: BLACS (Basic Linear Algebra Communication Subprograms) library [71]. Further, both libraries are used for execution of all linear algebra computations applied to full storage dense matrices.

MoM-SIE matrix filling is done as given in Section II, where the parallel matrix filing builds on top of the cobblestone geometrical processing as introduced in [69]. If the total number of processes running the simulation is N_{procs}, then number of mesh groups used in the preprocessing is $N^g = \sqrt{N_{procs}}$. Further, each process can be described by its 2D coordinates (p, q) where p, $q = 1..N^g$ and the local matrix calculated by the (p, q) process corresponds to the SIE interactions between the p-th and q-th mesh group.

Matrix calculation and initial RRQR compression are done at the leaf level, where the 2D process grid is divided into k subgrids, with each subgrid belonging to one leaf level node and defining the node's process context. Each of the k subgrids is of size $N^g/k \times N^g$, as shown in Fig. 3.9.

Processes belonging to one leaf-level node i context are used to calculate $A_{|t_i \times I}$, where A is the MoM-SIE system matrix, and its corresponding excitation vector set. All matrices are stored using the so-called distributed 2D block cyclic storage on a 2D process grid on a distributed memory systems [70]. Further, when two of the nodes at the same level have overlapping calculations, the calculations are non-redundantly done only on one node's context and efficiently forwarded to the other node using BLACS communication routines. Following this, all the calculations done at children's nodes needed at any of the parent's nodes are forwarded in the upward sweep along the HSS tree.

After the calculation of the local matrices at the leaf-level nodes, generators D_i are stored, while the initial parallel RRQR compression is done to obtain U_i and R_i matrices, as given in the first step of the HSS compression (Fig. 3.7). All HSS operations (HSS compression, ULV factorization and solution) are performed in parallel, either in upward or downward sweep along the HSS tree [61]. At upper levels in the HSS tree, each node uses all children's processes to

define its own context. For example, as shown in Fig. 3.4, at the third HSS level, nodes 7 and 14 are children to the fourth level node 15 and their corresponding 2×2 2D process grids: {0,1; 2,3} and {4, 5; 6,7} are combined together into 2×4 2D process grid: {0, 1, 4, 5; 2, 3, 6, 7}. The parent context is obtained by combining the two children's contexts either side by side or one on top of the other, because the size of both children's contexts is the same. At each node, matrices are stored using the 2D block cyclic storage defined for the current node context [69]. Computations done on each of the HSS generators are performed in parallel where each process is running computations on its local matrix "chunk." Throughout the computation phases, intracontext sequences of communication are done to ensure that the data needed for accurate computation is available to each process. After computation at the current node, preparation for the following step is done: both intracontext and intercontext data exchange and matrix redistribution for the new context needed on the next level of the traversal along the HSS tree.

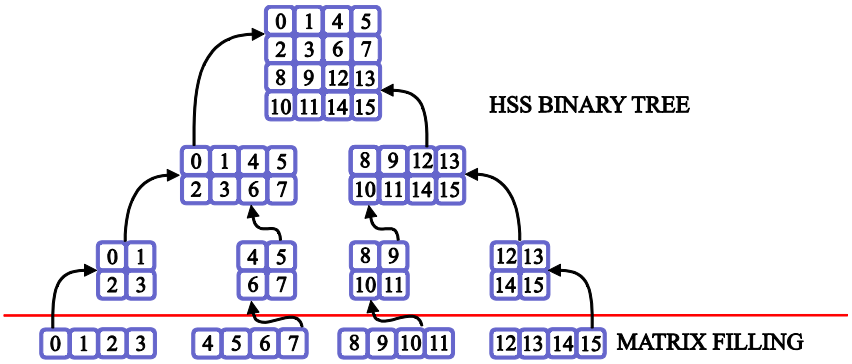

Figure 3.9. Illustration of a process context change throughout matrix filling phase and HSS solver on a level 3 HSS tree and using 16 processes.

Details behind the communication at each step in the parallel HSS solver can be found in [61]. Some of the examples of intracontext communication throughout the computation phase are the following: In the RRQR algorithm, when finding the norm of each column, norm of each local column is found and then BLACS function for summing the norms in a column-wise fashion on a 2D process grid is used. Afterwards, a similar row-wise communication function finds the

maximal norm and communicates it to all context processes. Such communication subroutines are the standard "combine operation" BLACS subroutines. Each participating process contributes data that is combined with data of other processes to produce a final result.

Similarly, the example of matrix redistribution is given in preparation of the next step moving up the HSS tree from level 3 to level 4. Two children's matrices are merging, as well as their contexts to define parent's matrix and a corresponding context. Due to the 2D block cyclic distribution of matrices, the data exchange when contexts {0, 1; 2, 3} and {4, 5; 6, 7} are switched to {0, 1, 4, 5; 2, 3, 6, 7} is achieved by the following pairwise data exchanges: $0 \leftrightarrow 4$, $1 \leftrightarrow 5$, $2 \leftrightarrow 6$, and $3 \leftrightarrow 7$.

3.5. Numerical results and Discussion

This section provides numerical results obtained by the DHO HSS-MoM-SIE analysis. All simulations were run on the TACC Stampede supercomputer that was accessed through The Extreme Science and Engineering Discovery Environment (XSEDE) [72]. Stampede has 6400 compute nodes where each node contains two Xeon Intel 8-Core 64-bit E5-processors (16 cores on each node). The core frequency is 2.7 GHz and supports 8 floating-point operations per clock period with a peak performance of 21.6 GFLOPS/core or 346 GFLOPS/node. Each node contains 32 GB of memory (2 GB/core). Nodes are interconnected with Mellanox FDR InfiniBand technology in a 2-level fat-tree topology [73].

3.5.1. Example 1: Spherical Scatterer

As the first example of the application as well as the validation of the HSS-MoM-SIE method, consider the analysis of scattering from a PEC sphere of diameter $d = 4.666\lambda_0$, with λ_0 being the

free-space wavelength. First, consider a higher-order mesh of the scatterer, maximal specified size of which is to be less than or equal to a wavelength. After the meshing procedure, the patch size s is approximately $0.9\lambda_0 \leq s \leq 0.95\lambda_0$ for all 96 geometrically second-order ($K_u = K_v = 2$) curvilinear quadrilateral patches modeling the sphere. The adopted current approximation orders are $N_u = N_v = 4$, which results in a total of $N = 3{,}072$ MoM-SIE unknowns. Fig. 3.10 shows the normalized bistatic radar cross section (RCS), σ_{3D}/λ_0^2 , as a function of the scattered angle, in two characteristic plane cuts. The excitation plane wave is incident from the direction defined by $(\theta_{inc},\phi_{inc}) = (90°,0)$, where θ and ϕ are angular coordinates in the spherical coordinate system. For the set of results given in Fig. 3.10, number of levels in the full postordered HSS tree is chosen to be 5, which contains 16 leaves, while the number of processes used in the parallel simulation is 64. In the same figure, we observe the convergence of the results to the analytical Mie solution with the decrease of τ, the RRQR relative tolerance (used in the HSS compression).

In addition, Table 3.1 provides the information on the average error, maximal rank, memory consumption, and total simulation time (including matrix filling, compression, factorization, and solution times) for different simulations given in Fig. 3.10. The average error is obtained as the average of the absolute error between the normalized bistatic RCS calculated by the numerical method and by the analytical Mie's series, respectively. The averaging is done by taking into account the error in a number (N^{dir}) of directions describing the bistatic RCS plane,

$$\zeta = \frac{1}{N^{\text{dir}}} \sum_{i=0}^{N^{\text{dir}}} \left| \sigma_i^{\text{num}} - \sigma_i^{\text{MIE}} \right| / \lambda_0^2. \tag{3.19}$$

Based on the convergence of different graphs given in Fig. 3.10, as well as the average errors given in Table 3.1, it can be concluded that the accuracy of the results is easy to control by the relative tolerance or maximal rank used in the RRQR. In addition, by inspecting the results given

in Fig. 3.10 and Table 3.1, as well as the results of the wide range of performed simulations (different tree levels and RRQR relative tolerance) using the same higher order model, scattering results for the PEC sphere that can readily be considered as accurate are obtained in simulations with the maximal rank $r \geq 490$. Maximal rank in the HSS compression corresponds to the maximal number of independent degrees of freedom (DoFs) needed for an accurate numerical simulation [74]. The number of DoFs needed to accurately model a scatterer should depend solely on the scatterer properties and not on the used discretization [63, 68, 74].

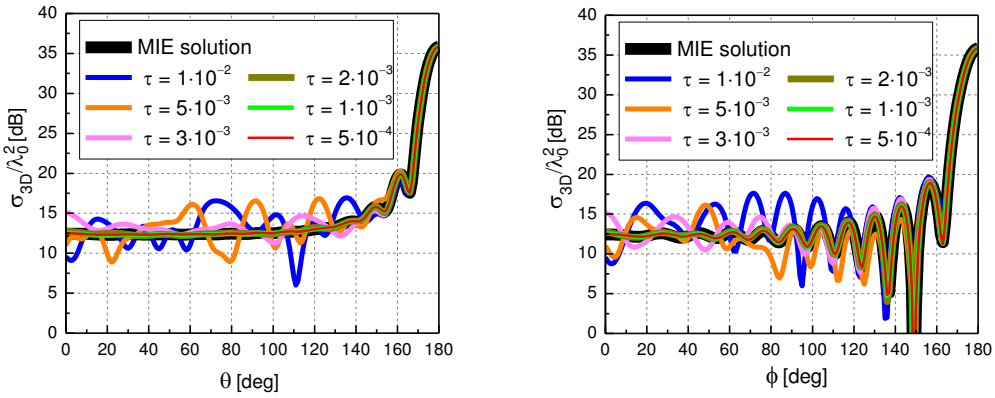

Figure 3.10. Normalized bistatic radar cross section of a spherical PEC scatterer computed by the HSS-MoM-SIE method using preprocessed mesh given in the Fig. 2 and by the Mie's series: (a) $\phi = 0$ cut and (b) $\theta = 90°$ cut.

TABLE 3.1
SIMULATION PARAMETERS FOR THE RESULTS GIVEN IN FIG. 3.10

RRQR rel. tolerance	Maximal rank	Time [s]	Storage [GB]	ζ [dB] ($\phi = 0$ cut)	ζ [dB] ($\theta = 90°$ cut)
$\tau = 1{\cdot}10^{-2}$	385	7.76	0.04	1.4964	2.2911
$\tau = 5{\cdot}10^{-3}$	433	8.00	0.05	1.3417	1.5164
$\tau = 3{\cdot}10^{-3}$	464	8.21	0.06	0.7309	0.9651
$\tau = 2{\cdot}10^{-3}$	493	8.27	0.06	0.0875	0.1567
$\tau = 1{\cdot}10^{-3}$	531	8.79	0.07	0.0319	0.0518
$\tau = 5{\cdot}10^{-4}$	575	8.92	0.08	0.0170	0.0403

Further analysis that compares low- and high-order modeling results shows the advantage of higher order modeling when capturing the real rank of the scattering problem. In particular, the

adopted low-order model of the same PEC scatterer consists of 7,776 geometrically first-order ($K_u = K_v = 1$) quadrilaterals with the maximal size of $0.12\lambda_0$. The adopted current approximation orders are $N_u = N_v = 1$, resulting in a total of $N = 15{,}552$ unknowns. After the initial discretization, when compared to the higher order model, the number of unknowns in the low-order model is more than 5 times larger. However, due to the physical properties of the scatterer, the maximal numerical rank of the compressed HSS matrix should be approximately the same for both models.

On the other hand, Fig. 3.11, shows the error, $\sigma_i^{\text{num}} - \sigma_i^{\text{MIE}}$, in the RCS for three choices of low-order simulations and one higher-order simulation, confirming that in order to achieve similar accuracy, a low-order simulation needs almost twice as large numerical rank. This is confirmed by the information in Table 3.2 that contains the average error for the four simulations given in Fig. 3.11.

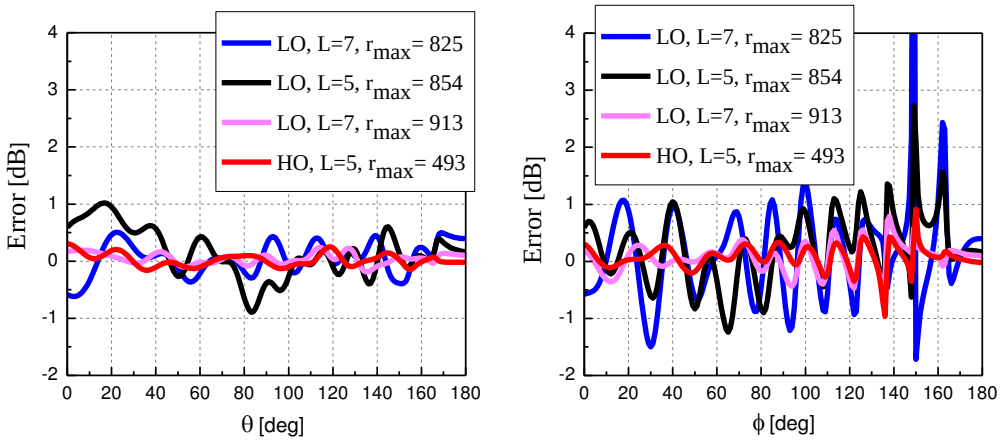

Figure 3.11. Error of the normalized bistatic RCS of the PEC scatterer computed by the HSS-MoM-SIE method with respect to the exact Mie solution: (a) $\phi = 0$ cut and (b) $\theta = 90°$ cut.

Further, note that the true low-order modelling based on RWG functions [31] defined over flat triangular patches uses from 500 to 600 unknowns per square wavelength [47, 48, 75], which

leads to a truly low order model of a PEC sphere with around 35,000 to 40,000 unknowns, making the number of unknowns more than 10 times larger than in the adopted HO model.

Next, we test the scalability performance of the HSS-MoM-SIE method – in the same example. Because the higher order model with only 96 quadrilaterals is not well fitted for simulations on hundreds of processes, the scalability testing of the method is done on a low-order model of the sphere. All simulations used in the test are set up for the tolerance $\tau = 5 \cdot 10^{-4}$ and level 5 full postordered HSS tree. Note that the number of leaves in the tree is 16, which, for the particular example, corresponds to the minimal number of processes that can be used in a parallel run of the HSS-MoM-SIE code. The runtime of the parallel code on 16 processes is thus adopted to be the baseline computational time used in the speed-up calculations. To measure scalability, we run the same model on 64, 256, and 1,024 processes, and observe an excellent scalability performance in Fig. 3.12.

TABLE 3.2
SIMULATION PARAMETERS FOR THE RESULTS GIVEN IN FIG. 3.11

Model type	Maximal rank	ζ [dB] (ϕ = 0 cut)	ζ [dB] (θ = 90° cut)
High Order	493	0.0875	0.1567
Low Order	825	0.2353	0.6521
	854	0.3541	0.5108
	913	0.0845	0.1947

3.5.2. Example 2: NASA Almond

In the second example, the HSS-SIE-MoM code is applied to analyze scattering from a NASA almond [76], an established benchmarking structure for monostatic RCS computations. In specific, we consider a PEC almond of the maximal size 42 λ_0 at a frequency of 50 GHz, with the overall surface of the scatterer being equal to $1{,}111\,\lambda_0^2$. The constructed higher order model of the almond uses a total of 16,384 curvilinear quadrilateral elements with $K_u = K_v = 2$ and the

current approximation in different directions on different patches ranging from $N_{u/v} = 1$ to $N_{u/v} = 3$ depending on the electrical dimensions of the quadrilateral element. The final number of unknowns (that would be even smaller if larger patches and even higher $N_{u/v}$ were used) is 149,756. A similar scatterer is analyzed in [75] using the model with around 450,000 unknowns. In addition, applying, for comparison, the true lower order quadrilateral modeling to the almond scatterer requires 524,288 unknowns defined over 262,144 patches with $K_u = K_v = 1$ and $N_{u/v} = 1$ on all the patches.

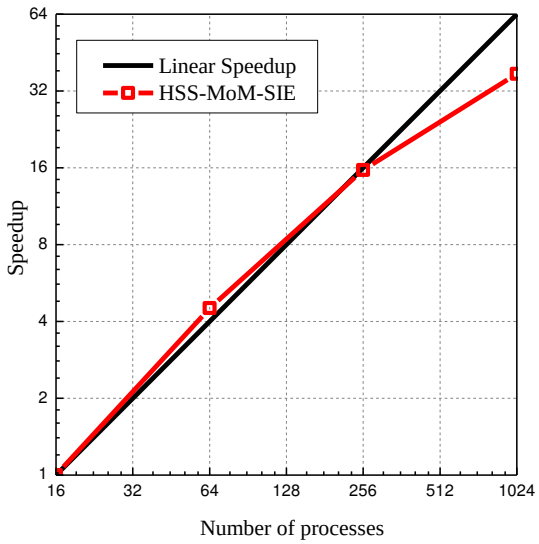

Figure 3.12. Performance and scalability of the HSS-MoM-SIE method applied to the simulation of a low-order PEC sphere model with the number of levels in the HSS tree equal to 5.

Fig. 3.13 shows the monostatic scattering computations of the DHO model of the PEC almond obtained by the HSS-MoM-SIE method and validated by the full-storage direct solver using ScaLAPACK LU decomposition [69] simulation of the same model, as well as against the low-order modeling results [75]. The normalized monostatic RCS is calculated for 361 different directions, in the $z = 0$ plane, with the polarization of the incident electric field along the z-axis.

The HSS compression is done using the relative tolerance $\tau = 3 \cdot 10^{-4}$ on the 5^{th} level HSS tree. The maximal rank of the compressed matrix comes out to be 3,926. The simulation is run in

parallel on 256 processes, with matrix calculation and HSS compression times being 846 s and 2,596 s, respectively. Further, the HSS factorization time is 41.95 s, while the total backsubstitution time for all 361 excitation vectors is 5.36 s. ScaLAPACK LU decomposition time on the same number of processes is 8,565 s, which, in terms of the performance can be compared to total time of the HSS compression and factorization: 2,638 s. The compressed matrix storage in the DHO HSS-MoM-SIE simulation amounts to 20.78 GB, while the full matrix storage for the same model would require 180 GB of memory. In addition, the LO quadrilateral model described above would require 2.2 TB. Hence, we observe great advantages of the DHO modeling coupled with the direct solver and HSS compression of the MoM-SIE matrix in the analysis of electrically large objects with multiple excitations (right-hand side values).

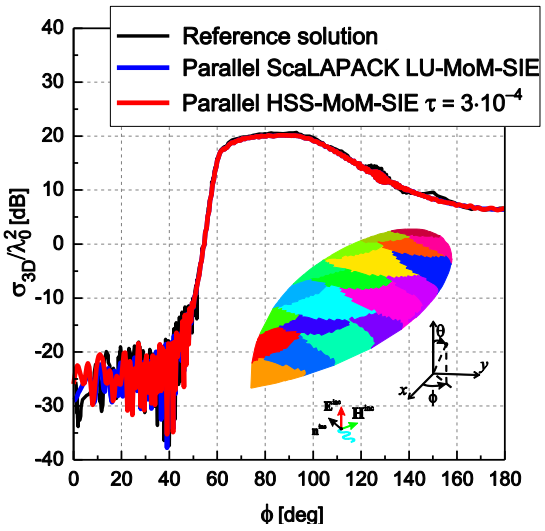

Figure. 3.13. Normalized monostatic RCS of a PEC NASA almond computed at 50 GHz by the full-storage direct ScaLAPACK LU-MoM-SIE and HSS-MoM-SIE methods.

3.6. Conclusions

This paper has proposed a novel fast scalable parallel algorithm and solver for large scattering problems based on double (geometrical and current-approximation) higher order MoM in the SIE

formulation and the frequency domain in conjunction with a direct solver for dense linear systems with hierarchically semiseparable structures, namely, with a HSS matrix representation for compression, factorization, and solution of the system matrix. In addition, a RRQR decomposition for memory compression has been used, with a stopping criterion in terms of the relative tolerance value/minimal rank, allowing for the method to store only the low-rank approximation of the original matrix that satisfies predefined accuracy. In order to enhance the HSS compression and parallelization, a method for geometrical preprocessing of the scatterers based on the cobblestone distance sorting technique has been employed, such that the MoM unknowns belonging to the same mesh group and thus having spatial locality also exhibit the data locality in the matrix system of equations.

Numerical examples have shown how the accuracy of the DHO HSS-MoM-SIE method is easily controllable by using the relative tolerance for the matrix compression. Moreover, the examples have demonstrated low memory consumption, as well as much faster simulation time, when compared to the direct LU decomposition. Finally, great scalability of the algorithm has been demonstrated on more than thousand processes.

Overall, the DHO HSS-MoM-SIE method and its future extensions and advancements are asymptotically faster direct algorithms for IE solutions that are memory and communication-efficient and amenable to extreme-scale parallel computing. They also are purely algebraic and kernel-independent and enable dramatically faster monostatic scattering computations than iterative solvers and reduced number of unknowns when compared to low-order discretizations.

This paper has focused on metallic scatterers. Nonetheless, due to the truly algebraic nature of the method, its extension to any electromagnetic system solved by the MoM-SIE analysis is straightforward.

4. DUFFY METHOD FOR EVALUATION OF SINGULAR POTENTIAL INTEGRALS OVER CURVED QUADRILATERALS WITH HIGHER ORDER BASIS FUNCTIONS IN SIE ANALYSIS OF ANTENNAS AND SCATTERERS[4]

4.1. Introduction

In analysis of antennas and scatterers based on the method of moments (MoM) in conjunction with the surface integral equation (SIE) approach [10], one of the most important problems in the development of a MoM-SIE technique and its implementation and optimization aimed to result in an accurate and efficient modeling and computational tool is the treatment of singular potential two-dimensional (2-D) integrals involved in the self-terms of the Galerkin impedance matrix, with the testing patch coinciding with the source patch, namely, when an observation (testing) point belongs to the source patch (with basis functions). This problem is even more pronounced and challenging when higher order basis functions are used for the approximation of surface currents of the antenna/scatterer, and especially when such functions are defined on curved surface (boundary) elements (patches) employed for geometrical modeling of the structure [5].

Most of the previous research in overcoming the problem of singular integrals in MoM-SIE modeling has been devoted to handling the singularities on planar triangular patches with low-order current approximations, typically in the form of Rao-Wilton-Glisson (RWG) basis functions [77]–[83]. Several works, on the other hand, deal with the problem of evaluation of

[4] © 2014 IEEE. Reprinted, with permission, from A. B. Manic, M. Djordjevic, and B. M. Notaros, "Duffy Method for Evaluation of Weakly Singular SIE Potential Integrals over Curved Quadrilaterals with Higher Order Basis Functions," *IEEE Transactions on Antennas and Propagation*, Vol. 62, No. 6, June 2014.

singular potential integrals for curved quadrilateral patches with higher order basis functions [10], [5], [84]–[88]. In particular, singularity extraction (subtraction) consisting of analytical integration of a principal singular part of the integrand and numerical integration of the residual using quadrature formulas [77] and it is implemented for RWG triangles in [78],[79], and for curved quadrilateral elements with higher order hierarchical polynomial vector basis functions in [10], [5].

Singularity cancellation methods for evaluation of singular integrals are based on coordinate transformations, i.e., on mapping of the integration domain to a new parametric domain such that the Jacobian of the transformation cancels out the singular term in the integrand. As a typical representative of this approach, the Duffy method [89], originally proposed for a volumetric integration domain [90], is applied to evaluation of singular integrals over planar [80] and curvilinear triangles [87], [88]. A polar transformation method for singularity cancellation is proposed for planar triangles with RWG functions [81]. Its implementation for singular potential integrals over curved quadrilateral elements with higher order hierarchical polynomial bases is given in [84], where a comparison of this technique and the singularity extraction method [10], [5] is presented as well. Rectangular transformation methods for singularity cancellation, first proposed for curved volume MoM elements [91], are applied to solve potential integrals over curved quadrilateral elements with higher order hierarchical polynomial bases in [85] and [86]. The arcsinh transformation method is applied for evaluating singular and near-singular potential integrals over flat triangular and quadrilateral MoM-SIE patches [82]. Singularity cancellation methods for computation of singular and near-singular potential integrals for flat triangles and linear basis functions using four different transformations are compared in [83].

Overall, there seems to be a lack of investigations and reported results on the treatment of singular potential integrals involved in the self Galerkin MoM-SIE impedance matrix entries for curved surface elements with higher order basis functions, as well as results for the accuracy and convergence properties of different methods for different locations of singular points in parametric domains, different basis functions on flat or curved surface elements, and overall.

In response to the above lacks of more adequate methods and more comprehensive studies of various methods, this paper proposes a Duffy method for singularity cancellation to evaluate singular potential integrals involved in the self Galerkin MoM-SIE impedances defined on Lagrange-type generalized curved parametric quadrilateral surface elements of arbitrary geometrical orders with polynomial basis functions of arbitrary current-approximation orders.

This paper also presents a comparison of the integration accuracy when using five different methods for evaluation of singular potential integrals, namely, (i) the singularity extraction method [5], (ii) the Duffy method for singularity cancellation (proposed in this paper), (iii) the polar transformation method for singularity cancellation [84], (iv) the quadratic rectangular transformation method for singularity cancellation [85], and (v) the cubic rectangular transformation method [86]. The study is performed for the integrals defined on a flat and a curved patch, both elements being electrically large, namely, two wavelengths in each dimension, for constant basis functions and for a choice of high-order polynomial bases, and all for five different characteristic locations of the singular point on the patch. In addition, example of full 2-D/2-D singular integral defined over highly-curved and badly-shaped patch is given.

We show that overall, of the five integration methods considered, the proposed Duffy method for singularity cancellation comes out to be the most accurate, the most rapidly converging with the increase of the order of integration formulas, and the fastest to execute.

4.2. Theory

We consider a MoM-SIE model of an antenna or scatterer built using generalized curved parametric quadrilaterals of arbitrary geometrical orders K_u and K_v (K_u, $K_v \geq 1$), shown in Fig. 4.1 and analytically described in the parametric $u-v$ domain as [10]

$$\mathbf{r}(u,v) = \sum_{i=0}^{K_u} \sum_{j=0}^{K_v} \mathbf{r}_{ij} u^i v^j \,, \quad -1 \leq u,v \leq 1 \,, \tag{4.1}$$

where $\mathbf{r}_{ij}$ are constant vector coefficients related to position vectors of interpolation nodes defining the quadrilateral. When these elements are used in conjunction with higher order polynomial basis functions, all entries of the Galerkin impedance matrix can be found as linear combinations of 2-D/2-D Galerkin integrals [10], which, for the case of testing and basis functions being defined on the same patch (self Galerkin integrals), contain the following singular inner 2-D basic potential integrals computed at an observation (testing) point (u_0, v_0) belonging to the source quadrilateral patch:

$$I_{mn} = \int_{-1}^{1}\int_{-1}^{1} u^m v^n g(R)\mathrm{d}u\mathrm{d}v \,, \quad g(R) = \frac{\mathrm{e}^{-\mathrm{j}kR}}{4\pi R} \,, \quad k = 2\pi f\sqrt{\varepsilon_0\mu_0} \,, \quad R = \left|\mathbf{r}(u,v) - \mathbf{r}(u_0,v_0)\right| \,, \tag{4.2}$$

with g being the free-space Green's function, f the operating frequency of the antenna/scatterer, and R the distance of the source point (u,v) from the point (u_0,v_0), referred to as the singular point. When the two points coincide, R is zero, and a special treatment of the singularity is needed. In what follows, we outline singularity cancellation Duffy method and overview four different methods for solving integrals in (4.2).

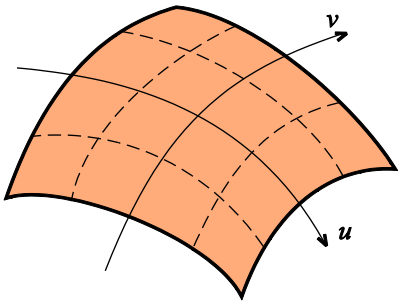

Figure 4.1. Generalized curved parametric quadrilateral defined by (4.1).

4.2.1. Duffy Method for Singularity Cancellation

Here, we propose a Duffy method to solve integrals in (4.2) defined over curvilinear, electrically large patches with higher order bases, which is based on subdividing the parametric $u-v$ square domain into four parametric triangles defined by the singular point and the vertices of the square, as shown in Fig. 4.2. Note that this is a modification in the spirit of the original Duffy method initially proposed for a 3-D domain of integration [90], which would imply a subdivision of the parametric square into eight right-angled triangles (much like in Fig. 4.4). Each triangle in Fig. 4.2, having the singular point as one of its vertices, is then independently mapped into a new $p-s$ domain as illustrated on example of first region. In [87] Duffy method is implemented for triangle local coordinates while in [88] it is further developed using mapping of curvilinear triangle to isosceles right triangle.

Mapping to the $p-s$ domain differs for different triangles in Fig. 4.2 but can be expressed in a unified way as follows:

$$a = a_0 + pc\,,\ b = b_0 + ps\,,\ 0 \le p \le 1,\ s_1 \le s \le s_2\,,\ c = \text{const}\,, \tag{4.3}$$

with coordinates a and b standing for either u or v. With this notation, Table 4.1 provides mapping parameters for each region (triangle).

Based on (4.3), the Jacobian of the mapping can be defined and computed, for every triangle, as

$$\Im = \begin{vmatrix} \dfrac{\partial a}{\partial p} & \dfrac{\partial b}{\partial p} \\ \dfrac{\partial a}{\partial s} & \dfrac{\partial b}{\partial s} \end{vmatrix} = p|c| . \tag{4.4}$$

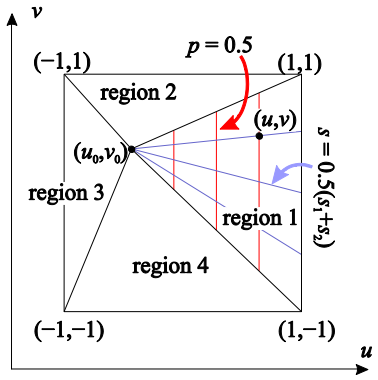

Figure 4.2. Duffy method for singularity cancellation: subdivision of the parametric $u - v$ square domain into four parametric triangles with local constant p and constant s parametric lines in triangular region 1.

TABLE 4.1

PARAMETERS OF THE DUFFY MAPPING IN (4.3) FOR THE FOUR TRIANGULAR REGIONS IN FIG. 4.2.

Region 1	Region 2	Region 3	Region 4
$u=a, v=b$	$v=a, u=b$	$u=a, v=b$	$v=a, u=b$
$s_1^1 = -1-v_0$	$s_1^2 = -1-u_0$	$s_1^3 = -1-v_0$	$s_1^4 = -1-u_0$
$s_2^1 = 1-v_0$	$s_2^2 = 1-u_0$	$s_2^3 = 1-v_0$	$s_2^4 = 1-u_0$

Combining (4.3) and (4.1), the radial distance from the singular point in triangular region l in Fig. 4.2 can be expressed as a polynomial in p with coefficients d being functions of s, as follows [note that the only term in the binomial expansion of $u^i v^j$ using (4.3) that does not contain p is $u_0^i v_0^j$]:

$$R^l = \left| \sum_{i=0}^{K_u} \sum_{j=0}^{K_v} \mathbf{r}_{ij} \left(u^i v^j - u_0^i v_0^j \right) \right| = p \left| \mathbf{d}_1^l + \sum_{i=2}^{K_u+K_v} \mathbf{d}_i^l p^{i-1} \right|, l = 1,2,3,4 . \tag{4.5}$$

Hence, the singular integral over region l can be expressed using (4.2), (4.5), and (4.4) in a way that removes (cancels) the singularity,

$$I_{mn}^l = \frac{1}{4\pi} \int_0^1 \int_{s_1^l}^{s_2^l} \frac{u^m v^n}{R^l} \mathrm{e}^{-\mathrm{j}kR^l} \Im \mathrm{d}p\mathrm{d}s = \frac{|c|}{4\pi} \int_0^1 \int_{s_1^l}^{s_2^l} \frac{u^m v^n \mathrm{e}^{-\mathrm{j}kR^l} \mathrm{d}p\mathrm{d}s}{\left| \mathbf{d}_1^l + \sum_{i=2}^{K_u+K_v} \mathbf{d}_i^l p^{i-1} \right|} , \tag{4.6}$$

namely, the singular dependence on the p coordinate in (4.5) is canceled by p in the expression for the Jacobian in (4.4), so the integral in the final form in (4.6) can be evaluated in a straightforward fashion numerically, using quadrature (e.g., Gauss-Legendre) formulas. Finally, the contributions of individual triangles are added up for the total potential integral, $I_{mn} = I_{mn}^1 + I_{mn}^2 + I_{mn}^3 + I_{mn}^4$.

4.2.2. Four Integration Methods used for Comparison

Singularity extraction method: The method of extracting the singularity consists of analytical integration of a principal singular part of the integrand over a (generally not rectangular) parallelogram whose surface is tangential to the surface of the generalized quadrilateral at the singular point, and numerical integration of the rest using Gauss-Legendre quadrature formulas [10], [5]. The parallelogram is defined by the unitary vectors [10] of the generalized quadrilateral at the singular point. The singular integral is evaluated analytically as in [77] while the other integral is well behaved in the vicinity of the point (u_0, v_0) and can be accurately integrated numerically.

Polar Transformation Method for Singularity Cancellation: Polar transformation [84] uses the same triangulation as in the Duffy method in Fig. 4.3(a) while mapping the parametric $u-v$ domain into a new $\rho-\theta$ domain, with a standard meaning of the radial coordinate, ρ, and angular coordinate, θ, in the polar coordinate system centered at the singular point, (u_0, v_0), in the $u-v$ domain.

Quadratic and Cubic Rectangular Transformation Methods for Singularity Cancellation [85], [86], subdivides the parametric $u-v$ square domain into four rectangular regions whose common vertex is the singular point. Note that the rectangular transformation for singularity cancellation in SIE integrals is applied with $t=2$ (quadratic transformation) in [85], while [86] implements the same transformation with $t=3$ (cubic transformation).

4.3. Numerical Results and Discussion

In this section, we compare the integration accuracy when using five different methods for evaluation of singular potential integrals, (i) the singularity extraction method, and four singularity cancellation methods, namely, (ii) the Duffy method, (iii) the polar transformation method, (iv) the quadratic ($t=2$) rectangular transformation method, and (v) the cubic ($t=3$) rectangular transformation method, described in the previous section. All methods are implemented for solving integrals in (4.2) defined on curved quadrilaterals described by (4.1), for several choices of the singular point.

In examples, the integrals are defined on a square plate and on a spherical patch, respectively, for two choices of basis functions, that for $m = n = 0$ and that for $m = 2$ and $n = 6$ in (4.2), and for five different locations of the singular point defined in the $u-v$ parametric domain as shown in

Fig. 4.3 and specified in Table 4.3. Example of convergence results for 2-D/2-D integral defined on highly-curved and badly-shaped geometry is also considered.

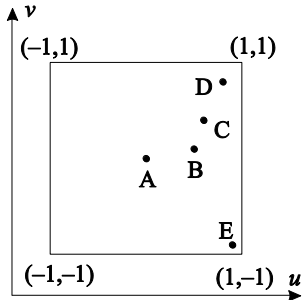

Figure. 4.3. Five different choices of the singular point (u_0, v_0), with parametric coordinates given in Table 4.3, in the $u - v$ parametric domain, over curved quadrilaterals in Fig. 4.1.

All results are given in terms of the relative integration error computed as

$$\delta = \left| I_{mn} - \tilde{I}_{mn} \right| \Big/ \left| \tilde{I}_{mn} \right| , \tag{4.7}$$

where $\tilde{I}_{mn}$ is the reference "exact" value of the integral. All computations are performed in double machine precision.

4.3.1. Integral with Constant Basis Functions over a Square Plate

As the first example, we consider the integral in (4.2) for $m = n = 0$, namely, with constant basis functions, over a square flat plate of side length $a = 2$ m, at a frequency $f = 300$ MHz, so that $a = 2\lambda$, with λ standing for the free-space wavelength. With reference to Fig. 4.4, the "exact" value $\tilde{I}_{00}$ in this special case (flat plate) can be obtained by first analytically transforming the 2-D integral in u and v as

$$\tilde{I}_{00} = \int_{-1}^{1}\int_{-1}^{1} \frac{e^{-jkR}}{4\pi R} dx dy = \sum_{l=1}^{8} \int_{0}^{\theta_l} \int_{0}^{r(\theta)} \frac{e^{-jk\rho}}{4\pi} d\rho\, d\theta = \sum_{l=1}^{8} \int_{0}^{\theta_l} \frac{e^{-\frac{jkd_l}{\cos\theta}}}{4\pi} d\theta , \tag{4.8}$$

and then numerically solving the final non-singular 1-D integrals in θ. This example's $\tilde{I}_{00}$ integral values are given in Table 4.2. Fig. 4.5 shows the error in (4.7) against the orders of Gauss-Legendre integration formulas, i.e., numbers of integration points, in each of the region's local directions, *NGL* (the same in both directions), for five different singular points in Fig. 4.3 and five different integration methods.

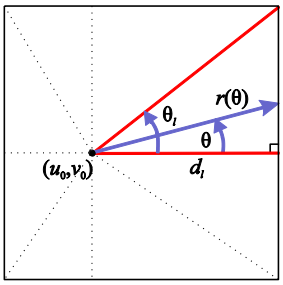

Figure 4.4. For integration in (4.8) over one of the eight right-angled triangles constituting a square flat plate, to compute the reference "exact" value of the integral I_{00}

TABLE 4.2

EXACT INTEGRAL VALUE $\tilde{I}_{00}$ OVER FLAT PLATE OF SIZE 2λ FOR SINGULAR POINTS GIVEN IN FIG. 4.3.

Point A	0.0390728194148081 - 0.0338074127356726i
Point B	- 0.0104077559218362 - 0.0873743257011760i
Point C	- 0.019482990210943 - 0.117888060820110i

Based on Figs. 4.5(a)-(c), we conclude that, for singular points A, B, and C, the Duffy method and the polar transformation method for singularity cancellation perform the best, with the Duffy method converging even faster in some cases than the latter method. We also observe that, accuracy and convergence properties of the singularity extraction method noticeably outperform the cubic rectangular transformation method, and especially the quadratic rectangular transformation method. From Figs. 4.5(d)-(f), we realize that the Duffy method is considerably more accurate and faster converging than the polar transformation method for some specific

choices of singular points, i.e., points D and E, and that the singularity extraction method features the highest convergence rate of all the methods for smaller values of *NGL*.

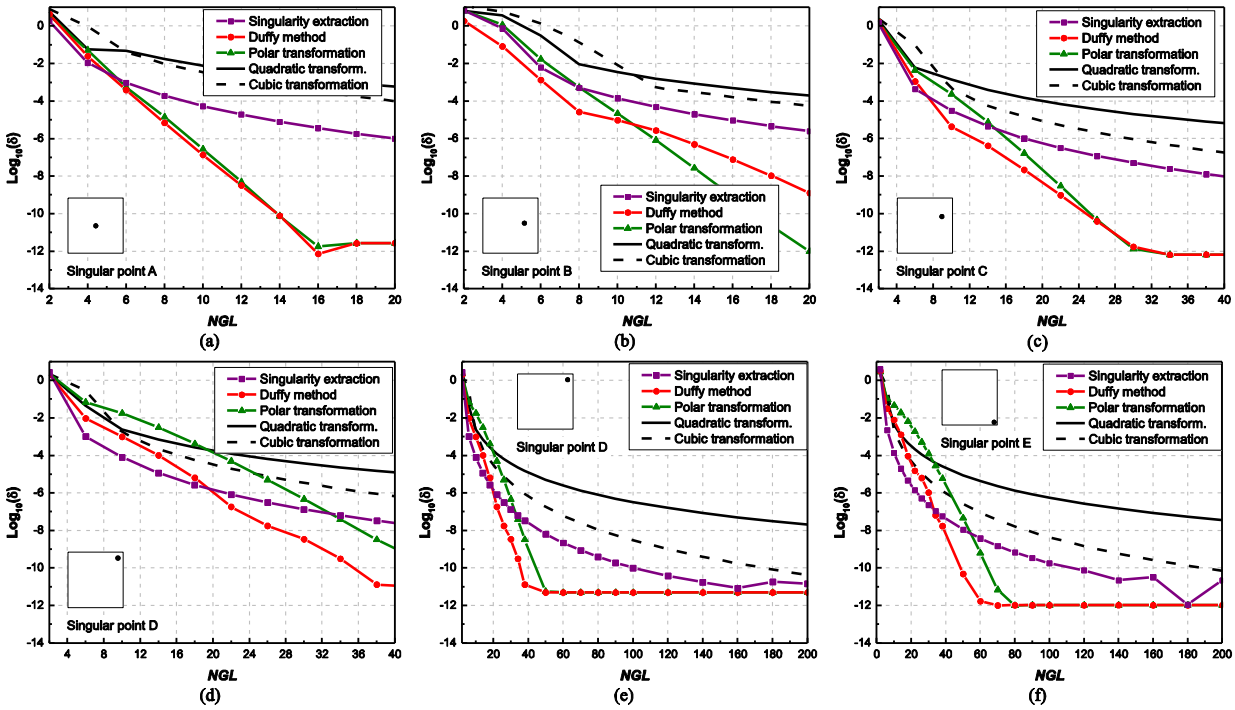

Figure 4.5. Evaluation of the integral I_{00} (for $m = n = 0$) in (4.2) over a square flat plate using the singularity extraction method, the Duffy method for singularity cancellation, the polar transformation method for singularity cancellation, the quadratic rectangular transformation method for singularity cancellation, and the cubic rectangular transformation method: integration error in (4.7) against the order of Gauss-Legendre integration formulas, *NGL*, for five different singular points in Fig. 4.3 [$\tilde{I}_{00}$ is computed as given in (4.8) and Fig. 4.4].

Note, however, that this is electrically a rather large patch, namely, the 2λ×2λ plate considered as a single MoM element, and that smaller patches, e.g., those on the order of λ×λ and 0.5λ×0.5λ, also used in higher order MoM-SIE techniques, and especially electrically small patches measuring 0.1λ×0.1λ and less, characteristic for low-order MoM-SIE techniques, require far lower values of *NGL* for a given accuracy of integration and a given machine precision (double precision).

Overall, when *NGL* is not limited, as shown in Figs. 4.5(e)-(f), the best convergence behavior is achieved by the Duffy method. While for some singular points and lower values of *NGL*, the

singularity extraction method reaches certain accuracy levels the fastest, further improvement of its accuracy at the expense of adopting higher *NGL* values is rather slow. On the other hand, both the Duffy method and the polar transformation method exhibit a logarithmic-type of convergence with increasing *NGL*.

Among the results for all singular points, the worst accuracies and convergence behaviors for all integration methods are those in Fig. 4.5(f). The singular point E in Fig. 4.3 thus comes out to be the worst-case scenario for the evaluation of the integral I_{00} using any of the methods, and the error graphs in Figs. 4.5(e) and (f) may be considered as defining and limiting the accuracy and convergence properties of the individual methods as long as the integration performance at specific singular points is concerned.

Table 4.4 provides information on computation times for the five integration methods, for singular point A and *NGL* = 20. We see that, out of all the methods, the Duffy method is the fastest to execute.

TABLE 4.3

PARAMETRIC COORDINATES OF SINGULAR POINTS IN FIG. 4.3.

Point A	Point B	Point C	Point D	Point E
$u_0 = 0$	$u_0 = 0.5$	$u_0 = 0.6$	$u_0 = 0.8$	$u_0 = 0.9$
$v_0 = 0$	$v_0 = 0.1$	$v_0 = 0.4$	$v_0 = 0.8$	$v_0 = -0.9$

4.3.2. Integral with High-Order Basis Functions and Geometry

In the second example, we evaluate the integral in (4.2) for a selection of high-order basis functions given by $m = 2$ and $n = 6$ over a curved quadrilateral patch (in Fig. 4.1) of the fourth geometrical order, namely, with $K_u = K_v = 4$ in (4.1), modeling one-sixth of a sphere of radius

a = 1.2732 m, at a frequency f = 300 MHz, with the patch being about 2λ across. Shown in Fig. 4.6 is the geometry of the patch and the error in (4.7) against the order of Gauss-Legendre integration formulas, *NGL*, for singular points A, B, C, D, and E in Fig. 4.3 and the five different integration methods. Based on the results in the previous example, as well as on extensive numerical investigations of the five methods in this (second) example, it is established that both the Duffy method and the polar transformation method for singularity cancellation with the order of Gauss-Legendre integration formulas adopted to be as high as $NGL = 200$ can reliably be considered as the fully converged and highly accurate, with negligible differences between results of the two method (for all five singular points analyzed, the relative difference between results obtained using Duffy and polar transformation methods with $NGL = 200$ is less than 1.5×10^{-14}). Therefore, we choose the solution by the Duffy method with $NGL = 200$ as the reference ("exact") result for $\tilde{I}_{26}$ in (4.7) in this example.

Conclusions about the accuracy and convergence properties of different integration methods, and their relative advantages and shortcomings, for different singular points and overall, are similar to those drawn in the previous example. In addition, we realize that all the methods perform well in Fig. 4.6(a) since singular point location A yield non-singular integral in (4.2), due to the polynomial part of the integrand having higher-order zeros. Figs. 4.6(b)-(f) demonstrate that the polar transformation method offers substantially slower convergence for singular integrals defined over curved patch when compared to ones defined on the flat geometry.

Further, for low orders of integration formulas, five methods result in a comparable precision; however, with the increase in number of integration points, Duffy and polar transformation methods yield a convergence superior to other methods.

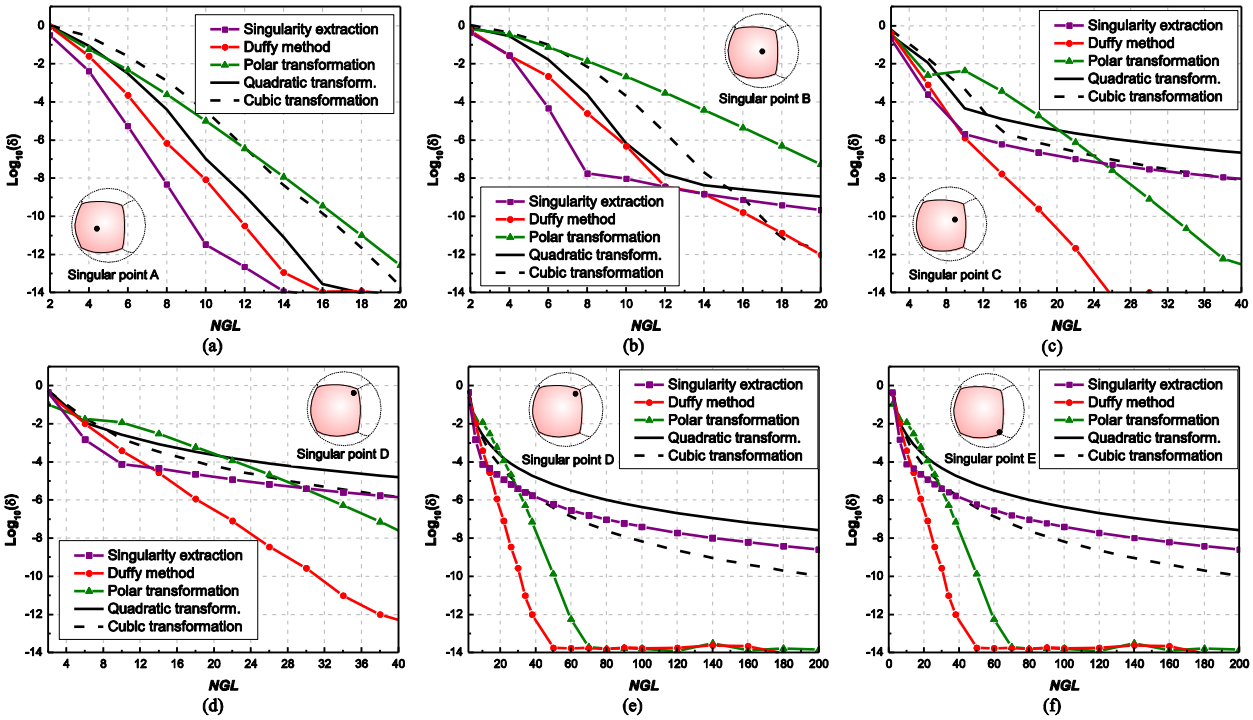

Figure 4.6. Evaluation of the integral I_{26} (for $m = 2$ and $n = 6$) in (4.2) over a spherical patch using five different integration methods: integration error in (4.7) against the order of integration formulas, *NGL*, for five different singular points ($\tilde{I}_{26}$ is computed by the Duffy method with *NGL* = 200).

4.3.3. Example of 2-D/2-D Integral

In addition, in similar fashion as in previous example, we evaluate full 2-D/2-D integral, used to assembly Galerkin impedance matrix element, defined on the highly-curved and badly-shaped patch ($K_u = K_v = 4$) modeling half of the oblate spheroid of maximal dimension 2λ with order of testing and basis polynomials being $m_t = n_t = 4$ and $m_b = n_b = 6$, respectively. Based on conclusions given in [92] we adopted *NGL* = 6 for calculation of outer, well-behaved integral while *NGL* for inner 2-D integration was ranged as depicted in Fig. 4.7. Patch geometry and convergence results of integral I_{4466} are given in the Fig. 4.7 while conclusions drawn stay the same as in previous examples. Note that accuracy of 10^{-3} and 10^{-4} that can be considered as optimal in higher-order SIE modeling is first reached by the Duffy method.

TABLE 4.4

COMPUTATION TIMES FOR FIVE INTEGRATION METHODS (INTEGRAL I_{00} OVER A SQUARE FLAT PLATE, SINGULAR POINT A, AND $NGL = 20$).

Singularity extraction	Duffy method	Polar transform.	Quadratic transform.	Cubic transform.
390 μs	328 μs	359 μs	390 μs	374 μs

4.4. Conclusions

This paper has proposed a Duffy method for singularity cancellation to evaluate singular potential integrals involved in the self Galerkin impedances defined on Lagrange-type generalized curved parametric quadrilateral surface elements of arbitrary geometrical orders with polynomial basis functions of arbitrary current-approximation orders in MoM-SIE analysis of antennas and scatterers. In addition to providing a new singularity cancellation method for the considered MoM-SIE elements and basis functions, the paper is considered as a step forward in overcoming the current lack of evaluations of various possible singularity treatment and integration methods, and assessments of the accuracy and convergence properties of different methods, and their relative advantages and shortcomings, for different locations of singular points in parametric domains, different basis functions on flat or curved surface elements, and overall.

A final overall conclusion based on evaluations of singular potential integrals in several examples, is that, of the five integration methods considered, the Duffy method for singularity cancellation comes out to be the most accurate, the most rapidly converging with the increase of the orders of Gauss-Legendre integration formulas, and the fastest to execute.

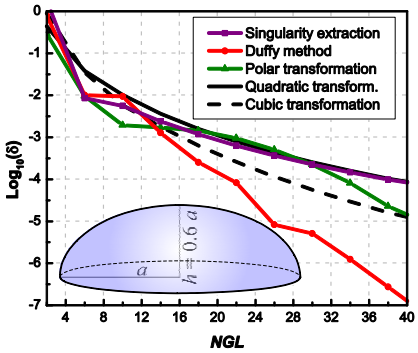

Figure 4.7. 2-D/2-D I_{4466} integral over badly–shaped and highly–curved patch.

5. NUMERICAL COMPUTATION OF NEAR-SINGULAR AND NEAR-HYPERSINGULAR INTEGRALS IN HIGHER ORDER METHOD OF MOMENTS USING CURVED QUADRILATERAL PATCHES

5.1. Introduction

In numerical techniques based on the method of moments (MoM) in the surface integral equation (SIE) formulation in the frequency domain, special attention must be paid to achieving high accuracy, which includes advanced methods for numerical computation of singular and near-singular integrals defined on MoM-SIE patches. The techniques for dealing with such integrals, which arise for zero or small source-to-field distances in computing the MoM matrix entries, can broadly be classified into singularity extraction or subtraction methods and singularity cancellation or coordinate transformation methods. Also, when a MoM-SIE method is aimed at analysis of both metallic and dielectric/magnetic structures, such generality in electromagnetic MoM-SIE simulations increases the singularity of the integral kernel, and requires special treatment of highly singular integrals. Finally, this problem is even more pronounced when higher order basis functions are used for the approximation of electric and magnetic equivalent surface currents in the MoM-SIE method and when such functions are defined on curved patches.

This paper presents a novel method for numerical computation of near-singular (potential) and near-hypersingular (field) integrals defined on Lagrange-type generalized curved parametric quadrilateral MoM-SIE surface elements of arbitrary geometrical orders with polynomial basis functions of arbitrary current-approximation orders. The integrals are evaluated using a method based on the singularity extraction, which consists of analytical integration of a principal singular

part of the integrand over a (generally not rectangular) parallelogram whose surface is close to the surface of the generalized quadrilateral near the singular point and numerical integration of the rest using Gauss-Legendre quadrature formulas.

The majority of the existing extraction techniques, used in MoM-SIE modeling so far, have been developed for planar triangular patches involving low-order basis functions. Few of those have been extended to curved patches but without really taking into account the curvature of the surface. The presented integration technique considers the curvature of the patch by extracting multiple terms in the evaluation of the principal singular part. Further, the theory behind the extraction technique has been extended to consider integrals with higher order basis functions.

Numerical examples demonstrate fast convergence of the novel integration method with increasing the orders of Gauss-Legendre integration formulas, i.e., numbers of integration points, over quadrilateral patches, in a variety of cases. Integrals are calculated over curved patches with curvature ranging from flat or almost flat patches to those with very pronounced curvature, such as spherical patches. Examples show steady behavior of the integration method for arbitrary choice of the location as well as the distance of the near-singular point. Further, examples investigate the numerical behavior of integrals with different choices of basis functions varied from constant approximations to very-high-order polynomial bases, and for elements with sizes varied from electrically very small to electrically large quadrilaterals extending to a couple of wavelengths in each dimension.

This paper is organized as follows. Section 5.2 gives an overview of the novel singularity extraction. In Section 5.3 numerical results and discussion are provided, followed by the conclusions in Section 5.4.

5.2. Double higher order singularity extraction

5.2.1. Near-Singular and Near-Hyper-Singular Integrals

We consider a MoM-SIE model of an antenna or scatterer built using generalized curved parametric quadrilaterals of arbitrary geometrical orders K_u and K_v (K_u, $K_v \geq 1$), shown in Fig. 5.1 and analytically described in the parametric $u-v$ domain as [10].

$$\mathbf{r}(u,v)=\sum_{k=0}^{K_u}\sum_{l=0}^{K_v}\mathbf{r}_{kl}u^k v^l\ ,\ -1\leq u,v\leq 1, \tag{5.1}$$

where $\mathbf{r}_{kl}$ are constant vector coefficients related to position vectors of interpolation nodes defining the quadrilateral. When these elements are used in conjunction with higher order polynomial basis functions, all entries of the Galerkin impedance matrix can be found as linear combinations of 2-D/2-D Galerkin integrals [10]. In a general case, these contain the following singular inner 2-D basic potential integrals computed at an observation (testing) point , that is close to the source quadrilateral patch:

$$I1_{ij}=\int_{-1}^{1}\int_{-1}^{1}\frac{u^i v^j e^{-\mathrm{j}\beta R}}{4\pi R}\mathrm{d}u\mathrm{d}v\,,\qquad I2_{ij}=\int_{-1}^{1}\int_{-1}^{1}u^i v^j\,\frac{(1+\mathrm{j}\beta R)e^{-\mathrm{j}\beta R}}{4\pi R^3}\mathrm{d}u\mathrm{d}v\,,$$

$$\beta=2\pi f\sqrt{\varepsilon_0\mu_0}\,,\quad R=\left|\mathbf{r}(u,v)-\mathbf{r}(u_0,v_0)-d\mathbf{n}\right|, \tag{5.2}$$

with f being the operating frequency of the antenna/scatterer, and R the distance of the source point (u,v) from the field point, referred to as the near-singular point. $\mathbf{r}(u_0,v_0)$ is the position vector of the so called close point projection (cpp) from the field point onto the quadrilateral of interest, and d_0 is the distance of the field point from its projection, while **n** is the unit normal to the quadrilateral surface. When the two points are close, R becomes small, and a special treatment of the near-singularity is needed.

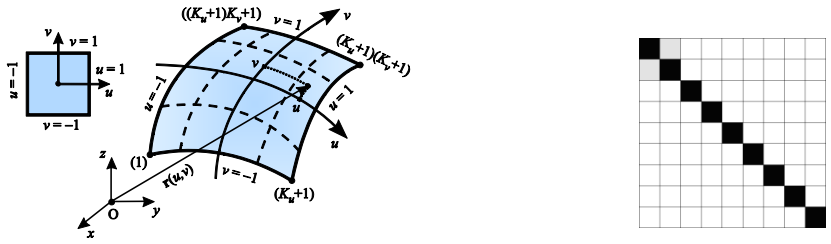

(a) (b)

Figure 5.1. a) Generalized curved parametric quadrilateral patch for double-higher-order MoM-SIE modeling. (b) Sketch of the orthogonality factor for maximally orthogonalized hierarchical basis functions of the eight order.

The traditional singularity extraction method consists of extracting the singularity of analytical integration of a principal singular part of the integrand over a (generally not rectangular) parallelogram, whose surface is tangential to the surface of the generalized quadrilateral at the singular point, and numerical integration of the rest using Gauss-Legendre quadrature formulas [10], [5]. The parallelogram is defined by the unitary vectors [10] of the generalized quadrilateral at the cpp point. The near-singular integral is evaluated analytically as in [93] while the other integral is well behaved in the vicinity of the point and can be accurately integrated numerically.

The vector **R**, which describes the distance between the source and test points, can be written as:

$$\mathbf{R}(u_0+du, v_0+dv) = -d_0\mathbf{n} + \sum_{\substack{k=0 \\ k+l\geq 1}}^{K_u}\sum_{l=0}^{K_v} \mathbf{a}_{kl} du^k dv^l . \tag{5.3}$$

The notation $\mathbf{a}_{kl}$ is used to represent the k^{th} and l^{th} derivative of **r** with respect to u and v, evaluated at the point (u_0, v_0), close point projection of the near-singular point onto the curvilinear surface. We consider that, by the definition of the cpp point, $\mathbf{n} = \mathbf{a}_{10}\times\mathbf{a}_{01}/|\,\mathbf{a}_{10}\times\mathbf{a}_{01}|$ at (u_0, v_0), then the expansion of R^2 can be rewritten as:

$$R^2 = d_0^2 + b_u^2 du^2 + b_v^2 dv^2 + 2b_u b_v \cos\alpha du dv + t, \tag{5.4}$$

where b_u, b_v and cosα are defined by : $b_u^2 = \mathbf{a}_{10} \cdot \mathbf{a}_{10} - 2d_0 \mathbf{a}_{20} \cdot \mathbf{n}$, $b_v^2 = \mathbf{a}_{01} \cdot \mathbf{a}_{01} - 2d_0 \mathbf{a}_{02} \cdot \mathbf{n}$ and $\cos\alpha = \left(\mathbf{a}_{10} \cdot \mathbf{a}_{01} - 2d_0 \mathbf{a}_{11} \cdot \mathbf{n}\right) / b_u b_v$, while d_0 is the distance of near-singular point to its projection. Furthermore, it is worth noting that t is a polynomial of du and dv with all terms being of at least the third order.

Novel higher order extraction introduces a new type of parallelogram tangential to the quadrilateral at (u_0, v_0), so that R_P, the distance between any parallelogram point from the near-singular is $R_P^2 = d_0^2 + b_u^2 du^2 + b_v^2 dv^2 + 2b_u b_v \cos\alpha du dv$, i.e. $R^2 = R_P^2 + t$. Consequently, the parallelogram used for extraction of the integrand singularities is tangential to the quadrilateral at the cpp point and has sides of the length b_u and b_v with an α angle between them.

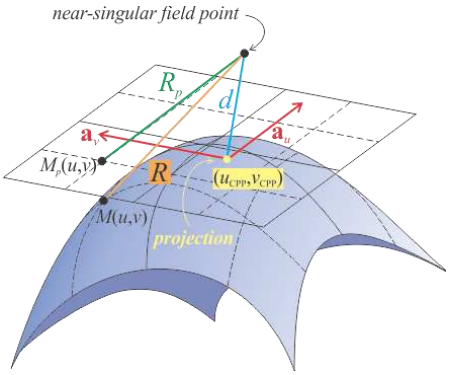

Figure 5.2. Illustration of the singularity extraction method based on the analytical integration over parallelogram tangential to the quadrilateral at the close point projection.

In order to account for the curvature of the quadrilateral, the discrepancy between distances from curvilinear patch and the flat parallelogram can be expanded as:

$$R - R_P = R_P\left(\left(1+\frac{t}{R_P^2}\right)^{1/2} - 1\right) \approx R_P\left(\frac{1}{2}\frac{t}{R_P^2} - \frac{1}{8}\left(\frac{t}{R_P^2}\right)^2 \ldots\right). \tag{5.5}$$

Following the same idea, the expansion of the integrands that considers higher order terms is done as follows,

$$\frac{e^{-\mathrm{j}\beta R}}{R} = \sum_{i=1}^{\infty} \frac{C_i(du,dv)}{R_P^{2i-1}},\ (1+\mathrm{j}\beta R)\frac{e^{-\mathrm{j}\beta R}}{R^3} = \sum_{i=1}^{\infty} \frac{D_i(du,dv)}{R_P^{2i-1}}, \tag{5.6}$$

with *C* and *D* being polynomials of *du* and *dv*. In the same fashion as in (5.5), it is easily shown that expansions in (5.6) consist exclusively of odd terms of R_P.

Finally, integrals given in (5.2) are calculated by applying the numerical integration to the smooth integrand obtained by subtracting the truncated expansions given in (5.6) from the original integrand. Integration of the higher-order integrals over the parallelogram is performed analytically.

5.2.2. Analytical integrals over parallelogram

Analytical closed form formulas for computing the integrals involving higher order basis functions and R_P^n ($n \geq -3$) singularities, over flat surfaces are first developed in [93]. Here, these formulas are extended to consider integrals of this type for any odd *n*. For the simplicity of this formulation, close projection point (*u*0, *v*0) is assumed to be (0,0), without any loss of generality for the formulas developed here.

First, a local orthogonal *xy* coordinate system is introduced as given in Fig. 5.3. Next, the local *u* and *v* coordinates, as well as their corresponding unit vectors, are represented as:

$$u = \frac{(x - \mathrm{ctg}\alpha y)}{b_u},\ v = \frac{y}{b_v \sin\alpha},\ \hat{u} = \hat{x},\ \ \hat{v} = \hat{x}\cos\alpha + \hat{y}\sin\alpha. \tag{5.7}$$

Furthermore, in the same fashion as in [93], polar coordinates are defined by $\vec{\rho} = b_u u\hat{u} + b_v v\hat{v}$, while local coordinates can be defined via the scalar product of vectors as:

$$u = \frac{1}{b_u}\vec{\rho}\left(\hat{x} - ctg(\alpha)\hat{y}\right),\ v = \frac{\vec{\rho}\hat{y}}{b_v \sin\alpha}. \tag{5.8}$$

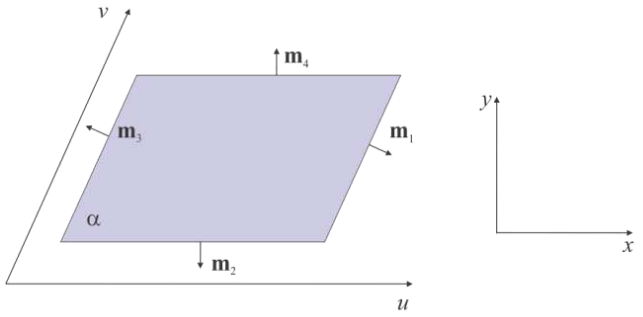

Figure 5.3. Parallelogram in the local nonorthogonal uv coordinate system and its corresponding orthogonal local *xy* coordinate system.

Finally, the surface gradient is defined as $\nabla_s\left(R_P^{n+2}\right) = (n+2)R_P^n\vec{\rho}$ for any odd *n*. The last equation is used together with (5.8) to rewrite the integrals over the parallelogram:

$$\begin{aligned}
&\int_s R_P^n u^p v^q dS = \frac{\left(\hat{x} - \mathrm{ctg}\alpha\hat{y}\right)}{b_u}\int_s R_P^n \vec{\rho} u^{p-1} v^q dS \\
&= \frac{\left(\hat{x} - \mathrm{ctg}\alpha\hat{y}\right)}{b_u(n+2)}\int_s \nabla_s\left(R_P^{n+2}\right) u^{p-1} v^q dS \\
&= \frac{\left(\hat{x} - \mathrm{ctg}\alpha\hat{y}\right)}{b_u(n+2)}\int_s \left[\nabla_s\left(R_P^{n+2} u^{p-1} v^q\right) - R_P^{n+2}\nabla_s\left(u^{p-1} v^q\right)\right] dS.
\end{aligned} \tag{5.9}$$

The last equation in (5.9) is obtained by applying the gradient product rule. In addition, the gradient of the simple polynomial functions in the local coordinate system can be expressed as:

$$\nabla_s\left(u^p v^q\right) = \frac{pu^{p-1}v^q}{b_u}\hat{x} - \mathrm{ctg}\alpha\frac{pu^{p-1}v^q}{b_u}\hat{y} + \frac{qu^p v^{q-1}}{b_v \sin\alpha}\hat{y}. \tag{5.10}$$

So, if $I_s^{n,p,q} = \int_s u^p v^q R_P^n dS$ a surface integral across the parallelogram and, $I_{i,line}^{n,p,q} = \int_{line\,i} u^p v^q R_P^n dl$ is a line integral along the i^{th} parallelogram side (as labeled in Fig. 5.3), then formulas may be obtained via the divergence theorem from (5.9) as:

$$I_s^{n,p,q} = \frac{1}{n+2}\left[-(p-1)A_u I_s^{n+2,p-2,q} + qB_u I_s^{n+2,p-1,q-1} + \sum_{i=1}^{4} \vec{T}_u \cdot \vec{m}_i I_{i,line}^{n+2,p-1,q}\right] \tag{5.11}$$

$$I_s^{n,p,q} = \frac{1}{n+2}\left[-(q-1)A_v I_s^{n+2,p,q-2} + pB_v I_s^{n+2,p-1,q-1} + \sum_{i=1}^{4} \vec{T}_v \cdot \vec{m}_i I_{i,line}^{n+2,p,q-1}\right] \tag{5.12}$$

with the corresponding coefficients being $A_u = \frac{1}{(b_u \sin\alpha)^2}$, $A_v = \frac{1}{(b_v \sin\alpha)^2}$, $B_u = B_v = \frac{\text{ctg}\alpha}{b_u b_v \sin\alpha}$, $\vec{T}_u = \frac{1}{a_u}(\hat{x} - ctg(\alpha)\hat{y})$ and $\vec{T}_v = \frac{\hat{y}}{a_v \sin\alpha}$.

Formulas given in (5.11) and (5.12) can be used in the recursive fashion to calculate analytical solution for any $I_s^{n,p,q}$ integral. The traversing through recursive formula is applied until $I_s^{n,0,0}, I_s^{n,1,0}, I_s^{n,0,1}, I_s^{n,1,1}$ are reached. Note that recursion in *n* is done in steps of two, so all remaining terms have *n* odd. Once all terms can be described by (*p*, *q*) $\in$ {(0, 0), (0, 1), (1, 0), (1, 1)}, special (*p*, *q*) independent recursive formulas are developed leading to the final solution, which depends only on integrals with known analytical solutions: $I_s^{-1,0,0}, I_s^{-1,1,0}, I_s^{-1,0,1}, I_s^{-3,0,0}, I_s^{-3,1,0}, I_s^{-3,0,1}$. By following the procedure described in [93], recursive formulas for line integrals are developed in the same fashion.

The main difference between the work presented here and work done by Prof. Oijala in [93], is the extension of these formulas to any odd integer *n*. Originally, work in [93] was developed

for higher order basis functions over flat triangles with no need to calculate integrals with $n < -3$. However, the developed scheme was not applicable to curvilinear patches. Future development of this novel extraction scheme consists of its application to full 4D integrals arising in computation of the impedance matrix elements from the MoM solution of various integral equation formulations which are used in the electromagnetic analysis of metallic, dielectric and composite structures.

5.3. Numerical Results

In this section, the integration accuracy using the new singularity extraction method is evaluated. All methods are implemented for solving integrals in (5.2) defined on curved quadrilaterals described by (5.1), for arbitrary choice of the near-singular point.

All results are given in terms of the relative integration error computed as

$$\delta = \log_{10} \left| I_{mn} - \tilde{I}_{mn} \right| \Big/ \left| \tilde{I}_{mn} \right| , \tag{5.13}$$

where $\tilde{I}_{mn}$ is the reference "exact" value of the integral. All computations are performed in double floating-point precision. Note that the novel extraction method performs numerical integration over the entire *uv* domain without subdividing it into four square or triangular subdomains, having close point projection point as the new vertex. The described subdivision is characteristic of the majority of extraction or cancellation schemes, which overall would introduce four times more integration points. The described subdivision is very inefficient, especially when projection is close to the domain edge, which, in the Galerkin type of testing, describes the majority of numerical cases of near-singular integrals.

Furthermore, local coordinates of the close point projection used in numerical examples are chosen to show convergence of the method for cases where projection is very close to the edge

of the integration domain, i.e. cases where other integration methods exhibit very low accuracy and, in some cases, even divergence.

5.3.1. Near-Singular and Near-Hypersingular Integrals over Curvilinear Spherical patch

In the first set of numerical results, we evaluate the integrals in (5.2) for a selection of both low-order and high-order basis functions given by $(p,\ q) = (\ 0,\ 0)$ and $(p,\ q) = (\ 6,\ 6)$, respectively, over a curved quadrilateral patch (in Fig. 5.1a) of second geometrical order, i.e. $K_u = K_v = 2$ in (5.1), modeling one-sixth of a sphere of radius $a = 1$ m, at a frequency $\beta = 2$ rad/m and distance $d_0 = 0.001$m, while close point projection is performed at local coordinates $(u_0, v_0) = (\ 0.9,\ 0.9)$. The integrals are calculated using novel double higher order singularity extraction with the expansion in (5.6) truncated at $i = 5$ and full expansion of C and D coefficients (5.6). Figs. 5.4a and 5.4b show excellent convergence of near singular and near hypersingular integrals, respectively, for $(p, q) = (\ 0,\ 0)$ with the increase of number of Gauss-Legendre points. In addition, Figs. 5.4c and 5.4d show the same type of results for $(p, q) = (\ 6,\ 6)$ integrals.

In order to show robustness of the method, for the same choice of the close point projection, distance d_0 is ranged from 10^{-12} m to 10^{-2} m, covering the full range of near-singular/hypersingular points (near-singular/hypersingular behavior). Figures 5.5a-5.5d correspond to the cases analyzed in the Figs 5.4a to 5.4d, respectively, and show great robustness and accuracy of the method for a number of Gauss-Legendre integration points being NGL=8.

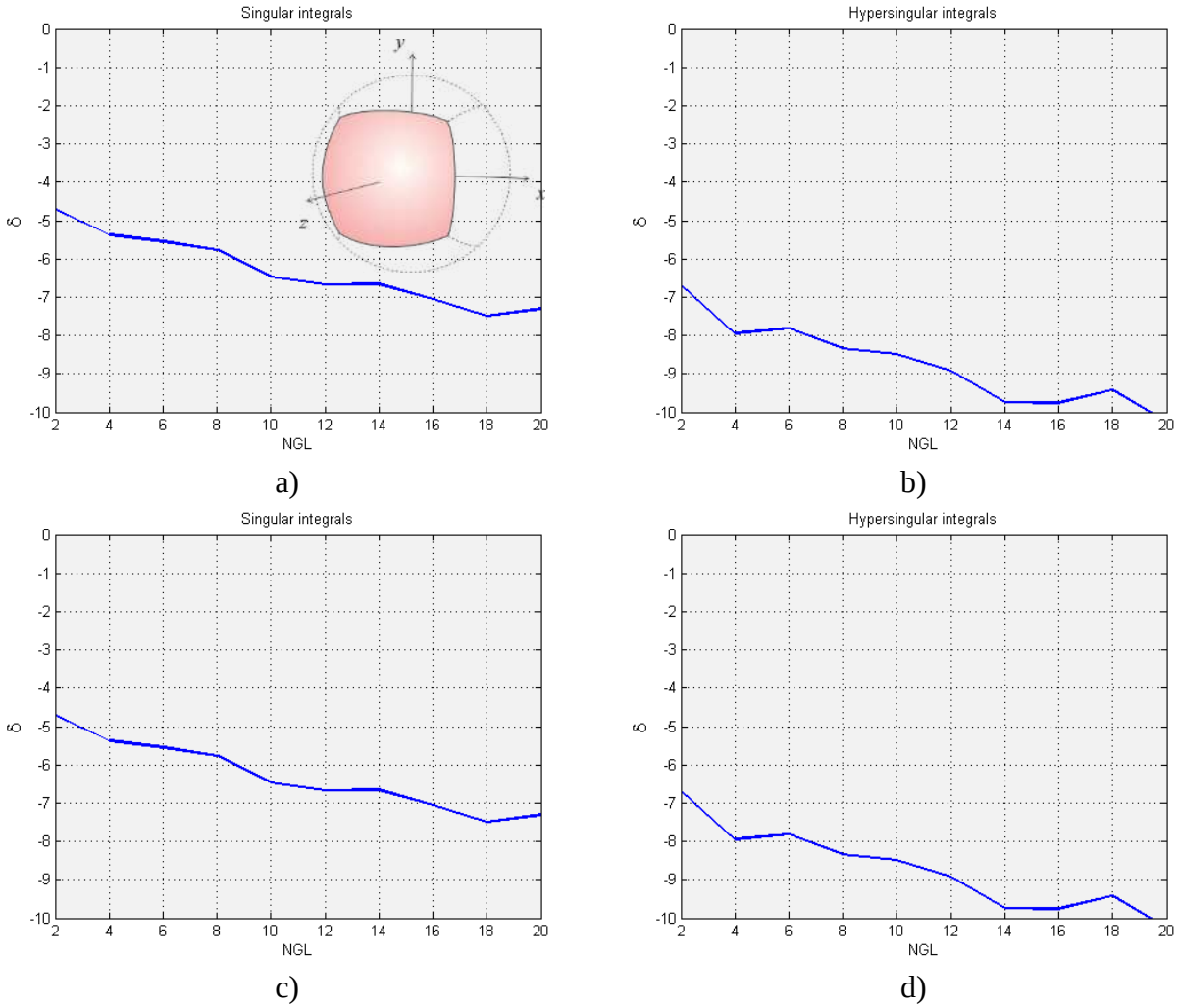

Figure 5.4. Convergence of the novel higher order singularity extraction with the increase of *NGL* points on the second order spherical patch, modeling one sixth of the sphere, with cpp local coordinates (u_0, v_0) = (0.9, 0.9) and d_0 = 0.001m: a) (p, q) = (0, 0), singular integrals, b) (p, q) = (0, 0), hypersingular integrals, c) (p, q) = (6, 6), singular integrals, d) (p, q) = (6, 6), hypersingular integrals.

5.4. Near-Singular and Near-Hypersingular Integrals calculated using optimized expansion of power series

Further, on a new set of results, expansion used in higher order singularity extraction (5.6) is again truncated at i = 5 while optimal choice of C and D coefficients contains only the highest order term in the expansion.

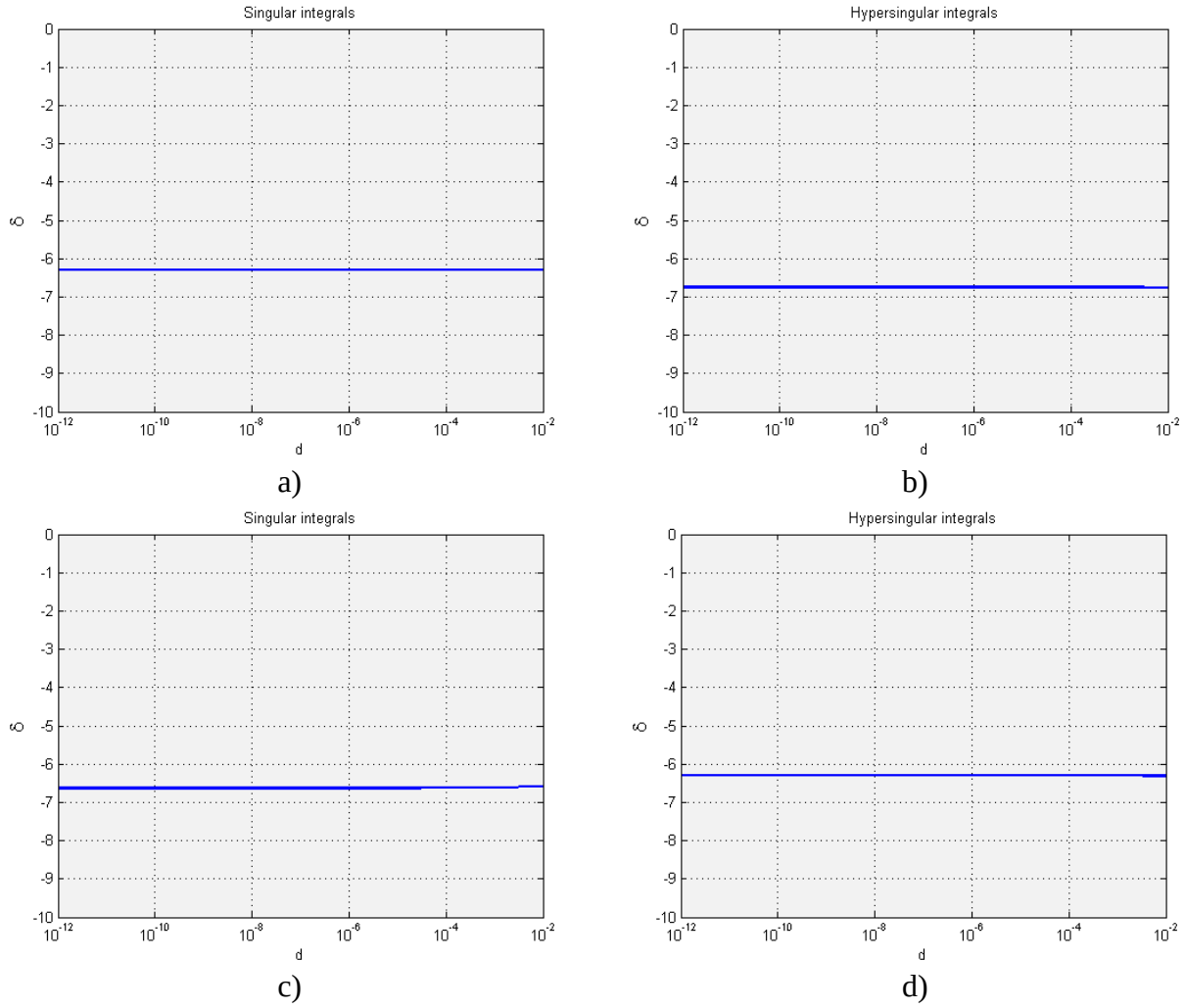

Figure 5.5. Accuracy of the novel higher order singularity extraction over the full range of nearsingular distances on the second order spherical patch, modeling one sixth of the sphere, with cpp local coordinates (u_0, v_0) = (0.9, 0.9) and NGL=8 a) (p, q) = (0, 0), singular integrals, b) (p, q) = (0, 0), hypersingular integrals, c) (p, q) = (6, 6), singular integrals, d) (p, q) = (6, 6), hypersingular integrals.

Figs. 5.6a and 5.6b show convergence of singular and hypersingular integrals, respectively, for a higher order polynomial choice (p, q) = (6, 6) on the spherical patch described in the previous example, at a frequency β = 2 rad/m and distance d_0 = 0.0001m, while close point projection is at local coordinates (u_0, v_0) = (0.99, 0.99). In addition, Fig. 5.6c and 5.6d show excellent convergence of singular and hypersingular integrals, respectively, for the same choice of distances and close point projection coordinates on a non-planar, distorted bilinear patch.

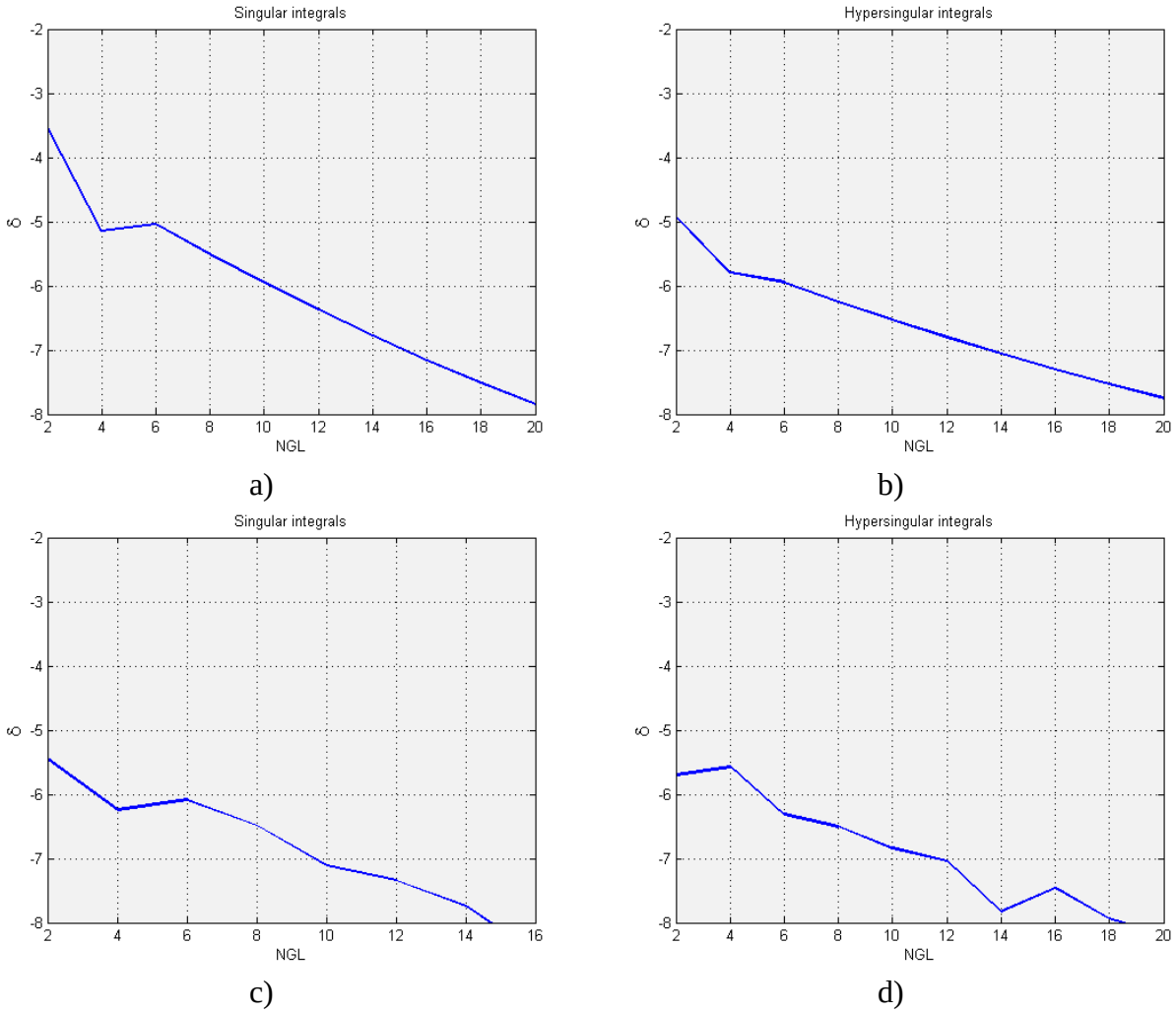

Figure 5.6. Convergence of the novel higher order singularity extraction calculated using optimized expansion of power series, with cpp local coordinates (u_0, v_0) = (0.99, 0.99), d_0 = 0.0001m and (p, q) = (6, 6), over a) spherical patch, singular integrals, b) spherical patch, hypersingular integrals, c) bilinear patch, singular integrals, d) bilinear patch, hypersingular integrals.

5.5. Conclusions

A novel method for numerical computation of near-singular (potential) and near-hypersingular (field) integrals defined on Lagrange-type generalized curved parametric quadrilateral MoM-SIE surface elements of arbitrary geometrical orders with polynomial basis functions of arbitrary current-approximation orders was presented. The integrals are evaluated

using a method based on the singularity extraction, which consists of analytical integration of a principal singular part of the integrand over a parallelogram whose surface is close to the surface of the generalized quadrilateral near the singular point and numerical integration of the rest using Gauss-Legendre quadrature formulas. The parallelogram used in the new technique is constructed in order to approximate geometry of the curved quadrilateral more accurately than the parallelogram used in the traditional singularity extraction. Further, curvature of the quadrilateral was approximated by introducing higher order terms in the integral expansion. In addition, special analytical formulas were developed to solve for higher order integrals over planar surfaces. Finally, the method was optimized and tested on a special set of numerical experiments chosen because they exhibited very low accuracy (and in some cases even diverged) when analysed by other integration methods. The overall conclusion is that the new integration method is very robust and performs extremely well in all tested examples.

4 REFERENCES

[1] J. M. Jin, "The Finite Element Method in Electromagnetics", 2nd ed., *John Wiley & Sons*, New York, 2002.

[2] J. M. Jin and D. J. Riley, "Finite Element Analysis of Antennas and Arrays", *John Wiley & Sons*, New York, 2008.

[3] P. P. Silvester and R. L. Ferrari, "Finite Elements for Electrical Engineers", 3rd ed., *Cambridge University Press*, 1996.

[4] J. L. Volakis, A. Chatterjee, and L. C. Kempel, "Finite Element Method for Electromagnetics", *IEEE Press*, New York, 1998.

[5] B. M. Notaroš, "Higher order frequency-domain computational electromagnetics," Special Issue on Large and Multiscale Computational Electromagnetics, *IEEE Transactions on Antennas and Propagation*, Vol. 56, No. 8, pp. 2251-2276, August 2008.

[6] M. M. Ilic and B. M. Notaros, "Higher order hierarchical curved hexahedral vector finite elements for electromagnetic modeling," *IEEE Transactions on Microwave Theory and Techniques*, Vol.51, (3), pp.1026-1033, March 2003.

[7] M. M. Ilic, A. Z. Ilic, and B. M. Notaros, "Higher Order Large-Domain FEM Modeling of 3-D Multiport Waveguide Structures with Arbitrary Discontinuities," *IEEE Transactions on Microwave Theory and Techniques*, Vol. 52, No. 6, pp.1608-1614, June 2004.

[8] M. M. Ilić, M. Djordjević, A. Ž. Ilić, and B. M. Notaroš, "Higher order hybrid FEM-MoM technique for analysis of antennas and scatterers," *IEEE Trans. Antennas Propag.*, vol. 57, pp. 1452-1460, May 2009.

[9] M. M. Ilic, A. Z. Ilic, and B. M. Notaros, "Continuously Inhomogeneous Higher Order Finite Elements for 3-D Electromagnetic Analysis," *IEEE Transactions on Antennas and Propagations*, Vol. 57, No. 9, September 2009, pp. 2798-2803

[10] M. Djordjevic and B. M. Notaros, "Double higher order method of moments for surface integral equation modeling of metallic and dielectric antennas and scatterers," *IEEE Transactions on Antennas and Propagation*, Vol. 52, No. 8, pp. 2118-2129, August 2004.

[11] M. M. Ilic and B. M. Notaros, "Higher order large-domain hierarchical FEM technique for electromagnetic modeling using Legendre basis functions on generalized hexahedra," *Electromagnetics*, Vol. 26, No. 7, pp. 517-529, October 2006.

[12] M. Djordjevic and B. M. Notaros, "Higher-Order Hierarchical Basis Functions with Improved Orthogonality Properties for Moment-Method Modeling of Metallic and Dielectric Microwave Structures," *Microwave and Optical Technology Letters*, Vol. 37, No. 2, pp. 83-88, April 2003.

[13] J. B. Pendry, D. Schurig, and D. R. Smith, "Controlling Electromagnetic Fields," *Science*, 312, pp. 1780-1782, June 2006.

[14] D. I. Olćan, M. M. Ilic, B. M. Notaros, B. M. Kolundzija, and A. R. Djordjevic, "Diakoptic higher-order FEM-MoM approach," *2010 IEEE International Symposium on Antennas and Propagation*, July 11-17, 2010, Toronto, Canada.

[15] D. I. Olćan, I. M. Stevanović, J. R. Mosig, and A. R. Djordjević, "Diakoptic approach to analysis of multiconductor transmission lines," *Microwave and Optical Technology Letters*, Vol. 50, No. 4, pp. 931–936, April 2008.

[16] D. I. Olćan, I. M. Stevanović, B.M. Kolundžija, J.R. Mosig, and A. R. Djordjević, "Diakoptic surface integral-equation formulation applied to large antenna arrays," *2008 IEEE International Symposium on Antennas and Propagation*, July 4-12, 2008, San Diego, CA.

[17] D. I. Olćan, I. M. Stevanović, J.R. Mosig, and A. R. Djordjević, "Diakoptic surface integral-equation formulation applied to large 2-D scattering problems," *EuCAP*. November 11-16, 2007, Edinburgh, UK.

[18] D. I. Olćan, I. M. Stevanović, J. R. Mosig, and A. R. Djordjević. "Diakoptic approach to analysis of microwave transmission lines," *Proc. of 36th European Microwave Conference*, pp. 291–294, September 10-15 2006, Manchester, UK.

[19] A. B. Manic, D. I. Olcan, M. M. Ilic, and B. M. Notaros, "Diakoptic FEM-MoM Analysis Using Explicit Connection between Field and Current Bases," *2013 IEEE Antennas and Propagation Society International Symposium Digest*, July 7-12, 2013, Lake Buena Vista, Florida.

[20] A. B. Manic, D. I. Olcan, M. M. Ilic, and B. M. Notaros, "FEM-MoM-Diakoptic Analysis of Scatterers with Anisotropic Inhomogeneities Using Hierarchical Vector Bases on Large Curved Elements," invited paper, Special Session "Advances in Vector Bases for CEM," *11th International Workshop on Finite Elements for Microwave Engineering – FEM2012*, June 4-6, 2012, Estes Park, Colorado.

[21] G. Kron, "Diakoptics: The Piecewise Solution of Large Scale Systems" *MacDonald*, 1963.

[22] Seung-Cheol Lee, Marinos N. Vouvakis, and Jin-Fa Lee, "A non-overlapping domain decomposition method with non-matching grids for modeling large finite antenna arrays, " *Journal of Computational Physics* 203, no. 1, pp. 1-21, 2005.

[23] Yu-Jia Li; Jian-Ming Jin, "A New Dual-Primal Domain Decomposition Approach for Finite Element Simulation of 3-D Large-Scale Electromagnetic Problems," *IEEE Trans. Antennas Propag*.,vol.55, no.10, pp.2803-2810, Oct. 2007.

[24] Kezhong Zhao; Rawat, V.; Lee, J.-F., "A Domain Decomposition Method for Electromagnetic Radiation and Scattering Analysis of Multi-Target Problems," *IEEE Trans. Antennas Propag*., vol.56, no.8, pp.2211-2221, Aug. 2008.

[25] Ilic, M.M.; Notaros, B.M., "Higher Order FEM-MoM Domain Decomposition for 3-D Electromagnetic Analysis," *IEEE Antennas and Wireless Propagation Letters*, vol.8, no., pp.970-973, 2009.

[26] B. M. Kolundžija, and A. R. Djordjević, "Electromagnetic Modeling of Composite Metallic and Dielectric Structures," *Artech House*, Norwood, MA, 2002.

[27] R. F. Harrington, "Time-Harmonic Electromagnetic Fields," New York: *John Wiley & Sons*, 2001.

[28] A. B. Manic, S. B. Manic, M. M. Ilic, and B. M. Notaros, "Large Anisotropic Inhomogeneous Higher Order Hierarchical Generalized Hexahedral Finite Elements for

3-D Electromagnetic Modeling of Scattering and Waveguide Structures," *Microwave and Optical Technology Letters*, vol. 54, No. 7, pp. 1644-1649, July 2012.

[29] B.M. Notaros, B.D Popovic, "General entire-domain method for analysis of dielectric scatterers," in *Microwaves, Antennas and Propagation, IEE Proceedings* , vol.143, no.6, pp.498-504, Dec. 1996.

[30] S. V. Savic, A. B. Manic, M. M. Ilic, and B. M. Notaros, "Efficient Higher Order Full-Wave Numerical Analysis of 3-D Cloaking Structures," Plasmonics, 2012 (published online: 8 July, 2012).

[31] W. C. Chew, J.-M. Jin, E. Michielssen, and J. Song, "Fast and Efficient Algorithms in Computational Electromagnetics," Boston, MA: *Artech House*, 2001.

[32] W. Hackbusch, "A sparse matrix arithmetic based on H-matrices. Part I: Introduction to H-matrices," *Computing*, Vol. 62, pp. 89–108, 1999.

[33] W. Hackbusch and B. N. Khoromskij, "A sparse H-matrix arithmetic. Part II: Application to multi-dimensional problems," *Computing*, Vol. 64, pp. 21–47, 2000.

[34] W. Hackbusch, L. Grasedyck, and S. Börm, "An introduction to hierarchical matrices," *Math. Bohem.*, Vol. 127, pp. 229-241, 2002.

[35] S. Börm, "$\mathcal{H}2$-matrices–Multilevel methods for the approximation of integral operators," *Computing and Visualization in Science*, Vol. 7, no. 3–4, pp. 173–181, Aug. 2004.

[36] W. Chai and D. Jiao, "An $\mathcal{H}2$-Matrix-Based Integral-Equation Solver of Reduced Complexity and Controlled Accuracy for Solving Electrodynamic Problems," *IEEE Trans. Antennas Propag.*, Vol. 57, no. 10, pp. 3147–3159, Oct. 2009.

[37] W. Chai and D. Jiao, "Dense matrix inversion of linear complexity for integral-equation based large-scale 3-D capacitance extraction," *IEEE Trans. Microw. Theory Tech*, Vol. 59, no. 10, pp. 2404–2421, Oct. 2011.

[38] T. Wan, Z. N. Jiang, and Y. J. Sheng. "Hierarchical matrix techniques based on matrix decomposition algorithm for the fast analysis of planar layered structures," *IEEE Trans. Antennas Propag*., Vol. 59, no. 11, pp. 4132–4141, Nov. 2011.

[39] W. Chai and D. Jiao, "Linear-complexity direct and iterative integral equation solvers accelerated by a new rank-minimized representation for large-scale 3-D interconnect extraction," *IEEE Trans. Microw. Theory Tech*, Vol. 61, no. 8, Aug. 2013.

[40] W. Chai and D. Jiao, "Fast-Matrix-Based Direct Integral Equation Solver With Reduced Computational Cost for Large-Scale Interconnect Extraction," *IEEE Trans. Compon. Packag. Manuf. Technol.*, Vol. 3, no. 2, Feb. 2013.

[41] A. Heldring, J. M. Rius, J. M. Tamayo, J. Parrón, and E. Ubeda, "Fast direct solution of method of moments linear system," *IEEE Trans. Antennas Propag.*, Vol. 55, no. 11, pp. 3220–3228, Nov. 2007.

[42] G. H. Golub and C. V. Loan, *Matrix Computations*, 3rd ed., Johns Hopkins University Press, Baltimore, MD, 1996.

[43] M. Gu, and S. C. Eisenstat, "Efficient algorithms for computing a strong rank-revealing QR factorization," *SIAM J. Sci. Comput.*, Vol. 17, no. 4, pp. 848–869, Jul. 1996.

[44] K. Zhao, M. N. Vouvakis, and J. F. Lee, "The adaptive cross approximation algorithm for accelerated method of moments computations of EMC problems," *IEEE Trans. EMC*, Vol. 47, no. 4, pp. 763–773, Nov. 2005.

[45] J. Shaeffer, "Direct solve of electrically large integral equations for problem sizes to 1 M unknowns," *IEEE Trans. Antenna Propag*., Vol. 56, no. 8, pp. 2306–2313, Aug. 2008.

[46] J. Laviada, F. Las-Heras, M. R. Pino, and R. Mittra, "Solution of electrically large problems with multilevel characteristic basis functions," *IEEE Trans. Antennas Propag*., Vol. 57, no. 10, pp. 3189–3198, Oct. 2009.

[47] J. M. Tamayo, A. Heldring, and J. M. Rius, "Multilevel adaptive cross approximation," *IEEE Trans. Antennas Propag*., Vol. 59, pp. 4600–4608, Dec. 2011.

[48] A. Heldring, J. M. Tamayo, C. Simon, E. Ubeda, and J. M. Rius, "Sparsified adaptive cross approximation algorithm for accelerated method of moments computations," *IEEE Trans. Antennas Propag*., Vol. 61, no. 1, pp. 240–246, Jan. 2013.

[49] F. Gesztesy, and K. A. Makarov, "(Modified) Fredholm determinants for operators with matrix-valued semi-separable integral kernels revisited," *Integral Equations and Operator Theory* , Vol. 47, no. 4, pp. 457–497, 2003.

[50] S. Chandrasekaran, P. Dewilde, M. Gu, T. Pals, X. Sun, AJ. van der Veen, and D. White, "Some fast algorithms for sequentially semiseparable representations," *SIAM J. Sci. Comput.*, Vol. 27, no. 2, pp. 341–364, 2015.

[51] E. Corona, PG. Martinsson, and D. Zorin, "An O (N) direct solver for integral equations on the plane," *Appl. Comput. Harmon. Anal.*, Vol. 38, no. 2, pp. 284–317, Mar. 2015.

[52] S. M. Rao, D. R. Wilton, and A. W. Glisson, "Electromagnetic scattering by surfaces of arbitrary shape," *IEEE Trans. Antennas Propag.*, Vol. 30, no. 3, pp. 409–418, May 1982.

[53] K. C. Donepudi, J.-M. Jin, and W. C. Chew, "A higher order multilevel fast multipole algorithm for scattering from mixed conducting/dielectric bodies," *IEEE Trans. Antennas Propag*., Vol. 51, no. 10, pp. 2814–2821, Oct. 2003.

[54] O. Borries, P. Meincke, E. Jørgensen, and P. C. Hansen, "Multi-level fast multipole method for higher-order discretizations," *IEEE Trans. Antennas Propag*., Vol. 62, no. 9, pp. 4695–4705, 2014.

[55] L. P. Zha, Y. Q. Hu, and T. Su, "Efficient surface integral equation using hierarchical vector bases for complex em scattering problems," *IEEE Trans. Antennas and Propag.*, Vol. 60, no. 2, pt. 2, pp. 952–957, Feb. 2012

[56] X. Mu, H.-X. Zhou, K. Chen and W. Hong, "Higher order method of moments with a parallel out-of-core LU solver on GPU/CPU platform", *IEEE Trans. Antennas Propag*., Vol. 62, no. 11, pp.5634–5646, Nov. 2014.

[57] Y. Zhang, Z. Lin, X. Zhao, and T. K. Sarkar, "Performance of a Massively Parallel Higher-Order Method of Moments Code Using Thousands of CPUs and Its

Applications," *IEEE Trans. Antennas Propag.*, Vol. 62, no. 12, pp. 6317–6324, Dec. 2014.

[58] H. Guo, J. Hu, and Z. Nie, "An MPI-OpenMP hybrid parallel H-LU direct solver for electromagnetic integral equations," *International Journal of Antennas and Propagation*, Vol. 2015, Article ID 615743, 10 pages, 2015.

[59] A. Schroder, H.D. Bruns, and C. Schuster, "Fast evaluation of electromagnetic fields using a parallelized adaptive cross approximation," *IEEE Trans. Antennas Propag.*, Vol. 62, No. 5, 2818– 2822, May. 2014.

[60] B. M. Notaros, B. D. Popovic, J. P. Weem, R. A. Brown, and Z. Popovic, "Efficient large-domain MoM solutions to electrically large practical EM problems," *IEEE Trans. Microw. Theory Tech*, Vol. 49, pp.151–159, Jan. 2001.

[61] S. Wang, X. S. Li, J. Xia, Y. Situ, and M. V. De Hoop, "Efficient Scalable Algorithms for Solving Dense Linear Systems with Hierarchically Semiseparable Structures," *SIAM J. Sci. Comput.*, Vol. 35, no. 6, pp. C519–C544, 2013.

[62] A. B. Manic, F.-H. Rouet, X. S. Li, and B. M. Notaros, "Efficient EM Scattering Analysis Based on MoM, HSS Direct Solver, and RRQR Decomposition," *2015 IEEE International Symposium on Antennas and Propagation*, July 19-25, 2015, Vancouver, BC, Canada.

[63] E. Michielssen and A. Boag, "A multilevel matrix decomposition algorithm for analyzing scattering from large structures," *IEEE Trans. Antennas Propag.*, Vol. 44, no. 8, pp. 1086–1093, Aug. 1996.

[64] G. Han, H. Jun, and E. Michielssen, "On MLMDA/Butterfly compressibility of inverse integral operators," *IEEE Antennas Wireless Propag. Lett.*, Vol. 12, pp. 31–34, 2013.

[65] Y. Brick, V. Lomakin, A. Boag, "Fast Direct Solver for Essentially Convex Scatterers Using Multilevel Non-Uniform Grids," *IEEE Trans. Antennas Propag* , Vol. 62, no. 8, pp.4314–4324, Aug. 2014.

[66] M. Kostic and B. Kolundzija, “Maximally orthogonalized higher order bases over generalized wires, quadrilaterals, and hexahedra,” *IEEE Trans. Antennas Propag.*, vol. 61, no. 6, pp. 3135–3148, Jun. 2013.

[67] I. Bogaert, and F. P. Andriulli, “Maximally Orthogonal High-Order Basis Functions have a Well-Conditioned Gram Matrix,” *IEEE Trans. Antennas Propag.*, Vol. 62, no. 8, pp. 4096–4104, Aug. 2014.

[68] A. Heldring, J. M. Tamayo, and J. M. Rius, “On the degrees of freedom in the interaction between sets of elementary scatterers,” presented at the 3rd Eur. Conf. Antennas Propag. (Eucap), Berlin, Germany, Mar. 23–27, 2009.

[69] A. B. Manic, E. Chobanyan, M. M. Ilic, and B. M. Notaros, “Parallelization of Double Higher Order FEM and MoM Techniques” *Proceedings of 2014 IEEE Antennas and Propagation Society International Symposium*, July 6–12, 2014, Memphis, Tennessee.

[70] ScaLAPACK—Scalable Linear Algebra PACKage, http://www.netlib.org/scalapack.

[71] *BLACS*, http://www.netlib.org/blacs.

[72] J. Towns, T. Cockerill, M. Dahan, I. Foster, K. Gaither, A. Grimshaw, V. Hazlewood, S. Lathrop, D. Lifka, G. D. Peterson, R. Roskies, J. Ray Scott, N. Wilkins-Diehr, "XSEDE: Accelerating Scientific Discovery", *Computing in Science & Engineering*, Vol.16, no. 5, pp. 62-74, Sept.-Oct. 2014, doi:10.1109/MCSE.2014.80

[73] https://portal.tacc.utexas.edu/user-guides/ stampede#overview

[74] O. M. Bucci and G. Franceschetti, “On the degrees of freedom of scattered fields,” *IEEE Trans. Antennas Propag*., Vol. 37, no. 7, pp. 918–926, July 1989.

[75] A. Heldring, J. M. Rius, J. M. Tamayo, J. Parrón, and E. Úbeda, “Multiscale compressed block decomposition for fast direct solution of method of moments linear system,” *IEEE Trans. Antennas Propag*., vol. 59, no. 2, pp. 526–536, Feb. 2011.

[76] A. C. Woo, H. T. G. Wang, M. J. Schuh, and M. L. Sanders, "Benchmark radar targets for the validation of computational electromagnetic programs," *IEEE Antennas Propagat. Mag*., Vol. 35, pp. 84–89, Feb. 1993.

[77] D. R. Wilton, S. M. Rao, A. W. Glisson, D. H. Schaubert, O. M. Al-Bundek, and C. M. Butler, "Potential integrals for uniform and linear source distributions on polygonal and polyhedral domains," *IEEE Transactions on Antennas and Propagation*, vol. 32, no. 3, pp. 276–281, March 1984.

[78] R. D. Graglia, "On the numerical integration of the linear shape functions times the 3-D Green's function or its gradient on a plane triangle," *IEEE Transactions on Antennas and Propagation*, vol. 41, no. 10, pp. 1448–1455, October 1993.

[79] M. S. Tong and W. C. Chew, "A novel approach for evaluating hypersingular and strongly singular surface integrals in electromagnetics," *IEEE Transactions on Antennas and Propagation*, vol. 58, no. 11, pp. 3593–3601, November 2010.

[80] D. J. Taylor, "Accurate and efficient numerical integration of weakly singular integrals in Galerkin EFIE solutions," *IEEE Transactions on Antennas and Propagation*, vol. 51, no. 7, pp.1630–1637, July 2003.

[81] L. Rossi and P. J. Cullen, "On the fully numerical evaluation of the linear-shape function times the 3-D Green's function on a plane triangle," *IEEE Transactions on Microwave Theory and Techniques*, vol. 47, no. 4, pp. 398–402, April 1999.

[82] M. Khayat and D. R. Wilton, "Numerical evaluation of singular and near-singular potential integrals," *IEEE Transactions on Antennas and Propagation*, vol.53, No.10, pp. 3180–3190, October 2005.

[83] M. A. Khayat, D. R. Wilton, and P. W. Fink, "An improved transformation and optimized sampling scheme for the numerical evaluation of singular and near-singular potentials," *IEEE Antennas and Wireless Propagation Letters*, vol. 7, pp. 377–380, 2008.

[84] W. Ding and G. Wang, "Treatment of singular integrals on generalized curvilinear parametric quadrilaterals in higher order method of moments," *IEEE Antennas and Wireless Propagation Letters*, vol. 8, pp. 1310–1313, 2009.

[85] E. Jørgensen, J. L. Volakis, P. Meincke, and O. Breinbjerg, "Higher order hierarchical Legendre basis functions for electromagnetic modeling," *IEEE Transactions on Antennas and Propagation*, vol. 52, pp. 2985–2995, November 2004.

[86] H. Yuan, N. Wang, and C. Liang, "Combining the higher order method of moments with geometric modeling by NURBS surfaces," *IEEE Transactions on Antennas and Propagation*, vol. 57, no. 11, pp. 3558–3563, November 2009.

[87] R. Kieser, C. Schwab and W. L. Wendland, "Numerical evaluation of singular and finite-part integrals on curved surfaces using symbolic manipulation," *Computing*, vol. 49, pp. 279-301, 1992.

[88] Sheng, Xin-Qing, and Wei Song., *Essentials of Computational Electromagnetics*. Vol. 757. Wiley, 2011.

[89] A. F. Peterson, "Mapped Vector Basis Functions for Electromagnetic Integral Equations," *Morgan & Claypool Publishers*, 2006.

[90] M. G. Duffy, "Quadrature over a pyramid or cube of integrands with a singularity at a vertex," *SIAM J. Numer. Anal.*, vol. 19, no. 6, pp. 1260–1262, 1982.

[91] K. Sertel and J. L. Volakis, "Method of moments solution of volume integral equations using parametric geometry modeling," *Radio Science*, vol. 37, pp.10– (1–7), January–February 2002.

[92] Klopf, E.M.; Sekeljic, N.J.; Ilic, M.M.; Notaros, B.M., "Optimal Modeling Parameters for Higher Order MoM-SIE and FEM-MoM Electromagnetic Simulations," *IEEE Transactions on Antennas and Propagation*, vol.60, no.6, pp.2790,2801, June 2012.

[93] S. Jarvenpaa, M. Taskinen, P. Yla-Oijala, "Singularity subtraction technique for high-order polynomial vector basis functions on planar triangles," *Trans. Antennas Propag.*, vol.54, no.1, pp.42,49, Jan. 2006.

5 PUBLICATIONS OF THE CANDIDATE

JOURNAL PAPERS

1. S. V. Savic, A. B. Manic, M. M. Ilic, and B. M. Notaros, "Efficient Higher Order Full-Wave Numerical Analysis of 3-D Cloaking Structures," *Plasmonics, 2012* (published online: 8 July, 2012), doi: 10.1007/s11468-012-9410-0.

2. A. B. Manic, S. B. Manic, M. M. Ilic, and B. M. Notaros, "Large Anisotropic Inhomogeneous Higher Order Hierarchical Generalized Hexahedral Finite Elements for 3-D Electromagnetic Modeling of Scattering and Waveguide Structures," *Microwave and Optical Technology Letters*, vol. 54, No. 7, July 2012, pp. 1644-1649.

3. A. B. Manic, M. Djordjevic, and B. M. Notaros, "Duffy Method for Evaluation of Weakly Singular SIE Potential Integrals over Curved Quadrilaterals with Higher Order Basis Functions," *IEEE Transactions on Antennas and Propagation*, Vol. 62, No. 6, June 2014.

4. A. B. Manić, D. I. Olćan, M. M. Ilić, and B. M. Notaroš, "Diakoptic approach combining finite-element method and method of moments in analysis of inhomogeneous anisotropic dielectric and magnetic scatterers," *Electromagnetics*, vol. 34, no. 3–4, pp. 222–238, 2014.

5. M. Thurai, V. N. Bringi, A. B. Manić, N. J. Šekeljić, and B. M. Notaroš, "Investigating rain drop shapes, oscillation modes, and implications for radiowave propagation," *Radio Science*, vol. 49, no. 10, pp. 921-932, October 2104.

6. E. Chobanyan, N. J. Šekeljić, A. B. Manić, M. M. Ilić, V. N. Bringi, and B. M. Notaroš, "Efficient and Accurate Computational Electromagnetics Approach to Precipitation Particle Scattering Analysis Based on Higher Order Method of Moments Integral-Equation Modeling", *Journal of Atmospheric and Oceanic Technology*, published online (http://dx.doi.org/10.1175/JTECH-D-15-0037.1).

7. Ana B. Manić, François-Henry Rouet, Xiaoye Sherry Li, and Branislav M. Notaroš, "Efficient Scalable Parallel Higher Order Direct MoM-SIE Method with Hierarchically Semiseparable Structures for 3D Scattering, " submitted to *IEEE Transactions on Antennas and Propagation*.

8. Ana B. Manić, and Branislav M. Notaroš, "Fast Computation of Near-Singular and Near-Hypersingular Integrals in Higher Order Method of Moments Using Curved Quadrilateral Patches, " *IEEE Transactions on Antennas and Propagation*, manuscript completed, to be submitted.

BOOK CHAPTER

9. B. M. Notaros, M. M. Ilic, S. V. Savic, and A. B. Manic, "Construction, Modeling, and Analysis of Transformation-Based Metamaterial Invisibility Cloaks," Invited Summary Review Chapter, Accepted for The Annual Reviews in Plasmonics, edited by Chris D. Geddes, currently in print with Springer.

PEER-REVIEWED CONFERENCE PAPERS AND ABSTRACTS

10. A. B. Manic, M. Djordjevic, E. Smith, and B. M. Notaros, "Numerical Computation of Singular Integrals in Higher Order Method of Moments Using Curved Quadrilateral Patches," *Proc. 2013 USNC-URSI National Radio Science Meeting*, January 9-12, 2013, Boulder, Colorado.

11. A. B. Manic, M. M. Ilic, and B. M. Notaros, "Symmetric Coupling of Finite Element Method and Method of Moments Using Higher Order Elements," *2012 IEEE Antennas and Propagation Society International Symposium Digest*, July 8-14, 2012, Chicago, Illinois.

12. A. B. Manic, D. I. Olcan, M. M. Ilic, and B. M. Notaros, "FEM-MoM-Diakoptic Analysis of Scatterers with Anisotropic Inhomogeneities Using Hierarchical Vector Bases on Large Curved Elements," invited paper, Special Session "Advances in Vector Bases for CEM," *11th International Workshop on Finite Elements for Microwave Engineering – FEM2012*, June 4-6, 2012, Estes Park, Colorado.

13. A. B. Manic, M. M. Ilic, and B. M. Notaros, "Symmetric and Nonsymmetric FEM-MoM Techniques Using Higher Order Hierarchical Vector Basis Functions and Curved Parametric Elements," invited paper, Special Session "Advances in Hybrid Methods and Multiphysics Problems," *11th International Workshop on Finite Elements for Microwave Engineering –FEM2012*, June 4-6, 2012, Estes Park, Colorado.

14. A. B. Manic, S. B. Manic, S. V. Savic, M. M. Ilic, and B. M. Notaros, "Efficient Electromagnetic Analysis Using Electrically Large Curved p-Refined Hierarchical Anisotropic Inhomogeneous Finite Elements," *Proc. 2012 USNC-URSI National Radio Science Meeting*, January 4-7, 2012, Boulder, Colorado.

15. A. B. Manic, D. I. Olcan, M. M. Ilic, and B. M. Notaros, "Diakoptic FEM-MoM Analysis Using Explicit Connection between Field and Current Bases," *2013 IEEE Antennas and Propagation Society International Symposium Digest*, July 7-12, 2013, Lake Buena Vista, Florida.

16. E. Chobanyan, N. J. Sekeljic, A. B. Manic, M. M. Ilic, and B. M. Notaros, "Atmospheric Particle Scattering Computation Using Higher Order MoM-SIE Method," *2013 IEEE Antennas and Propagation Society International Symposium Digest*, July 7-12, 2013, Lake Buena Vista, Florida.

17. N. J. Sekeljic, A. B. Manic, M. M. Ilic, and B. M. Notaros, "Transient Analysis of 3D Waveguides Using Double-Higher Time-Domain Finite Element Method," *2013 IEEE Antennas and Propagation Society International Symposium Digest*, July 7-12, 2013, Lake Buena Vista, Florida.

18. M. Thurai, V. N. Bringi, A. B. Manic, and B. M. Notaros, "Ongoing Investigations of Rain Drop Shapes and Oscillation Modes," *Proc. URSI Commission F Triennial Open Symposium on Radiowave Propagation & Remote Sensing*, April 30-May 3, 2013, Ottawa, Canada.

19. Ana Manic, Elene Chobanyan, Milan Ilic, and Branislav Notaros, "Parallelization of Double Higher Order FEM and MoM Techniques," *2014 IEEE Antennas and Propagation Society International Symposium Digest*, July 6-11, 2014, Memphis, Tennessee.

20. Nada Sekeljic, Ana Manic, Elene Chobanyan, Merhala Thurai, V. N. Bringi, and Branislav Notaros, "Electromagnetic Scattering by Oscillating Rain Drops of Asymmetric Shapes," *2014 IEEE Antennas and Propagation Society International Symposium Digest*, July 6-11, 2014, Memphis, Tennessee.

21. B. M. Notaros, M. M. Ilic, D. I. Olcan, M. Djordjevic, A. B. Manic, and E. Chobanyan, "Hybrid Higher Order Numerical Methods in Electromagnetics," invited paper, Special Session "Numerical Methods in Electromagnetics," *Proceedings of 16th International Conference on Electromagnetics in Advanced Applications – ICEAA 2014*, August 3-8, 2014, Palm Beach, Aruba, pp. 411-414.

22. A. B. Manic, E. Chobanyan, D. I. Olcan, M. M. Ilic, and B. M. Notaros, "FEM-SIE and VIE-SIE Diakoptic Domain-Decomposition Electromagnetic Scattering Analyses Using Higher Order Numerical Discretizations," invited paper, Special Session "*Advanced FEM and Hybrid Techniques," 12th International Workshop on Finite Elements for Microwave Engineering – FEM2014*, May 14-17, 2014, Chengdu, China.

23. Ana Manic, François-Henry Rouet, Xiaoye Sherry Li, Branislav Notaros, "Efficient EM Scattering Analysis Based on MoM, HSS Direct Solver, and RRQR Decomposition," *2015 IEEE Antennas and Propagation Society International Symposium Digest*, July 19-25, 2015, Vancouver, British Columbia, Canada.

24. Ana Manic, Branislav Notaros, "Numerical Computation of Near-Singular and Near-Hypersingular Integrals in Higher Order Method of Moments Using Curved Quadrilateral Patches," presented at *2015 IEEE Antennas and Propagation and North American Radio Science Meeting*, July 19-25, 2015, Vancouver, British Columbia, Canada.

25. Ana Manic, Sanja Manic, Aaron Smull, Branislav Notaros, "Parallel Double Higher Order Algorithms for Large and Complex Problems Based on Integral and Partial Differential Equations in Computational Sciences Developed for HPC," presented at *2015 RMACC High Performance Computing Symposium*, August 12-14, 2015, Boulder, Colorado.